Closely Coupled GPS/INS Relative Positioning For Automated Vehicle Convoys

by

Scott M. Martin

A thesis submitted to the Graduate Faculty of
Auburn University
in partial fulfillment of the
requirements for the Degree of
Master of Science

Auburn, Alabama
May 9, 2011

Keywords: DGPS, Relative Positioning, Convoys

Approved by:

David M. Bevly, Chair, Professor of Mechanical Engineering
Dan Marghitu, Professor of Mechanical Engineering
John Y. Hung, Professor of Electrical and Computer Engineering

Abstract

In this thesis, differential GPS methods are developed for use in automated vehicle convoy positioning. The GPS pseudorange and carrier phase measurements are used to compute relative position vectors between two vehicles with sub-meter errors. The carrier phase measurement makes this level of accuracy attainable, but the carrier phase ambiguity must be resolved prior to the relative position estimation. An algorithm, referred to as Dynamic base Real Time Kinematic (DRTK) algorithm, is described in this thesis to estimate the carrier phase ambiguity and the relative position vector between two GPS receivers. The DRTK algorithm is capable of using single frequency (L1 or L2 frequency only) or dual frequency (L1 and L2 frequency) GPS measurements to estimate the relative position vector. A comparative study of the performance of the algorithm using either single or dual frequency measurements is presented.

The DRTK algorithm is expanded to incorporate inertial measurement to increase to output rate, to improve solution availability, and to improve the reliability of the algorithm. Since inertial navigation systems (INS) compute a navigation solution independent of any additional infrastructure, the INS can be used to update the relative position vector estimate during short GPS outages. The update rate of the INS is also as much as ten times the rate of the GPS receiver; the integrated system produces estimates at a significantly higher output rate. The combined DRTK/INS system is implemented with two integration architectures – a federated GPS/INS/DRTK architecture and a centralized DRTK/INS architecture. Each configuration produced estimates of the relative position vector with error on the centimeter level.

Finally, the use of relative positioning to autonomously follow a human driven lead vehicle is presented. Time difference carrier phase (TDCP) measurements are used to estimate

the change in the position of the following vehicle between measurement epochs. The TDCP algorithm is combined with the DRTK algorithm to estimate the position of the following vehicle relative to a virtual lead vehicle position. Analysis of the accuracy of the TDCP algorithm at individual measurement epochs and over varying time intervals is presented. The DRTK/TDCP following method is compared to a GPS waypoint following method using data collected on an automated all-terrain vehicle.

Acknowledgments

I would like to thank my sister, Stephanie for all the wisdom and love she has given me over the years. I would also like to thank my parents for their unending support in all my endeavors. I would like acknowledge all the friends from Greenville that always make life interesting and full of excitement; I wish you all the happiness that you deserve. I would also like to thank Dr. Rick Williams for his encouragement and friendship.

I especially want to acknowledge the team of researchers at the Auburn University GPS and Vehicle Dynamics Laboratory. My adviser Dr. David Bevly has been a consistent source of knowledge and leadership throughout my studies. I owe a great deal of my success to Dr. William Travis for his guidance and counsel. Thanks to all the members of the lab for being an indispensable source of information and for your willingness to defend your ideology.

Table of Contents

List of Figures

List of Tables

Chapter 1

Introduction

The Global Positioning System (GPS) has changed the way drivers navigate by combining accurate position information with road maps to provide real time directions to their destination. The future of GPS assisted ground vehicle operation is automation which has already been demonstrated in precision agriculture and unmanned military vehicles (ref). The work in this thesis focuses on automated vehicle convoys with autonomous ground vehicles (AGV) following human driven lead vehicles. AGVs offer significant flexibility in convoy operations. Automated following vehicles can be configured to have human drivers at the ready or to be completely unmanned. In civilian applications, several automated delivery trucks may leave a distribution center led by a human driven vehicle. Drivers in the following vehicles can divert their attention from the road while the vehicle operates automatically. When the lead driver needs a rest, one of the drivers of a following vehicle can relieve him at the front of the formation. This would decrease the need for downtime, when the truck sits still while the driver rests. A military convoy could operate in a similar fashion, but instead of resting while in the following position, the driver's responsibility is to monitor the surroundings for hostile forces. However, it may be more important to remove drivers from harms way by using unmanned vehicles.

Vehicle automation is not a new science but the advent of GPS has brought on new possibilities for these complex systems. Accurate position and velocity information is invaluable when navigating without the benefit of human sensing and motor skill. Unfortunately, GPS has its limitations in both accuracy and availability. Alternate measurement processing techniques can be implemented to improve accuracy, but GPS availability will always be affected by environmental influences. This thesis attempts to address each concern by

combining advanced GPS measurement processing with additional sensing capabilities to provide a reliable and accurate navigation solution for autonomous following.

1.1 Vehicle Sensing Capabilities

Autonomous vehicles are typical outfitted with a multitude of sensors. This thesis focuses on navigation systems incorporating GPS and inertial measurement units. The following is an introduction to these sensors and their capabilities.

1.1.1 Global Positioning System

GPS consists of three segments including the space segment, the control segment, and the user segment which combine to provide users with accurate position, velocity and time. The space segment is composed of a minimum of 24 satellites in six orbital planes. Generally there are approximately 32 satellites in orbit, oriented to allow users to have a clear line of sight to at least four satellites at any given time. The control segment is based at Schriever Air Force Base (AFB) in Colorado Springs, Colorado with additional monitoring stations around the Earth and it is tasked with maintaining satellite orbits and accurate timing for the system. The user segment is the GPS receiver which tracks radio signals broadcast by each GPS satellite [28]. GPS satellites transmit on three frequencies in the L band: L1 at 1575.42 MHz, L2 at 1227.60 MHz and L5 at 1176.45 MHz. Each transmitted signal contains a ranging code and navigation message modulated on a sinusoidal carrier.

The ranging codes are pseudorandom binary sequences unique to each satellite and are referred to as pseudorandom noise (PRN) codes. The PRN codes are selected to be orthogonal to one another allowing a receiver to access various satellite signals broadcast at the same frequency through Code Division Multiple Access (CDMA) [19]. Both military and civilian ranging codes are modulated on the L1 and L2 carrier frequencies. The civilian ranging code, called the Course Acquisition (C/A) code, is 1023 chips long and repeats every one millisecond. The military ranging code, or P code, is much longer, 6.1871×10^{12} chips,

and is broadcast at ten times the rate of the C/A code. Encryption of the P code limits the availability of the signal to military users with access to the encryption key. Originally, the L2 carrier was modulated with only the P code making it unavailable to civilian users. The launch of Block IIR-M satellites beginning in 2005 marked the introduction of the L2C ranging code providing civilian users with dual frequency capabilities[9]. Despite the fact that the L2C code is available on a limited number of satellites in the constellation, many civilian users can now access L2 P coded signals through semi-codeless tracking techniques [32].

The navigation message provides the user with satellite information and the signal transmission time [16]. Satellite information includes almanac data, ephemeris data, and satellite health which allow the user to determine the satellite's position and velocity. The distance from a given satellite to the receiver is calculated from the time of flight (TOF) of the signal. The TOF formulation relies on a receiver generated replica of the ranging code. The replica is shifted in time to match the satellite transmitted ranging code. With perfect time synchronization between the satellite clock and the receiver clock, the time shift is due to the TOF of the signal. The range from the receiver to the satellite is equal to the TOF times the speed of light. The user's position is then constrained to a sphere centered at the satellite's position with a radius equal to the measured range. With three accurate measurements, the user's position can be determined by trilateration. However, the measured range is corrupted with timing errors due to the inaccuracy of both the satellite and receiver clocks and is therefore referred to as the pseudorange measurement. Satellite clock corrections terms are transmitted with the ephemeris data and are used to significantly reduce the error introduced by the satellite clock. By including a fourth measurement, the user estimates a three dimensional position and the range bias due to the receiver clock error.

GPS errors are not limited to satellite and receiver clock errors. Additional error sources include but are not limited to satellite ephemeris errors, propagation delays due to the atmosphere, multipath and receiver noise. Satellite ephemeris errors result from inaccurate information in the transmitted navigation message and lead to ranging errors of approximately 2.1 meters on average. Atmospheric delays are attributed to two layers of the atmosphere: the ionosphere and the troposphere. Ionospheric delays are typically the dominant GPS error source resulting in average range errors of 4.0 meters when not modeled accurately. The tropospheric delays are less severe with associated range errors of approximately 0.5 meters. Multipath, which is the error due to reflected GPS signals, and receiver noise contribute additional range errors of approximately 1.0 meter and 0.5 meters respectively. The cumulative effect of these errors and the residual satellite clock error is a range error with a standard deviation of 5 meters. For a typical satellite geometry, this error will result in horizontal position errors near 10 meters and vertical position errors near 13 meters [28].

1.1.2 Inertial Measurement Unit

Inertial Measurement Units (IMU) are comprised of some combination of accelerometers and gyroscopes. These sensors provide measurements of specific force and angular rate about the units sensitive axes hundreds of times a second. The IMU may be mounted in a strapdown or gimbaled configuration with most modern applications using the strapdown approach. IMUs are available in a variety of grades ranging from automotive to marine with a wide range of accuracy and stability.

In principle, an accelerometer measures the displacement of an internal proof mass relative to the IMU case caused by an externally applied force. For a sensor in free fall near the surface of the Earth, the acceleration due to gravity is experienced by the proof mass and IMU case resulting in a measurement of zero acceleration (neglecting drag effects). The same sensor on the surface of the Earth measures the force of the Earth pushing up on the IMU case and not on the spoof mass. Therefore, accelerometers are said to measure the specific

Table 1.1: Common Bias Values for Various IMU Grades (From: [17])

IMU Grade	Accelerometer Bias (m/s^2)	Gyroscope Bias (deg/hr)
Marine	10^{-4}	0.001
Aviation	$3 \times 10^{-4} - 10^{-3}$	0.01
Intermediate	$10^{-3} - 10^{-2}$	0.1
Tactical	$10^{-2} - 10^{-1}$	$1 - 100$
Automotive	> 1	> 100

force acting of the unit. Accelerometers used in strapdown applications are commonly either pendulous or vibrating beam [17].

Gyroscopes measures the rate of change of the angular position of the IMU about a sensitive axis. Common gyroscopes include spinning mass, optical, and vibratory devices. These sensors operate on principles such as the conservation of angular momentum, the Sagnac effect, and Coriolis acceleration. Additional information on gyroscope operation is available in [17].

IMU errors include but are not limited to scale factor errors, misalignment errors, biases, and random noise. The accelerometer and gyroscope biases are often the dominant errors sources of an IMU. The bias term is composed of a static turn-on bias and a dynamic in-run bias. Table 1.1 shows typical bias values for various IMU grades as given in [17].

1.2 Prior Work

This thesis incorporates GPS and IMUs to compute relative positioning information for navigation of an autonomous vehicle following the path of a lead vehicle. Relative GPS positioning is accomplished using the carrier phase measurement which will be described in detail in Chapter 2. Carrier phase position estimation was originally studied for surveying applications in the 1970s. The first use of carrier measurements for dynamic applications came in 1985 [31]. Carrier phase measurements contain an inherent integer ambiguity that must be resolved before estimating position. This ambiguity is easily estimated as a floating point value; however position accuracy can be increased significantly if fixed integer estimate

is available . Researchers at Deft University addressed the integer estimation problem in the 1990s and developed the Least Squares Ambiguity Decorrelation Adjustment or LAMBDA method [33].

Carrier phase relative positioning has been used extensively in aircraft navigation. First, systems were developed to use GPS measurements from static bases at the airport to calculate accurate relative positions for automated landing [11]. This work was later expanded to include landing sites where a static GPS base station is unavailable, for example landing on an aircraft carrier [10, 14, 29]. Carrier phase positioning has also been applied to in flight operation of unmanned aerial vehicles (UAV). Relative position solutions using GPS carrier measurements have been studied for autonomous formation flight [7] and autonomous airborne refueling [20].

There is considerable work in the literature of the fusion of GPS and IMUs to produce position, velocity, and attitude estimates with high update rates. The focus of this thesis is the integration of carrier phase based GPS solutions with inertial measurements. At the University of Calgary, inertial measurements were used to improve the reacquisition of integer estimates of the carrier phase ambiguity [30]. Additionally, GPS and IMUs were used in tandem for relative positioning in helicopter formation flight [13] and precision shipboard landing [4]. In contrast to these examples, the carrier phase GPS and IMU positioning algorithms described in this thesis are developed for ground vehicles. Also, the inertial measurements are incorporated to increase the update rate of the position solution and the GPS algorithms are developed to use L1 measurements,L2 measurements or L1 and L2 measurements. Results are shown comparing the solutions of single and dual frequency GPS solutions.

Much of the research in the field of autonomous following relies on a clear line of sight to the lead vehicle [5, 26, 25]. Often the following vehicle is sensing the position of the lead vehicle in its field of vision with camera, Lidar, or both [15, 5, 8]. Typically, these methods are chosen over GPS due to inconsistency and inaccuracy of GPS measurements. However,

the use of GPS does allow for non line of sight following and accuracy and integrity can be improved by using carrier phase relative position. Researchers at the Position, Localization and Navigation Group developed methods using carrier phase relative position to maintain vehicle spacing in vehicle convoys [3].

1.3 Contributions

The focus of the research presented in this thesis is the development of relative positioning methods for autonomous ground vehicle convoys. To that end, the following contributions are made:

- Relative positioning algorithms are developed to utilizing either the L1 frequency GPS observable, the L2 frequency GPS observable or a combination of both L1 and L2 frequency GPS observables. The algorithms are compared based on accuracy and reliable of their results in various operational scenarios.

- The relative positioning algorithms are expanded to include high update rate inertial measurements to improve the availability of the relative position solution. Two integration architectures are implemented and their results are examined. A fault detection and exclusion routine is incorporated to monitor solution integrity during the GPS measurement update. The federated DRTK/INS integration architecture with fault detection and exclusion capabilities was presented by the author of this thesis at the Institute of Navigation and Institute of Electrical and Electronics Engineers Position, Location, and Navigation Symposium in May 2010 [23].

- A path following method combining the relative positioning algorithm with GPS carrier phase based odometry is examined. The inherent error growth due to the accumulation of residual noise in the odometry estimates is evaluated. Time difference GPS carrier phase estimation of the change in the position of a vehicle was combined with GPS relative positioning in a terrain mapping algorithm by the author of this thesis

for publication in the proceedings of the Institute of Navigation GNSS conference in September 2010 [22].

1.4 Thesis Outline

Chapter 2 is a discussion of differential GPS techniques focusing on carrier phase differential positioning. Single and dual frequency algorithms are developed and compared. These algorithms are expanded to include inertial measurements in Chapter 3. Chapter 4 introduces time differencing of GPS carrier phase measurements for vehicle odometry and its impact on path following. Finally, Chapter 5 provides conclusions from the work presented here and provides direction for future work in the field of autonomous vehicle convoys.

Chapter 2

Dynamic base Real Time Kinematic

In this work, GPS is used to determine position of the lead vehicle relative to the following vehicle. To limit the position errors of the standard GPS solution, differential GPS (DGPS) techniques are used. DGPS takes advantage of the common mode error sources experienced by receivers operating in close proximity. The signal delays introduced by the atmosphere are highly correlated for receivers separated by several kilometers or less. The residual satellite clock errors after correction are also nearly identical. Measurements from two receivers are differenced to mitigate these common mode errors. DGPS methods incorporate the GPS pseudorange measurement, the carrier phase measurement, or both.

The carrier phase measurement is an accumulation of the cycles of the GPS sinusoidal carrier from the time of signal acquisition to the present time. This phase shift can be measured with significantly higher accuracy than the pseudorange (to within five millimeters [24]) but the absolute measurement contains an ambiguous number of carrier cycles. With accurate estimates of the carrier phase integer ambiguity, the relative position vector (RPV) between two GPS receivers can be estimated to within centimeters of the true value.

Real time kinematic (RTK) systems exploit the accuracy of the carrier phase measurement to calculate highly precise global position estimates. This is accomplished by combining measurements from a static base station at a known position with measurements for roving GPS receiver in the area. The base station broadcasts its position, pseudorange measurements and carrier phase measurements to the rover and the RPV from the base station to the rover is estimated. The RPV is then added to the position of base station resulting in a global position solution for the rover. This method results in a highly accurate global

position solution of the roving receiver but requires the rover to be operating in proximity to a GPS base station.

The autonomous following scenario offers a unique opportunity to apply the same technique without requiring the static base station. The global information is not the ultimate concern of the following vehicle; only the relative location of the lead vehicle is important. In this case the following vehicle is treated as a base station and the leader's position is estimated relative to the followers current location. The global accuracy is lost but the accuracy of the RPV is retained. This method will be referred to as Dynamic base RTK (DRTK). The pertinent GPS measurements and the RPV estimation algorithm are discussed in this chapter.

2.1 Measurements

The formulation of the DRTK algorithm will begin with a description of the relevant GPS measurements. The pseudorange and carrier phase measurements are expressed mathematically in Equation (2.1) and Equation (2.2) respectively.

$$\rho_a^s = r_a^s + cdt_a + cdt^s + T_a^s + I_a^s + M_{a_\rho}^s + v_{a_\rho}^s \tag{2.1}$$

$$\phi_a^s = r_a^s + cdt_a + cdt^s + T_a^s - I_a^s + \lambda N_a^s + M_{a_\phi}^s + v_{a_\phi}^s \tag{2.2}$$

where,

ρ_a^s	is the measured pseudorange between receiver a and satellite s
ϕ_a^s	is the measured carrier phase between receiver a and satellite s
r_a^s	is the true range between receiver a and satellite s
c	is the speed of light
dt_a	is the receiver clock bias
dt^s	is the satellite clock bias
T_a^s	is the tropospheric delay between receiver a and satellite s in units of meters
I_a^s	is the ionospheric delay between receiver a and satellite s in units of meters
λ	is the carrier wavelength (L1 = 0.1902m or L2 = 0.2442m)
N_a^s	is the carrier integer ambiguity between receiver a and satellite s
M_a^s	is the multipath error
v_a^s	is the measurement noise

As stated in the introduction, the GPS signal is subjected to delays due to the atmosphere. It is interesting to note that the ionosphere affects the code based pseudorange measurement and the carrier based phase measurement differently. The magnitude of the errors are the same when each measurement is expressed in units of length. However, the code is delayed, effectively increasing the measured pseudorange and the carrier is advanced thereby decreasing the phase measurement. Assuming that multipath errors are small, the ionospheric delay and the carrier integer ambiguity are the dominant differences in the two measurements.

2.1.1 Single Differences

Given measurements from two receivers, the common mode errors of the measured pseudorange and carrier phase are mitigated by computing the single difference of each measurement. The single differenced pseudorange and carrier phase are calculated by subtracting the measurement of one receiver to a given satellite from the corresponding measurement from the second receiver. Therefore, single differenced pseudorange and carrier phase observables are computed for each visible satellite. Satellite clock errors are removed in the operation and the errors due to atmospheric interference are significantly reduced. Residual atmospheric errors are assumed to be small and are lumped in with the measurement noise

term. After differencing, the pseudorange measurement is a function of the distance between the receivers, the relative receiver clock bias, and noise of increased variance. The single differenced carrier phase also contains the distance and noise terms in addition to the difference of the carrier phase ambiguities from the two receivers. The noise term will be discussed in detail in Section 2.2. Single differenced pseudorange and carrier phase measurements are expressed mathematically in Equation (2.3) and Equation (2.4).

$$\Delta\rho^s_{ab} = r^s_{ab} + cdt_{ab} + v^s_{ab_\rho} \tag{2.3}$$

$$\Delta\phi^s_{ab} = r^s_{ab} + cdt_{ab} + \lambda N^s_{ab} + v^s_{ab_\phi} \tag{2.4}$$

The subscript ab denotes the relative information between receiver a and receiver b. In this formulation, multipath errors are assumed to be negligible.

2.1.2 Double Differences

As seen in Equation (2.3) and Equation (2.4), the single differenced measurements contain the relative clock bias from the receivers. It is beneficial to remove this clock error term by computing the double differenced pseudorange and carrier phase. The double difference calculation begins by selecting one of the computed single differences as the base measurement. In this work the measurement corresponding to the closest satellite is selected as the base measurement. This value is subtracted from the single differenced measurements associated with the other visible satellites. The resulting observables are no longer a function of the receiver clock biases. The double differenced pseudorange, expressed in Equation (2.5), is only a function of the relative position of the two receivers and noise.

$$\nabla\Delta\rho^{st}_{ab} = r^{st}_{ab} + v^{st}_{ab} \tag{2.5}$$

As seen in Equation (2.6), the double differenced carrier phase contains the relative position, the relative carrier phase ambiguity and noise.

$$\nabla\Delta\phi_{ab}^{st} = r_{ab}^{st} + \lambda N_{ab}^{st} + v_{ab}^{st} \tag{2.6}$$

It is important to note that the single differenced and double differenced observables are not the only valuable combinations of the pseudorange and carrier phase measurements. Additional combinations include the widelane and narrowlane observables. These observables minimize noise or maximize wavelength to assist in integer ambiguity resolution. They are not discussed further in this thesis, but for additional information see [20] and [35].

2.2 Algorithm

Estimation of the RPV between two receivers using DRTK is a multistage process. First, the carrier phase ambiguities are estimated as floating point values. Then fixed integer estimates of the ambiguities are computed. The fixed integer estimate is subtracted from the carrier phase measurement and the RPV is estimated. The complete process is a combination of a Kalman filter (floating point ambiguity estimation) , the LAMBDA method (ambiguity integer fixing), and least squares estimation (relative position vector estimation).

2.2.1 Kalman Filter Floating Point Ambiguity Estimation

Carrier phase ambiguities are initially estimated in a Kalman Filter. Specifically, it is the single differenced ambiguities that are being estimated. The state vector, shown in Equation (2.7), contains L1 and L2 frequency single differenced ambiguity states for each visible satellite.

$$x = \begin{bmatrix} N_{ab_{L1}}^{1} & \cdots & N_{ab_{L1}}^{m} & N_{ab_{L2}}^{1} & \cdots & N_{ab_{L2}}^{m} \end{bmatrix}^{\mathbf{T}} \tag{2.7}$$

Therefore x is a column vector of length $2m$, where m is the number of satellite seen simultaneously by both receivers. Note that this assumes that each receivers provides L1 and L2 frequency measurements for each visible satellite.

2.2.1.1 Measurement Model

Constructing the measurement equation to fit the form of the Kalman filter, $z = Hx$, is not a trivial undertaking. The single difference pseudorange and carrier phase measurements are a function of two unknown terms plus the stochastic noise term. In order to estimate the carrier phase ambiguity, the relative range term, r^s_{ab}, must be removed from the equation. The single differenced pseudorange and carrier phase originally defined in Equation (2.3) and Equation (2.4) are rewritten in matrix form in Equation (2.8).

$$\begin{bmatrix} \Delta\rho^s_{ab} \\ \Delta\phi^s_{ab} \end{bmatrix} = \begin{bmatrix} u^s_{a_x} & u^s_{a_y} & u^s_{a_z} & 1 \\ u^s_{a_x} & u^s_{a_y} & u^s_{a_z} & 1 \end{bmatrix} \begin{bmatrix} r^s_{ab_x} \\ r^s_{ab_y} \\ r^s_{ab_z} \\ cdt_{ab} \end{bmatrix} + \begin{bmatrix} 0 \\ \lambda \end{bmatrix} N^s_{ab} \tag{2.8}$$

The non-deterministic terms are ignored for simplicity. The true range between receiver a and receiver b is decomposed into the line of sight unit vector from receiver a to satellite s and the x, y, and z components of the RPV in the Earth Center Earth Fixed (ECEF) frame. For a description of the ECEF frame see [12]. The matrix containing the unit vectors and a column of ones corresponding to the relative clock bias term is referred to here as the geometry matrix.

Equation (2.8) assumes that the unit vector from receiver a to satellite s is approximately equal to the unit vector from receiver b to satellite s. Formulation of the vector product of the RPV using this assumption is shown in Equation (2.9), Equation (2.10) and Equation

(2.11).

$$r^s_{ab} = \begin{bmatrix} u^s_{b_x} & u^s_{b_y} & u^s_{b_z} \end{bmatrix} \begin{bmatrix} r^s_{b_x} \\ r^s_{b_y} \\ r^s_{b_x} \end{bmatrix} - \begin{bmatrix} u^s_{a_x} & u^s_{a_y} & u^s_{a_z} \end{bmatrix} \begin{bmatrix} r^s_{a_x} \\ r^s_{a_y} \\ r^s_{a_x} \end{bmatrix} \tag{2.9}$$

$$\begin{bmatrix} u^s_{a_x} & u^s_{a_y} & u^s_{a_z} \end{bmatrix} \approx \begin{bmatrix} u^s_{b_x} & u^s_{b_y} & u^s_{b_z} \end{bmatrix} \tag{2.10}$$

$$r^s_{ab} = \begin{bmatrix} u^s_{a_x} & u^s_{a_y} & u^s_{a_z} \end{bmatrix} \begin{bmatrix} r^s_{b_x} - r^s_{a_x} \\ r^s_{b_y} - r^s_{a_y} \\ r^s_{b_x} - r^s_{a_z} \end{bmatrix} \tag{2.11}$$

To estimate the single differenced ambiguity, N^s_{ab}, in Equation 2.8, it must be isolated from the range information contained in the single differenced pseudorange and carrier phase observables. This is done by premultiplying each term in Equation 2.8 by the left null space of the geometry matrix. The left null space of matrix G is defined as the set of all vectors $\vec{a}$ such that $\vec{a}^T G = 0$. By multiplying Equation 2.8 by the left null space of the geometry matrix, L defined in Equation 2.12, the lead term on the right hand side of the equation is removed.

$$L = leftnull \left(\begin{bmatrix} \begin{matrix} 1 & \cdots & m \\ u_{a_x} & & \end{matrix}^{\mathbf{T}} & \begin{matrix} 1 & \cdots & m \\ u_{a_y} & & \end{matrix}^{\mathbf{T}} & \begin{matrix} 1 & \cdots & m \\ u_{a_z} & & \end{matrix}^{\mathbf{T}} & \begin{matrix} \\ 1 \end{matrix} \\ \begin{matrix} 1 & \cdots & m \\ u_{a_x} & & \end{matrix}^{\mathbf{T}} & \begin{matrix} 1 & \cdots & m \\ u_{a_y} & & \end{matrix}^{\mathbf{T}} & \begin{matrix} 1 & \cdots & m \\ u_{a_z} & & \end{matrix}^{\mathbf{T}} & \begin{matrix} \\ 1 \end{matrix} \\ \begin{matrix} 1 & \cdots & m \\ u_{a_x} & & \end{matrix}^{\mathbf{T}} & \begin{matrix} 1 & \cdots & m \\ u_{a_y} & & \end{matrix}^{\mathbf{T}} & \begin{matrix} 1 & \cdots & m \\ u_{a_z} & & \end{matrix}^{\mathbf{T}} & \begin{matrix} \\ 1 \end{matrix} \\ \begin{matrix} 1 & \cdots & m \\ u_{a_x} & & \end{matrix}^{\mathbf{T}} & \begin{matrix} 1 & \cdots & m \\ u_{a_y} & & \end{matrix}^{\mathbf{T}} & \begin{matrix} 1 & \cdots & m \\ u_{a_z} & & \end{matrix}^{\mathbf{T}} & \begin{matrix} \\ 1 \end{matrix} \end{bmatrix} \right) \tag{2.12}$$

The measurement vector z, shown in Equation 2.13, remains on the left hand side with the single differenced pseudorange and carrier phase measurements multiplied by L. The

equation shows the vector of single differenced L1 and L2 measurements from satellites 1 to m.

$$z = L \left[\begin{array}{cccc} \Delta\rho_{ab_{L1}}^{1\cdots m} & \Delta\rho_{ab_{L2}}^{1\cdots m} & \Delta\phi_{ab_{L1}}^{1\cdots m} & \Delta\phi_{ab_{L2}}^{1\cdots m} \end{array} \right]^{\mathbf{T}} \tag{2.13}$$

The coefficient matrix for the state vector is now L times the matrix containing rows of zeros corresponding to the single differenced pseudorange measurement and rows containing the appropriate wavelength corresponding to the single differenced carrier phase measurements. The matrix is represented in Equation 2.14.

$$H = L \left[\begin{array}{cc} 0_{2m\times m} & 0_{2m\times m} \\ \lambda_{L1} I_{m\times m} & 0_{m\times m} \\ 0_{m\times m} & \lambda_{L2} I_{m\times m} \end{array} \right] \tag{2.14}$$

The measurement equation now fits the $z = Hx$ form of the Kalman filter. The update step of the filter follows the implementation shown in Equations (2.15) through (2.17).

$$K_k = P_k^- H_k^{\mathbf{T}} (H_k P_k^- H_k^{\mathbf{T}} + R_k)^{-1} \tag{2.15}$$

$$P_k^+ = (I - K_k H_k) P_k^- \tag{2.16}$$

$$\hat{x}_k^+ = \hat{x}_k^- + K_k (z_k - H_k \hat{x}_k^-) \tag{2.17}$$

The Kalman gain K is calculated as a function of the error covariance matrix P, the measurement matrix H, and the uncertainty in the measurement R. The error covariance matrix and the state vector are then updated using the gain, the measurement matrix, and the a priori estimates and error covariance. The initialization of the state vector and the error covariance matrix are discussed in Section 2.2.1.3 along with the calculation of the measurement uncertainty. For derivation of the Kalman filter measurement update see [2].

2.2.1.2 Propagation Model

Assuming the GPS receiver maintains lock on the signal from a given satellite between measurements, the carrier phase ambiguity remains constant. Therefore, the state transition matrix is the identity matrix with dimension equal to the number of single differenced ambiguity estimates. Since the ambiguities are known to be constant with certainty the process noise vector can be set to zero. However, to prevent the error covariance from settling to a small value that results in a zero gain matrix, the process noise matrix,Q, is set to 1×10^{-6} times the identity matrix of with dimension equal to the number of single differenced ambiguity estimates. The state estimates and error covariance matrix are propagated with the standard Kalman time update equations shown in Equation 2.18 and Equation 2.19.

$$\hat{x}_{k+1}^{-} = \Phi_k \hat{x}_k^{+} \tag{2.18}$$

$$P_{k+1}^{-} = \Phi_k P_k^{+} \Phi_k^{\mathbf{T}} + Q \tag{2.19}$$

The state transition matrix and the process noise vector are represented by Φ and Q respectively.

2.2.1.3 Filter Initialization and Implementation

The state vector is initialized with single differenced pseudorange and carrier phase measurements from each satellite. The initial estimate of the single differenced ambiguities is equal to the difference between the single differenced pseudorange and single differenced carrier phase measurement as seen in Equation 2.20. The value is divided by the signal

wavelength to convert the estimate to units of cycles.

$$\hat{x} = \begin{bmatrix} (\Delta\rho^1_{ab_{l1}} - \Delta\phi^1_{ab_{l1}})/\lambda_{L1} \\ \vdots \\ (\Delta\rho^m_{ab_{l1}} - \Delta\phi^m_{ab_{l1}})/\lambda_{L1} \\ (\Delta\rho^1_{ab_{l2}} - \Delta\phi^1_{ab_{l2}})/\lambda_{L2} \\ \vdots \\ (\Delta\rho^m_{ab_{L2}} - \Delta\phi^m_{ab_{l2}})/\lambda_{L2} \end{bmatrix} \tag{2.20}$$

The error covariance matrix is initialized as the identity matrix multiplied by 1/2 to reflect the expected variance of the single differenced ambiguities. The initial uncertainty is selected to provide desired filter performance based on experimental testing. Obviously, the error covariance matrix is a square matrix with dimensions of $2m \times 2m$ where m is the number of visible satellites.

Measurement uncertainty, R, is calculated at each measurement update based on the expected variance as defined in [28] and [19]. GPS measurement variance is a function of receiver characteristics and the carrier to noise ratio, c/n_0, of the received signal. The expected pseudorange and carrier phase variances are given by Equation (2.21) and Equation (2.23) respectively with parameters defined in Table 2.1.

$$\sigma^2_\rho = \sigma^2_{\rho_{atm}} + \sigma^2_{DLL} \tag{2.21}$$

$$\sigma_{DLL} = \lambda_c \sqrt{\frac{4d^2 B_{n\rho}}{c/n_0}(2(1-d) + \frac{4d}{Tc/n_0})} \tag{2.22}$$

$$\sigma^2_\phi = \sigma^2_{\phi_{atm}} + \sigma^2_{PLL} \tag{2.23}$$

$$\sigma_{PLL} = \frac{\lambda_L}{2\pi}\sqrt{\frac{B_{n\phi}}{c/n_0}(1 + \frac{1}{Tc/n_0})} \tag{2.24}$$

The values for the receiver characteristics given in Table 2.1 are typical values taken from [19] and [21]. Note that the variances calculated from Equation (2.21) and Equation (2.23) represent the variance of individual pseudorange and carrier phase measurements. However,

Table 2.1: Pseudorange and Carrier Phase variance calculation parameters

Parameter	Description	Value
$\sigma^2_{\rho_{atm}}$	Variance due to atmospheric code delay	5.22 (m)
λ_c	Code chip width	293.05 (m)
d	Correlator spacing	0.5 (chips)
$B_{n\rho}$	Code loop noise bandwidth	2 (Hz)
T	Prediction integration time	2 (ms)
$\sigma^2_{\phi_{atm}}$	Variance due to atmospheric carrier delay	0.03 (m)
λ_L	Carrier wavelength	L1, L2 (m)
$B_{n\phi}$	Carrier loop noise bandwidth	18 (Hz)

the filter observables are a combination of measurements from two receivers. Therefore, R is a function of the measurement noise from receiver a and receiver b. Assuming that the measurement noise is uncorrelated between receivers and that the atmospheric delays have been removed through differencing, R is the diagonal matrix defined by Equation (2.25).

$$R = \begin{bmatrix} \sigma^2_{a_{DLL}} + \sigma^2_{b_{DLL}} & 0 \\ 0 & \sigma^2_{a_{PLL}} + \sigma^2_{b_{PLL}} \end{bmatrix} \tag{2.25}$$

Equation (2.25) shows R for one satellite for simplicity; in actuality R has dimensions equal to the two times number of visible satellites.

During filter operation, two conditions cause a modification of the dimensions of the state vector and the error covariance matrix. The first is a result of the changing satellite constellation. When a satellite that was previous being tracked by receivers a and b is lost that ambiguity estimate is removed from the state vector. The corresponding row and column of the error covariance matrix are also removed. Conversely, an additional ambiguity estimate is added to the state vector when a new satellite is acquired and the error covariance matrix is expanded to include the uncertainty in that estimate. The new ambiguity estimate and error covariance are initialized as before.

Cycle slips also cause a modification of the state vector. A cycle slip occurs when the receiver loses and reacquires lock on the carrier signal of a satellite between measurement

updates. In this case the actual carrier phase ambiguity changes, nullifying the previous estimate. Inclusion of the faulty estimate would severely degrade the RPV estimate. A cycle slip detection algorithm is executed on each new measurement before it is used in the update step. The single differenced pseudorange and carrier phase measurements from the current and previous time steps are used to compute a time differenced ambiguity estimate, shown in Equation (2.26).

$$dN^s_{k,k-1} = [(\Delta\rho^s_k - \Delta\phi^s_k) - (\Delta\rho^s_{k-1} - \Delta\phi^s_{k-1})]/\lambda \tag{2.26}$$

If this value exceeds a threshold, selected to be plus or minus one cycle for this work, the measurement is deemed to have experienced a cycle slip and the ambiguity estimate and the covariance are reset as if a new satellite were acquired.

2.2.2 Integer Fixing using the LAMBDA method

The second stage of RPV estimation is an attempt to fix the floating point ambiguity estimates to integer values. The Kalman filter provides estimates of the single differenced carrier ambiguities and a covariance matrix describing the uncertainty in the estimates. The single differenced estimates are transformed into double differenced values prior to integer fixing to remove residual receiver clock errors. Seeing that the transformation is a linear process, a transformation matrix is constructed to perform the operation. An example of a transformation matrix is given in Equation (2.27).

$$C^d_s = \begin{bmatrix} 1 & -1 & 0 & 0 & 0 \\ 0 & -1 & 1 & 0 & 0 \\ 0 & -1 & 0 & 1 & 0 \\ 0 & -1 & 0 & 0 & 1 \end{bmatrix} \tag{2.27}$$

In the example, the second of five single differenced ambiguities is chosen as the base estimate and is subtracted, via Equation (2.28), from the remaining estimates resulting in four double differenced ambiguity estimates.

$$\hat{N}_d = C_s^d \hat{N}_s \tag{2.28}$$

The transformation matrix is also applied to the covariance matrix as seen in Equation (2.29).

$$P_{N_d} = C_s^d P_{N_s} C_s^{d\mathbf{T}} \tag{2.29}$$

Intuitively, rounding is the most straightforward method of converting a floating point value to an integer. However, the Kalman filter yields ambiguity estimates which are highly correlated. This correlation can be seen in the off diagonal terms of the covariance matrix. Simply rounding the estimates to their nearest integer makes insufficient use of the available information. Optimal integer estimates take into account both the variance and covariance of each floating point ambiguity estimate. However, searching the multi-dimensional space defined by the total set of estimates is impractical. The LAMBDA method refines the search space by decorrelating the ambiguity estimates through a transformation [33]. This transformation results in a nearly diagonal covariance matrix which is used to calculate integer estimates of the carrier ambiguities. The integer ambiguities are computed in a sequential routine starting with the most certain estimate (lowest variance). The completed set is then transformed back into the original domain.

While the LAMBDA method does provide the most likely candidate set of integer ambiguities, they are not guaranteed to be correct [18]. The user must decide if the candidate set meets the requirements of the application. The decision criterion used here is known as the ratio test. Two candidate sets, $\breve{N}_1$ and $\breve{N}_2$, are computed via the LAMBDA method and their deviations, d, from the original floating point ambiguity estimates, $\hat{N}$, are calculate

using Equation (2.30).

$$d_i = (\hat{N} - \breve{N}_i)P_N^{-1}(\hat{N} - \breve{N}_i)^{\mathbf{T}} \tag{2.30}$$

If the ratio of the deviations, d_2/d_1, exceeds a selected threshold, the most likely candidate, $\breve{N}_1$, is retained and used to compute a high precision RPV. A threshold of three was used in this work based on the results seen in [34].

2.2.3 Least Squares Relative Position Vector Estimation

The final step of the DRTK algorithm is the estimation of the RPV between the GPS receivers. The first two steps of the algorithm provide the best available estimate of the double differenced carrier phase ambiguities. Ideally, fixed integer estimates are successfully computed with the LAMBDA method but the RPV is estimated regardless of the results of the ratio test. The RPV estimate is therefore designated as a high precision (HPRPV) estimate in the case that the integer estimates are available or a low precision (LPRPV) estimate when the floating point estimate must be used. The solution procedure is same regardless of the precision of the ambiguity estimates. Equation (2.31) shows the form of the RPV estimate problem derived from Equation (2.6) and Equation (2.11).

$$\nabla\Delta\phi_{ab} - \lambda\nabla\Delta N_{ab} = \Delta\vec{u}_a\vec{r}_{ab} + v_{ab} \tag{2.31}$$

Note that the Δ preceding the unit vector signifies that the base unit vector has been subtracted to form the correct geometry and that the satellite notation has been removed for clarity. The RPV is estimated using least squares as shown in Equation (2.32).

$$\vec{r}_{ab} = (\Delta\vec{u_a}^{\mathbf{T}}\Delta\vec{u_a})^{-1}\Delta\vec{u_a}^{\mathbf{T}}(\nabla\Delta\phi_{ab} - \lambda\nabla\Delta N_{ab}) \tag{2.32}$$

A weighted least squares formulation may also be implemented to incorporate the measurement uncertainty described in Section 2.2.1.3.

2.3 Low Cost Alternative

In the previous section, a DRTK algorithm incorporating both L1 and L2 frequency measurements was described. A goal of this thesis is to develop a single frequency alternative and to evaluate any performance limitations. Single frequency receivers are far cheaper than their dual frequency counterparts. Typically, single frequency receivers can be purchased for less than $200 while dual frequency receivers can cost several thousands of dollars. Single frequency antennas can be purchased at reduced cost as well.

The single frequency algorithm follows the same multistage process as the dual frequency algorithm. First, the carrier phase ambiguities are estimated in a Kalman filter. The state vector, measurement matrix, and measurement vector are modified to contain only L1 information as seen in Equations (2.33) through (2.36) (Note: L2 only implementation is also possible).

$$x = \begin{bmatrix} N^1_{ab_{L1}} & \cdots & N^m_{ab_{L1}} \end{bmatrix}^{\mathbf{T}} \tag{2.33}$$

$$z = L \begin{bmatrix} \Delta\rho^{1\cdots m}_{ab_{L1}} & \Delta\phi^{1\cdots m}_{ab_{L1}} \end{bmatrix}^{\mathbf{T}} \tag{2.34}$$

$$H = L \begin{bmatrix} 0_{m\times m} \\ \lambda_{L1} I_{m\times m} \end{bmatrix} \tag{2.35}$$

$$L = leftnull\left(\begin{bmatrix} \begin{matrix} 1 & \cdots & m \\ u_{a_x} & & \end{matrix}^{\mathbf{T}} & \begin{matrix} 1 & \cdots & m \\ & u_{a_y} & \end{matrix}^{\mathbf{T}} & \begin{matrix} 1 & \cdots & m \\ & u_{a_z} & \end{matrix}^{\mathbf{T}} & \begin{matrix} \\ \\ 1 \end{matrix} \\ \begin{matrix} 1 & \cdots & m \\ u_{a_x} & & \end{matrix}^{\mathbf{T}} & \begin{matrix} 1 & \cdots & m \\ & u_{a_y} & \end{matrix}^{\mathbf{T}} & \begin{matrix} 1 & \cdots & m \\ & u_{a_z} & \end{matrix}^{\mathbf{T}} & \begin{matrix} \\ \\ 1 \end{matrix} \end{bmatrix} \right) \tag{2.36}$$

The Kalman filtering stage is implemented as described in Section 2.2.1.3. Again, the LAMBDA method is used to develop integer estimates of the double differenced ambiguities and the RPV is estimated in a least squares routine. However, the reduction in the number of available measurements both increases the uncertainty in the ambiguity estimates and decreases the likelihood of successfully fixing integers. Figure 2.1 shows the increased variance of the single frequency ambiguity estimates and the ratio test calculated from data

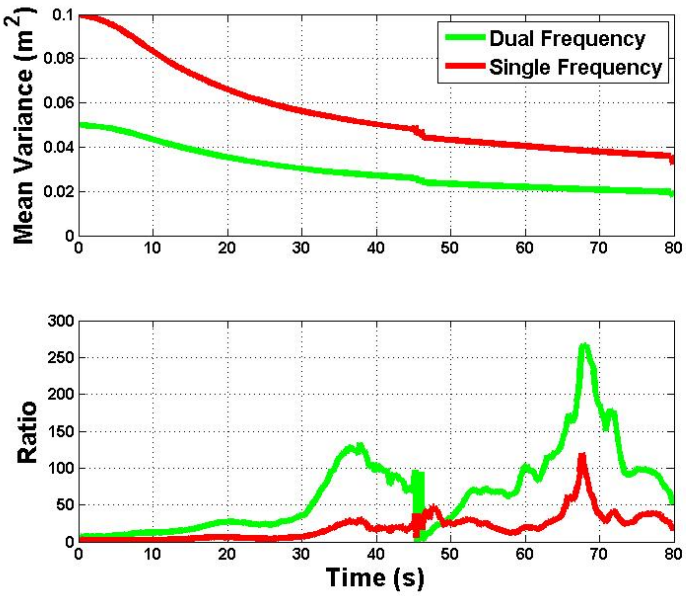

Figure 2.1: Single and dual frequency mean ambiguity variance and the corresponding ratio test from GPS data

collected on two dual frequency receivers. The same data set was processed with the dual and single frequency algorithm (simply ignoring the L2 measurements in single frequency calculations). It can be seen that the ratio test results from the single frequency algorithm are consistently lower than the dual frequency algorithm. Despite this drawback, the single frequency algorithm is capable of producing highly accurate results as long as the ratio test is passed. Assuming that both algorithms settle on the same set of integers, the RPV estimate calculated by the single frequency algorithm will be based on a subset of the same data used in the dual frequency estimation. Recall that the ratio test threshold value of three was selected in Section 2.2.2 with values greater than the threshold passing the test. Clearly, the single frequency ratio exceeds the selected threshold for a majority of the data set. In additional analysis, the single frequency algorithm was not as successful in passing the ratio test. Overall, the ratio test was passed on 24.8 percent of all measurement epochs using only L1 frequency measurements as compared to 62.8 percent using both L1 and L2 frequency measurements. Additional analysis of the single and dual frequency algorithms is provided in the next section.

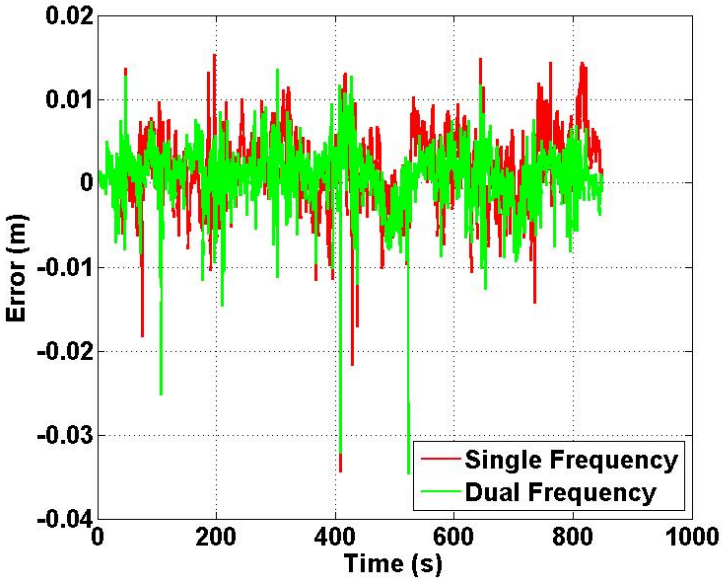

Figure 2.2: High precision baseline error calculated with the single and dual frequency algorithms for a dynamic data set from two vehicles

2.4 Experimentation and Results

To compare the performance of the single and dual frequency algorithms, data was collected with two Novatel Propak V3 receivers mounted on two Infiniti G35 sedans. A Septentrio Pola RX2 receiver was used as a base station to calculate a RTK position solution to be used as reference data. The receivers output L1 and L2 frequency measurements at 5Hz. Pseudorange and carrier phase measurements were recording at varying separation distances in both stationary and dynamic scenarios. The performance of the algorithms was evaluated based on accuracy and the availability of a high precision solution.

The accuracies of the single and dual frequency DRTK algorithms were determined by comparing the estimated RPV to the difference in the RTK reference solutions to the two receivers. Both low precision and high precision RPVs were examined. The low precision solution was computed at every measurement update while the high precision solution was computed only when three or more fixed integer ambiguity estimates were available. Figure 2.2 and Figure 2.3 show the high precision and low precision results of a typical test run.

Table 2.2: Statistics on HP and LP Baseline Errors

	High Precision		Low Precision	
	RMSE (cm)	Variance (cm^2)	RMSE (cm)	Variance (cm^2)
Dual Frequency	0.33	0.10	20.87	430
Single Frequency	0.45	0.18	24.52	600

The error in the magnitude of the RPV is plotted verse time. Note that the magnitude of the RPV will also be referred to as the baseline. Clearly, the dual frequency and single frequency high precision results show errors of similar magnitude throughout the run. As would be expected the error is highly correlated between the two algorithms with the single frequency algorithm producing slightly higher variance. The absolute value of the baseline error does not exceed 4 cm for either algorithm. The root mean squared error (RMSE) and variance of both the high and low precision solutions for each algorithm are provided in Table 2.2.

The low precision errors are typically slightly more than one order of magnitude higher than the high precision errors. Here the maximum error for each algorithm is nearly 80 centimeters. This is still a marked improvement over the expected error of the standalone GPS solution which is generally several meters. Again the errors are highly correlated with higher variance seen in the single frequency solution.

RPV estimates were calculated for a variety of separation distances and the resulting errors in the high precision solutions are shown in Figure 2.4. The majority of the errors for each algorithm do not exceed 20 centimeters but it is apparent that the variance increases slightly as the separation distance increases. Also notice that at a separation distance of approximately 600 meters the dual frequency algorithm produces a high precision solution while the single frequency algorithm does not. This portion of the data was collected during a static test as can be seen by the constant separation distance. Approximately ten minutes of data was collected during each static test and both the single and dual frequency algorithms successfully estimated integer ambiguities for separation distances of 8, 150, and 350 meters. However, the ratio test was not passed using only L1 frequency measurements with 600 meters of separation.

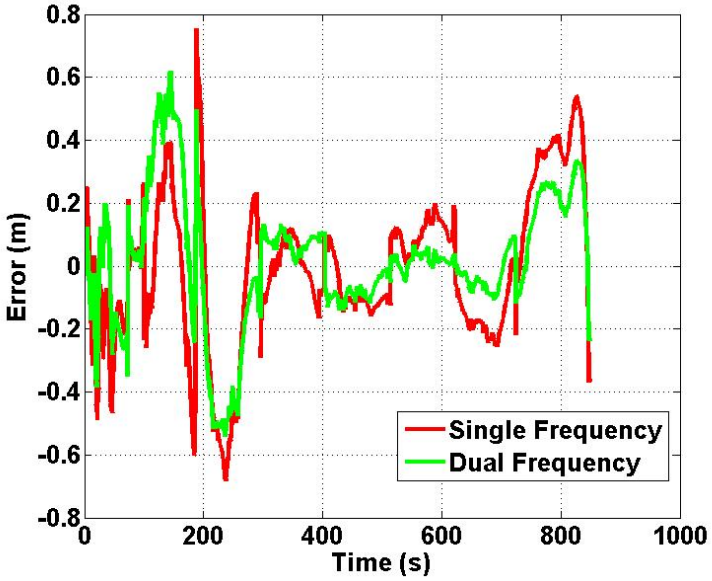

Figure 2.3: Low precision baseline error calculated with the single and dual frequency algorithms for a dynamic data set from two vehicles

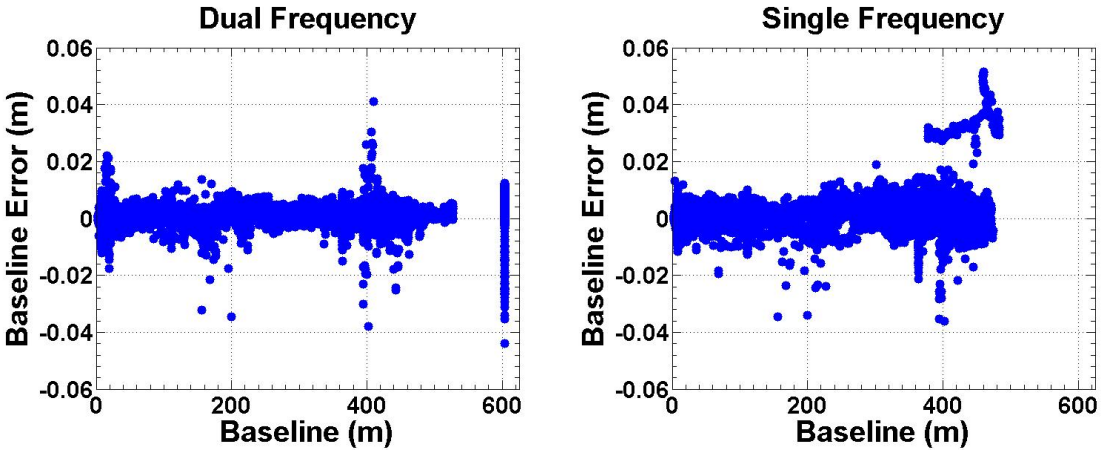

Figure 2.4: Dual and single frequency errors as a function of the separation distance

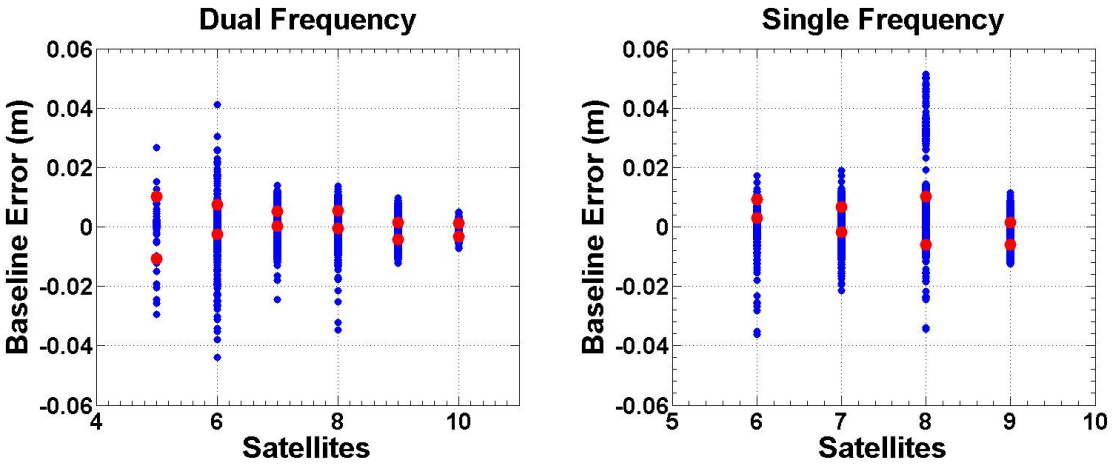

Figure 2.5: Dual and single frequency errors as a function of the number of visible satellites

The accuracy of the high precision solution from each algorithm was also evaluated based on the number of satellites being tracked by each receiver. Figure 2.5 shows the single and dual frequency results for various numbers of satellites with the red dots corresponding to the one sigma bounds of the error. Again, the accuracy of each algorithm is comparable but the algorithms can be differentiated by the availability of a high precision solution. With both L1 and L2 frequency measurements a high precision solution is calculated when tracking as few as five satellites. A minimum of six satellites were required to successfully fix integers when using only L1 frequency measurements.

It has been established that the primary difference in the single and dual frequency algorithms is the availability of a high precision solution. To quantify this difference, the time to first fix (TTFF) for each algorithm was calculated. The TTFF is time required to fix floating point ambiguity estimates to integer values. The TTFF for each algorithm is shown in Figure 2.6 as a function of the number of visible satellites. Statistics on the TTFF for each algorithm are also provided in Table 2.3. The mean TTFF for the dual frequency algorithm is approximately 0.2 seconds which corresponds to two measurement epochs. The single frequency mean TTFF is significantly higher at almost 2.5 seconds or approximately 12 measurement epochs. It is also important to note that the mean TTFF with L1 measurements only increases considerably as the number of satellites decreases. In

Table 2.3: Statistics on the TTFF

	Mean (s)						Standard Deviation (s)					
Satellites	9+	8	7	6	5	Total	9+	8	7	6	5	Total
Dual	0.20	0.07	0.28	0.26	0.14	0.18	0.50	1.10	4.24	5.24	2.89	3.52
Single	2.44	4.90	7.74	6.21	NA	4.29	14.33	36.17	32.96	30.07	NA	24.70

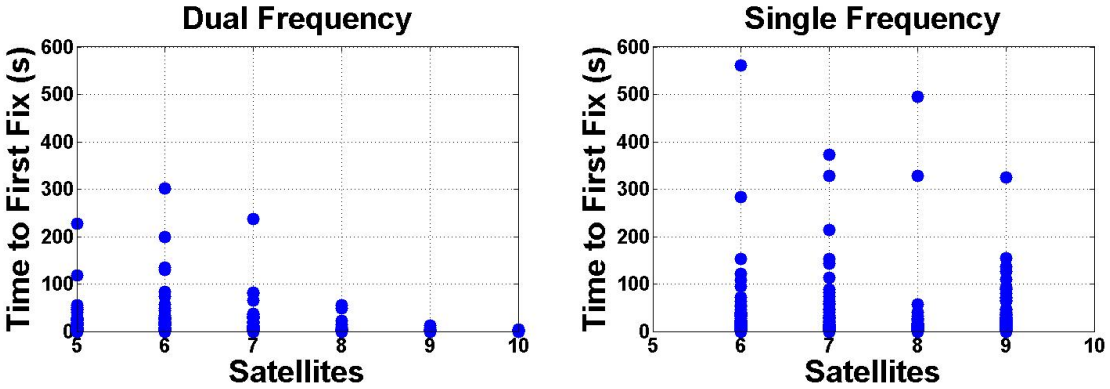

Figure 2.6: Dual and single frequency TTFF as a function of the number of visible satellites

comparison, the mean TTFF using both L1 and L2 measurements is not effected by the number of satellites but an increase in the standard deviation is seen as the number of satellites decreases.

2.5 Conclusions

Single and dual frequency DRTK algorithm were developed and compared based on their accuracy and the availability of a high precision solution. The accuracy of both the low precision and the high precision RPV estimates of each algorithm were significantly better than the traditional standalone GPS solution. The high precision baseline errors for each algorithm was predominantly sub-centimeter. It is important to note that the residual error of the DRTK algorithm is correlated with the residual error of the reference RTK solution, so the reported errors may be slightly optimistic. The RTK solution is reported to be accurate to the centimeter level and by comparison the DRTK algorithm errors are of the same order of magnitude.

High precision solution availability proved to be the primary difference in the performance of the single and dual frequency algorithms. The mean TTFF of the single frequency algorithm was 9 seconds for a variety of operational scenarios while the dual frequency algorithm fixed integers in 0.2 seconds on average.

From the analysis, the single frequency algorithm is an effective alternative to the dual frequency algorithm depending on the system requirements. Given that GPS availability is high in the operational environment and that time can be given to allow the algorithm to fix integers, the single frequency provides similar performance to the dual frequency algorithm. If operation in poor GPS environments or immediate integer fixing are design requirement, the dual frequency algorithm should be implemented.

Chapter 3

DRTK and IMU Integration

The DRTK algorithm described in Chapter 2 provides RPV estimates at the output rate of the GPS receiver, typically less than 10 Hz. By incorporating IMU measurements in the navigation algorithm, the RPV can be estimated at five to ten times the rate of the GPS only solution. In this chapter, GPS and IMU integration is discussed and possible architectures are evaluated to determine the best method of data fusion for relative navigation of ground vehicles.

3.1 GPS and IMU Integration

GPS and IMU are combined in integrated navigation solutions to take advantage of the complimentary nature of each unit's strengths and weaknesses. The strength of GPS lays in its ability to provide a global navigation solution with predictable long term accuracy. However, the GPS position solution is prone to meter level jumps and intermittent outages due to faulty measurements, changing satellite geometry, and environmental interference. The IMU is used to smooth jumps in the GPS position solution and bridge short GPS outages. The IMU navigation solution requires global position initialization and periodic updates to bound dead reckoning error growth due to integrated errors and noise. The combined navigation system provides a smooth high rate solution with immunity to short GPS outages.

At this point it is valuable to differentiate between an IMU and an inertial navigation system (INS). The IMU is the device measuring the specific forces and angular rates acting on the sensor platform. Combining these measurements with a navigation processor constitutes an INS. The navigation processor is responsible for maintaining the orientation of the sensor

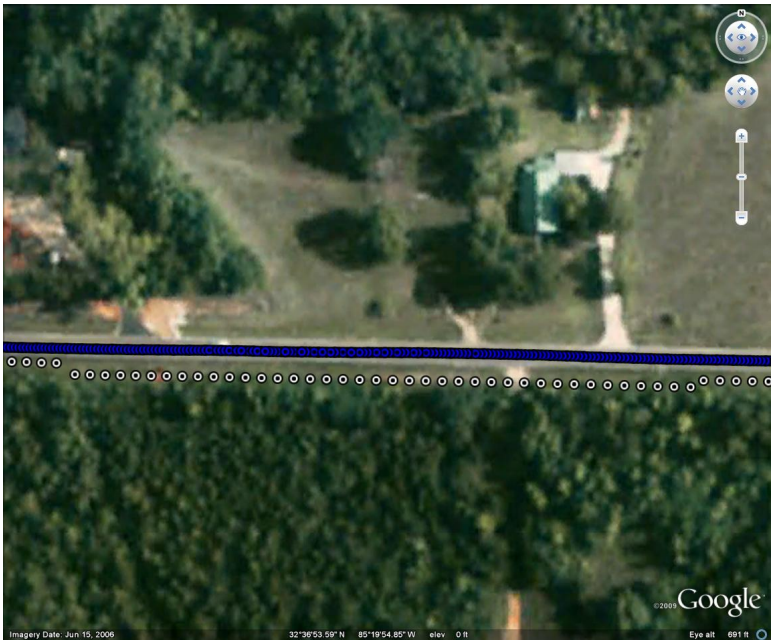

Figure 3.1: GPS/INS filtered solution with erroneous stand alone GPS solution

frame relative to the navigation frame and computing position and velocity estimates from the IMU measurement. This process is described in detail in the next section.

A comparison of a standalone GPS position solution and a GPS/INS position solution is shown in Figures 3.1 and 3.2. Note that the background maps were made available through *GPS Visualizer*. In each figure the GPS only solution, as reported by a Novatel Propak V3 receiver, is shown in white and the GPS/INS solution is shown in blue. The GPS/INS solution was calculated post process by combining pseudorange measurements from the Novatel receiver with measurements from a Crossbow IMU440. These sensors were affixed to a test vehicle traveling on a two lane county road. Figure 3.1 shows the standalone GPS solution jump off the road by several meters while the GPS/INS solution maintains its position on the road.

In Figure 3.2, the vehicle travels under an overpass and predictably the standalone GPS solution is lost momentarily. The GPS/INS algorithm continues to output a solution by dead reckoning with IMU measurements only until GPS returns. When satellite signals are reacquired on the north side the overpass, a correction of the of INS solution can be seen.

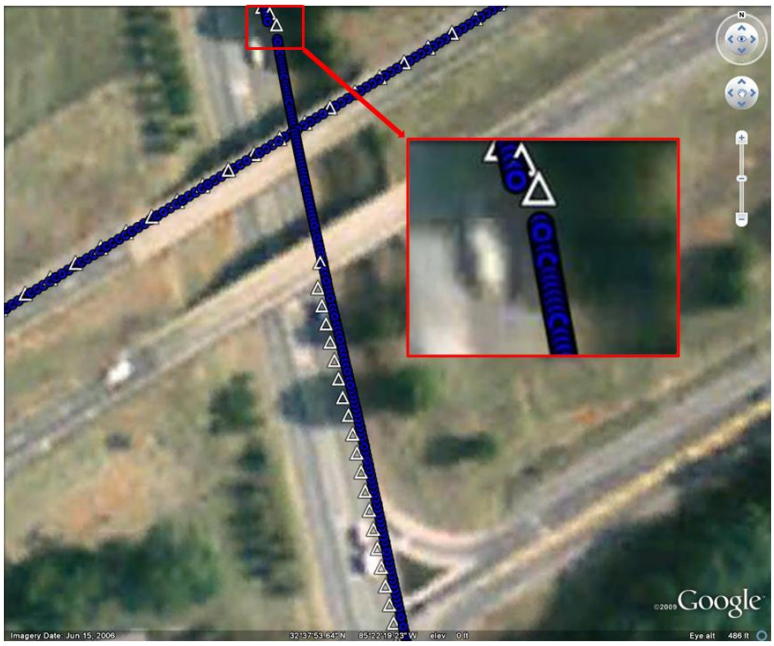

Figure 3.2: IMU dead reckoning under an overpass during GPS outage

GPS/INS integration architectures can be classified into three categories: loosely coupled, tightly coupled, or deeply coupled. Variation of the method of integration and on the names given to each category are found in the literature but generally the coupling architectures can be differentiate based on GPS measurements used to correct INS propagation errors [17]. For example, the term loosely coupled indicates that GPS position and velocity estimates are used to update the INS solution. Tightly coupled GPS/INS architectures utilize GPS pseudorange, carrier phase, and/or pseudorange rate measurements to update the INS solution. Deep coupling of GPS and INS is performed at the signal processing level. In-phase and quadraphase correlator outputs from the receiver tracking channels are used as inputs to the navigation filter. The navigation filter feeds oscillator corrections back to the GPS receiver and INS corrections to the navigation processor to update position estimates. Figure 3.3 provides a visual representation of the three architectures.

Each integration method has advantages and disadvantages. The loosely coupled architecture is relatively simple to implement but ignores valuable information when the GPS receiver is not capable of computing a position solution due to limited satellite visibility (less

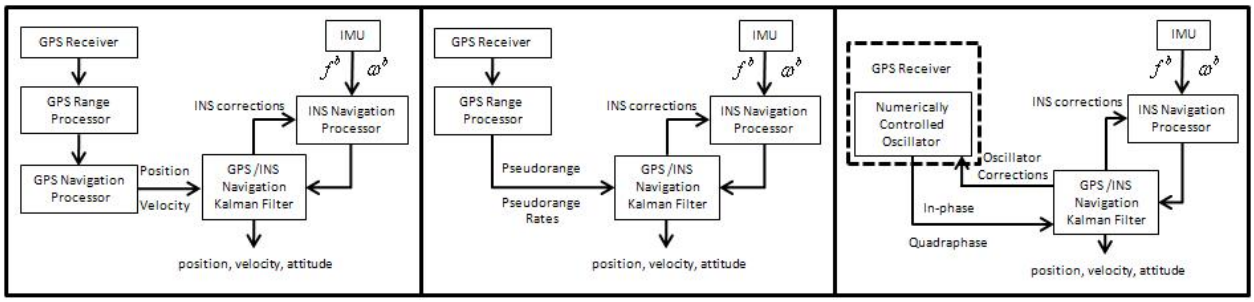

Figure 3.3: GPS/INS coupling architectures from left to right - loosely coupled, tightly coupled, and deeply coupled

than four satellites). Tight coupling avoids this deficiency by using all available pseudorange and Doppler measurements whether the complete GPS solution is available or not. The deeply coupled architecture excels in this area by improving the signal tracking capability of the GPS receiver thereby maximizing the number of available GPS observables. Of course, implementation becomes increasing difficult moving from loose to tight to deep integration. One additional consideration for this work is the quality of the available measurements. Deep coupling maximizes the available information often at the expense of quality. Signal tracking at low carrier to noise ratios, the specialty of deeply coupled filters, can leads to degraded measurements. Since the algorithms developed here are acutely dependent on measurement quality, tight coupling is chosen as the basis for GPS/INS filter design.

3.2 Tightly Coupled GPS/INS

The tightly coupled GPS/INS navigation filter is founded on the INS position, velocity, and attitude (PVA) solution. PVA estimates are computed in the INS navigation processor and errors are tracked in an error state Kalman filter. The estimated errors are fed back to the navigation processor and a corrected navigation solution is output.

3.2.1 INS Navigation Processor

Position, velocity and attitude estimation in the INS navigation processor is a multi-stage process. The steps of the estimation procedure are shown in Figure 3.4. Clearly

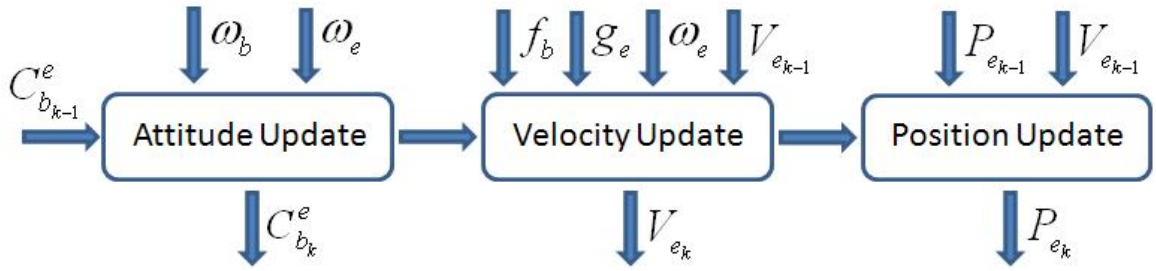

Figure 3.4: INS navigation processor steps

from the figure, a priori attitude, velocity, and position information is required for estimate propagation. For now it is assumed that estimates of the initial conditions of the states are available. The additional terms in the figure represent the IMU measurements of angular rate, ω_b, and specific force, f_b, and the local acceleration due to gravity, g_e, and the rotation rate of the Earth, ω_e.

The first step in the navigation processor is the attitude update. Attitude information is maintained in the form of a transformation matrix relating the platform body frame to the chosen navigation frame. The ECEF frame is the navigation frame in this work and therefore the transformation matrix is defined by the Euler rotation angles relating the body frame and the ECEF frame. The Euler roll, pitch, and yaw angles, (ϕ, θ, ψ), define three rotations transforming a vector in a given reference frame to a new frame. The Euler angles ϕ^e_b, θ^e_b, and ψ^e_b, relate the body frame, b, to the ECEF frame, e, and the rotations associated with these angle are shown in matrix form in Equations (3.1) through (3.3).

$$R_1 = \begin{bmatrix} 1 & 0 & 0 \\ 0 & \cos\phi^e_b & \sin\phi^e_b \\ 0 & -\sin\phi^e_b & \cos\phi^e_b \end{bmatrix} \tag{3.1}$$

$$R_2 = \begin{bmatrix} \cos\theta^e_b & 0 & -\sin\theta^e_b \\ 0 & 1 & 0 \\ \sin\theta^e_b & 0 & \cos\theta^e_b \end{bmatrix} \tag{3.2}$$

$$R_3 = \begin{bmatrix} \cos\psi_b^e & \sin\psi_b^e & 0 \\ -\sin\psi_b^e & \cos\psi_b^e & 0 \\ 0 & 0 & 1 \end{bmatrix} \tag{3.3}$$

The resulting transformation matrix, C_b^e, is computed as shown in Equation (3.4).

$$C_b^e = [R_1][R_2][R_3] \tag{3.4}$$

On each IMU measurement, the transformation matrix is updated using the measured angular rates, ω_b. Note that the measurements are in the IMU frame which is assumed to be consistent with the platform body frame. Using a small angle approximation, the rate of change of the transformation matrix is approximated by

$$\dot{C}_b^e = C_b^e \Omega_{ib} - \Omega_{ie} C_b^e \tag{3.5}$$

where Ω_{ib} is the rotation of the body frame relative to an inertial frame expressed in skew-symmetric form and Ω_{ie} is the rotation of the ECEF frame relative to an inertial frame also expressed in skew-symmetric form. The ECEF frame rotates with the Earth and that rotation is assumed to be constant here and given by the vector, $\omega_e = [\ 0 \quad 0 \quad 7.292115 \times 10^{-5}\ ]^{\mathbf{T}}$ in units of radians per second [17]. The rotation of the body frame is measured by the IMU and is given by the vector ω_b. The skew-symmetric form is defined in Equation (3.6) for an arbitrary vector of rotations $(\omega_x, \omega_y, \omega_z)$.

$$\Omega = [(\omega_x, \omega_y, \omega_z)]_\times = \begin{bmatrix} 0 & -\omega_z & \omega_y \\ \omega_z & 0 & -\omega_x \\ -\omega_y & \omega_x & 0 \end{bmatrix} \tag{3.6}$$

Equation (3.5) is integrated assuming that Ω_{ib} and Ω_{ie} are constant over the IMU measurement interval, Δt, and C_b^e is propagated using Equation (3.7).

$$C_{b_k}^e = C_{b_{k-1}}^e (I + \Omega_{ib}\Delta t) - \Omega_{ie} C_{b_{k-1}}^e \Delta t \tag{3.7}$$

The current transformation matrix and the accelerometer measurements are then used to update the velocity estimate. Specific forces measured by the IMU, denoted as f_b, must be rotated into the navigation frame prior to use. This is done by multiplying the measured specific forces by the transformation matrix as seen in Equation (3.8).

$$f_e = C_b^e f_b \tag{3.8}$$

The specific force measurement is corrected to account for gravity and Coriolis effects and the estimated velocity is propagated using Equation (3.9).

$$V_{e_k} = V_{e_{k-1}} + (f_e + g_e - 2\Omega_{ie} V_{e_{k-1}})\Delta t \tag{3.9}$$

The acceleration due to gravity, g_e, is calculated based on the ECEF position of the platform using the model described in [37].

Finally, the position estimate is updated by Euler integration using the current velocity estimates as given in Equation (3.10).

$$P_{e_k} = P_{e_{k-1}} + V_{e_k}\Delta t \tag{3.10}$$

Since the INS solution is depended on integration of IMU measurements known to contain errors due to misalignment, biases and noise, the PVA estimates will diverge from the true value over time. Corrections in the form of GPS measurements are used to bound this drift. The pose error due to IMU errors is estimated in an extended Kalman filter described in the next section.

3.2.2 Kalman Filter

INS solution errors are estimated in an extended Kalman filter with 17 states as shown in Equation (3.11).

$$x = \begin{bmatrix} \delta P_e & \delta V_e & \delta \Psi_e & b_a & b_g & cdt & c\dot{dt} \end{bmatrix}^{\mathbf{T}} \tag{3.11}$$

Each of the first five terms in the state vector represent three dimensional components which from left to right are the position error, velocity error, attitude error, accelerometer biases, and gyroscope biases. The pose error states (position, velocity, and attitude) are estimated in the ECEF frame while the bias states are estimated in the platform body frame. The last two states are estimates of the GPS receiver clock bias and clock drift.

3.2.2.1 Measurement Model

As stated in Section 3.1, in a tightly coupled GPS/INS filter the INS navigation solution is corrected using pseudorange and pseudorange rate measurements from GPS. The measured pseudoranges and pseudorange rates are compared to predicted values derived from the INS navigation solution. Equations (3.12) and (3.13) are used to compute the predicted the pseudorange and pseudorange rate from the receiver to satellite s where P_{s_e} is the position of satellite s in ECEF coordinates.

$$\hat{\rho}_s = \sqrt{(P_e - P_{s_e}) \cdot (P_e - P_{s_e})^{\mathbf{T}}} + cdt \tag{3.12}$$

$$\hat{\dot{\rho}}_s = \frac{(P_e - P_{s_e})^{\mathbf{T}} \cdot (V_e - V_{s_e})}{\sqrt{(P_e - P_{s_e}) \cdot (P_e - P_{s_e})^{\mathbf{T}}}} + c\dot{dt} \tag{3.13}$$

The measurement vector contains the difference between the GPS measurements and the INS based predictions which are called the measurement innovations, δz.

$$z = \begin{bmatrix} \delta z_{\rho_1} \\ \vdots \\ \delta z_{\dot{\rho}_1} \\ \vdots \end{bmatrix} = \begin{bmatrix} \rho_1 - \hat{\rho}_1 \\ \vdots \\ \dot{\rho}_1 - \hat{\dot{\rho}}_1 \\ \vdots \end{bmatrix} \tag{3.14}$$

The dimensions of the measurement vector are $4m \times 1$ with m equal to the number of visible satellites (assuming GPS measurements on L1 and L2 frequencies). Note that the measured pseudorange rate, $\dot{\rho}$ is calculated from the GPS Doppler measurement, f_d, by

$$\dot{\rho} = -\frac{c}{\lambda} f_d \tag{3.15}$$

where c is the speed of light and λ is the wavelength of the carrier signal.

Since the measurement model is a nonlinear function of the states, as seen in the Equations (3.12) and (3.13), the measurement matrix, H, is a linearization of the actual measurement model about the current states. It is derived by computing the partial derivative of each equation with respect to the state vector. Despite the fact that the position and velocity estimates from the INS navigation processor are dependent on the attitude errors, those influences are assumed to be small relative to the influence of the position and velocity errors. Therefore, attitude error affects on the pseudorange and pseudorange rate errors are ignored. Also, the velocity error is assumed to be the dominant error in the predicted pseudorange rate thus the partial derivative of Equation (3.13) with respect to the position error is assumed to be zero. With these assumption in mind, the measurement matrix is

approximated as

$$H = \begin{bmatrix} u^1 & 0 & 0 & 0 & 0 & 1 & 0 \\ \vdots & 0 & 0 & 0 & 0 & \vdots & 0 \\ 0 & u^1 & 0 & 0 & 0 & 0 & 1 \\ 0 & \vdots & 0 & 0 & 0 & 0 & \vdots \end{bmatrix} \tag{3.16}$$

where u^i is the unit vector from the GPS receiver to the i^{th} satellite and the column of ones corresponding to the receiver clock bias for the first $2m$ rows and the receiver clock drift for the last $2m$ rows.

The Kalman measurement update is performed by first calculating the Kalman gain using the linearized measurement matrix, the a priori error covariance matrix, and the measurement noise covariance matrix.

$$K_k = P_k H_k^{\mathbf{T}} (H_k P_k H_k^{\mathbf{T}} + R_k)^{-1} \tag{3.17}$$

The error covariance matrix and the error state vector are then updated with Equations (3.18) and (3.19).

$$P_k^+ = (I - K_k H_k) P_k^- \tag{3.18}$$

$$\hat{x}_k^+ = \hat{x}_k^- + K_k z_k \tag{3.19}$$

The measurement noise covariance matrix, R, is defined in Section 3.2.3.

The estimated position, velocity, attitude from the navigation processor are corrected using the error state vector. The position and velocity are update by simply adding the corresponding error state to the previous estimate. The rotation matrix, C_b^e, is updated using Equation (3.20) where $\Omega_{\delta\Psi}$ is the skew symmetric form of the attitude error estimate.

$$C_b^{e+} = (I_3 + \Omega_{\delta\Psi}) C_b^e \tag{3.20}$$

After the pose estimates are updated, the error states are reset to zero.

3.2.2.2 Propagation Model

The Kalman filter requires a linear system model to propagate the states and error covariance matrix in time. This is done by first defining the time derivative of the error state vector as a linear function of the states. Starting with the Equation (3.21), the time rate of change of the position errors is equal to the velocity errors.

$$\delta \dot{P}_e = \delta V_e \tag{3.21}$$

Propagation of the velocity estimates in the navigation processor is a function of the local acceleration due to gravity, the Coriolis effect, and the accelerometer measurements. The velocity error is dependent on each of these parameters as seen in Equation (3.22).

$$\delta \dot{V}_e = G_o \delta P_e - 2\Omega_{ie} \delta V_e - f_e \delta \Psi_e + C_b^e b_a \tag{3.22}$$

Errors associated with the local acceleration due to gravity are introduced through the position errors shown in the first term of the equation. G_o is a matrix of gravity variations defined for position vectors in the ECEF frame and its definition can be found in [35]. The estimated Coriolis effect is influenced by the velocity errors and the resulting deviations are accounted for in the second term. The final two terms are the affect of attitude errors on the rotation of the accelerometer measurements into the navigation frame and the affect of the accelerometer biases.

The time rate of change of the attitude errors is given in Equation (3.23).

$$\delta \dot{\Psi}_e = -\Omega_{ie} \delta \Psi_e + C_b^e b_g \tag{3.23}$$

Here, the attitude errors due to gyroscope biases are tracked along with any error introduced when removing the Earth's rotation from the gyroscope measurements.

In addition to the propagation models of the error states, models must be defined for the accelerometer and gyroscope biases. The accelerometer and gyroscope biases are modeled as Gauss Markov processes defined in Equation (3.24) and Equation (3.25) respectively.

$$\dot{b}_a = -\frac{1}{\tau_a} b_a + v_a \tag{3.24}$$

$$\dot{b}_g = -\frac{1}{\tau_g} b_g + v_g \tag{3.25}$$

In this work, the time constants are as follows: $\tau_a = 500s$ and $\tau_g = 1300s$. These values are taken from experimental identification of time constants for similar hardware in [36]. The noise terms are assumed to be zero mean white Gaussian noise.

With the system dynamics defined the system model, F, is constructed as seen in Equation 3.26.

$$F = \begin{bmatrix} 0_3 & I_3 & 0_3 & 0_3 & 0_3 & 0 & 0 \\ G_o & -2\Omega_{ie} & -f_e & C_b^e & 0_3 & 0 & 0 \\ 0_3 & 0_3 & -\Omega_{ie} & 0_3 & C_b^e & 0 & 0 \\ 0_3 & 0_3 & 0_3 & -\frac{1}{\tau_a} I_3 & 0 & 0 & 0 \\ 0_3 & 0_3 & 0_3 & 0_3 & -\frac{1}{\tau_g} I_3 & 0 & 0 \\ 0 & 0 & 0 & 0 & 0 & 0 & 1 \\ 0 & 0 & 0 & 0 & 0 & 0 & 0 \end{bmatrix} \tag{3.26}$$

Note that the final two rows correspond to the GPS receiver clock bias and drift with the derivative of the clock bias equal to the clock drift and the clock drift assumed to be driven by zero mean white noise. The discrete state transition matrix, Φ, is approximated by truncating the Taylor series expansion of $e^{F\Delta t}$ to first order resulting in

$$\Phi = I + F\Delta t \tag{3.27}$$

The first order approximation should be only used for propagation over sufficiently small intervals ($\Delta t < 1s$) [17]. The state transition matrix is used to propagate both the state vector and the error covariance matrix. The process noise covariance matrix, Q, is defined in the next section.

$$\hat{x}_{k+1}^{-} = \hat{x}_{k}^{+} + \Phi_k \hat{x}_{k}^{+} \tag{3.28}$$

$$P_{k+1}^{-} = \Phi_k P_{k}^{+} \Phi_{k}^{\mathbf{T}} + Q \tag{3.29}$$

3.2.3 GPS/INS Filter Initialization and Implementation

Filter initialization includes estimating the initial position, velocity, and attitude to "kick off" the INS navigation processor, and initialize the Kalman filter state vector and error covariance matrix. The position and velocity estimates are initialization with the first available GPS solutions but the initial attitude is not so easily estimated. High quality IMUs are capable of estimating the orientation of a static platform by observing the Earth's rotation and the local acceleration due to gravity. In this work, automotive grade IMU are the primary sensors used making this method infeasible. Alternatively, the attitude estimates are initialized based on the local East, North, UP (ENU) frame. The pitch and roll of the platform body frame relative to the local tangent plane are assumed to be zero. The yaw angle relating the forward axis of the body frame and the north direction is estimated using known landmarks. The rotation matrix relating the platform body frame to the local ENU frame is then computed using

$$C_b^l = \begin{bmatrix} \cos\theta_3 & -\sin\theta_3 & 0 \\ \sin\theta_3 & \cos\theta_3 & 0 \\ 0 & 0 & 0 \end{bmatrix} \begin{bmatrix} \cos\theta_2 & -\sin\theta_2 & 0 \\ \sin\theta_2 & \cos\theta_2 & 0 \\ 0 & 0 & 0 \end{bmatrix} \begin{bmatrix} 0 & 0 & 0 \\ 0 & \cos\theta_1 & \sin\theta_1 \\ 0 & -\sin\theta_1 & \cos\theta_1 \end{bmatrix} \tag{3.30}$$

where θ_1, θ_2, and θ_3 are 180^o, -90^o, and the yaw angle respectively. Note that this assumes that the platform body frame is defined as x forward, y right, and z down. Now the rotation matrix relating the local ENU frame to the ECEF frame, C_l^e is defined as seen in [12] and [35] using the estimated Latitude and Longitude. Finally, the initial body frame to ECEF frame transformation matrix is calculated using Equation (3.31).

$$C_b^e = C_l^e C_b^l \tag{3.31}$$

The Kalman filter state vector and error covariance matrix are initialized more intuitively. Since the state vector is comprised of error estimates it can be initialized to zeros. The error covariance matrix is initialized with the expected variance of the associated error states.

The GPS measurement noise covariance matrix, R, is again calculated as a function of the receiver characteristics and the carrier to noise ratio of each measurement. The pseudorange variance, σ_ρ^2, due to atmospheric delays and the receiver delay lock loops (DLL) was defined in Equation (2.21). The pseudorange rate measurement is tracked by the receiver frequency lock loops (FLL) causing the variance to be dictated by Equation (3.32) and (3.33).

$$\sigma_{\dot{\rho}}^2 = \sigma_{FLL}^2 + \frac{f_E^2}{9} \tag{3.32}$$

$$\sigma_{FLL} = \frac{\lambda}{2\pi T}\sqrt{\frac{4B_{np}}{c/n_0}(1 + \frac{1}{Tc/n_0})} \tag{3.33}$$

The parameters in the above equations are defined previously in Table 2.1 with the exception of f_E, the dynamic stress error. Assuming that the pseudorange variance and the pseudorange rate variance are uncorrelated the noise covariance matrix is a diagonal matrix is given by

$$R = \begin{bmatrix} \sigma_\rho^2 & 0 \\ 0 & \sigma_{\dot{\rho}}^2 \end{bmatrix} \tag{3.34}$$

The process noise covariance matrix, Q, is a diagonal matrix with approximations of the noise variance induced through the navigation processor and the variance of white noise of the GPS receiver clock bias and drift. Initial estimates of the noise variances are taken from [6] and are tuned to improve performance.

The observability of the GPS/INS filter is an important point to consider. There are no direct measurements of the platform's attitude available from the GPS receiver. Therefore, it can be difficult to differentiate attitude errors from accelerometer biases. For example, the roll angle error and the lateral accelerometer bias introduce common deviations in the filter solution. Accordingly, the platform must experience sufficient excitation to effectively distinguish accelerometer biases from attitude errors. Since the accelerometer biases are expected to change slowly with time, they are more easily separated from the attitude errors during high dynamic maneuvers. Generally once the platform has performed dynamic maneuvers, the bias estimates converge to the actual values and the transience in the estimation error decreases.

3.3 DRTK/INS

Combining GPS and INS for estimation of the relative position vector between two vehicles is similar to the standard GPS/INS integration described above. However, there is an addition choice of filter architectures. The RPV can be estimated in two stage federated filter approach where two independent GPS/INS filters feed a third filter responsible for only an RPV estimate or a single filter can be implemented combining measurements from each platform and computing both global position estimates and relative position estimates. The two implementation options are described below.

3.3.1 Federated Filter

A block diagram of the federated DRTK/INS filter approach is shown in Figure 3.5. Two independent GPS/INS filters maintain global position estimates for each vehicle. These

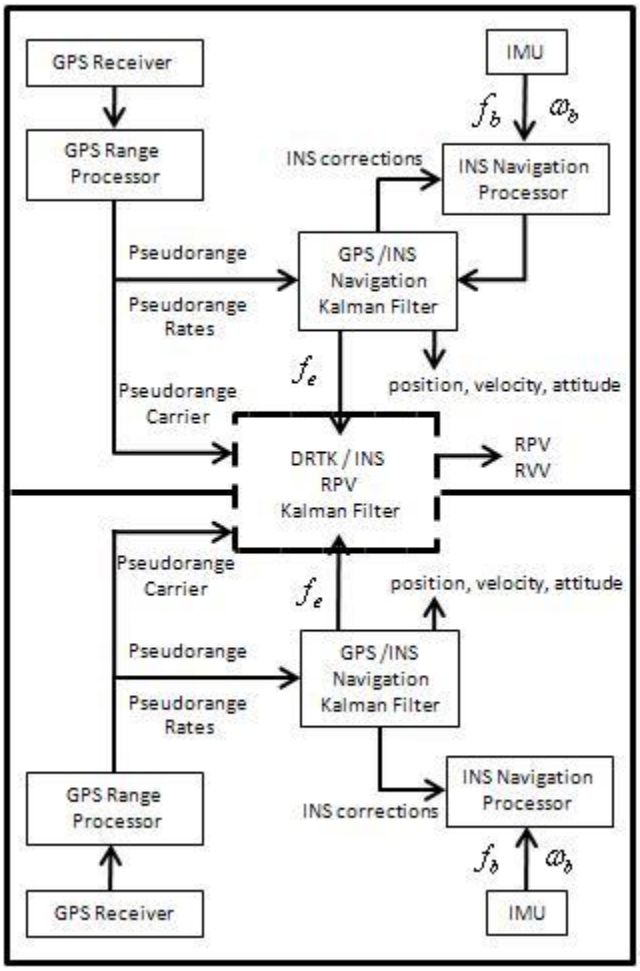

Figure 3.5: Federated DRTK/INS filter configuration

filter are executed exactly as described in Section 3.2.3. On each IMU measurement epoch, the specific force measurements are rotated in the navigation frame in the GPS/INS filter during the propagation step and the rotated measurements, f_e, are sent to the DRTK/INS filter for RPV propagation. The GPS pseudorange and carrier phase measurements from each receiver are used to update the RPV and a relative velocity vector (RVV). The RPV and RVV are estimated in a Kalman filter combining the filtering techniques described thus far.

3.3.1.1 Measurement Model

The DRTK/INS measurement update is similar to the measurement update discussed in Chapter 2 with minor exceptions. First of all, the low precision RPV estimate is maintained in the state vector rather than being estimated in a separate least squares routine. The state vector also contains the RVV and the double differenced carrier phase ambiguity estimates. The complete vector is given in Equation (3.35) with the total number of states being $6 + 2(m-1)$ where m is the number visible satellites.

$$x = \begin{bmatrix} \vec{r}_{ab} & \vec{v}_{ab} & \nabla\Delta N_{ab_{L1}}^{1\cdots m-1} & \nabla\Delta N_{ab_{L2}}^{1\cdots m-1} \end{bmatrix}^{\mathbf{T}} \tag{3.35}$$

Since the double differenced ambiguities are being estimated and the RPV is estimated in the state vector, the measurement vector is constructed with no need of the left null of the geometry matrix. The measurement vector simply contains the double differenced pseudorange and carrier phase measurements.

$$z = \begin{bmatrix} \nabla\Delta\rho_{ab_{L1}}^{1\cdots m-1} & \nabla\Delta\rho_{ab_{L2}}^{1\cdots m-1} & \nabla\Delta\phi_{ab_{L1}}^{1\cdots m-1} & \nabla\Delta\phi_{ab_{L2}}^{1\cdots m-1} \end{bmatrix}^{\mathbf{T}} \tag{3.36}$$

The measurement matrix is now dependent on the satellite geometry. The unit vector to the base satellite is subtracted from the remaining unit vectors to account for the double difference. Rows corresponding to carrier phase measurements contain the signal wavelength in the appropriate column to add the carrier ambiguity estimate to the estimated range. The measurement matrix is shown in Equation (3.37) with the satellite notation removed but note that the total number of rows in H will be $4(m-1)$.

$$H = \begin{bmatrix} \Delta u_{a_{L1}} & 0_3 & 0_3 & 0_3 \\ \Delta u_{a_{L2}} & 0_3 & 0_3 & 0_3 \\ \Delta u_{a_{L1}} & 0_3 & \lambda_{L1} & 0_3 \\ \Delta u_{a_{L1}} & 0_3 & 0_3 & \lambda_{L2} \end{bmatrix} \tag{3.37}$$

The Kalman measurement update is carried out with Equations (2.15) through (2.17). The RPV estimated in the state vector is comparable to the low precision estimate of the RPV described in the Chapter 2. To compute a high precision estimate, the estimated carrier ambiguities must be fixed to integer values. Again, the LAMBDA method is used to construct candidate integer sets and the ratio test is performed to evaluate the validity of the fix. If the ratio test is passed the high precision RPV is estimated with Equation (2.32).

3.3.1.2 Propagation Model

As seen in Equation (3.35), the platform attitudes are not estimated the DRTK filter. Since the rotated accelerometer measurements are available from the independent GPS/INS filters, they can be used directly in the relative navigation filter. The rotated specific force measurements enter the DRTK filter through the input matrix given by

$$\Gamma = \begin{bmatrix} \frac{1}{2}\Delta t^2 I_3 \\ \Delta t I_3 \\ 0_{(2(m-1)\times 3)} \end{bmatrix} \tag{3.38}$$

The state transition matrix is constructed accounting for the kinematic relationship of the RVV and RPV and assuming the ambiguity estimates are constant.

$$\Phi = \begin{bmatrix} I_3 & \Delta t I_3 & 0_{(3\times 2(m-1))} \\ 0_3 & I_3 & 0_{(3\times 2(m-1))} \\ 0_{2(m-1)} & 0_{2(m-1)} & I_{2(m-1)} \end{bmatrix} \tag{3.39}$$

With the specific force measurements from the two platforms rotated into a common navigation frame, they can be subtracted from one another to compute the relative specific force. Also notice that since the platforms are assumed to be in close proximity (a requirement of DRTK) and the measurements are expressed in the same frame the effects of gravity experienced by each unit are approximately equal and are therefore removed when

the measurements are subtracted. Finally, if it is assumed that the relative Coriolis effects are small compared to the sensor noise, the relative acceleration of the two platforms can be approximated by Equation (3.40).

$$f_{e_{ab}} = f_{e_b} - f_{e_a} \tag{3.40}$$

Now the input to the system is given by, $f_{e_{ab}}$, and the state vector and error covariance matrix are propagated with the following equations:

$$\hat{x}_k = \Phi_k \hat{x}_{k-1} + \Gamma_k f_{e_{ab_k}} \tag{3.41}$$

$$P_k = \Phi_k P_{k-1} \Phi_k^{\mathbf{T}} + Q \tag{3.42}$$

3.3.1.3 Implementation

The carrier phase ambiguities in the state vector are initialized with the first available GPS pseudorange and carrier measurements as described in Section 2.2.1.3. RPV and RVV estimates are initialized by differencing the GPS position and velocity solutions from the two receivers. The error covariance matrix is initialization with the expected variances of the RPV, RVV, and double differenced ambiguity estimates.

In the event that GPS becomes unavailable after initialization, the RPV estimates are maintained by dead-reckoning with inertial measurements. This leads to an alternative method of re-initialization of the carrier ambiguity estimates after short GPS outages. The RPV estimate can be used to re-initialize the ambiguity estimates using Equation (3.43).

$$\nabla \Delta N_\lambda = (\nabla \Delta \phi - \Delta \vec{u}_a \vec{r}_{ab})/\lambda \tag{3.43}$$

In the discussion of the propagation of the RPV and the RVV, the accelerometer bias was not mentioned explicitly, but there are two possible methods of accounting for them. One option is to remove the bias prior to sending the specific force measurement to the

DRTK algorithm but subtracting the GPS/INS estimate of the bias from the measurement. The other option is to estimate the relative bias in the DRTK filter by augmenting the state vector to include bias estimates. Each alternative offered similar results in testing. The results presented in this chapter are computed by removing the bias prior to passing the IMU measurements to the DRTK algorithm.

The measurement noise covariance matrix, R, is calculated as described in Section 2.2.1.3. However, the variance must be representative of the variance of double differenced pseudorange and carrier measurements. The variance of the single differenced measurements from receivers a and b is given by

$$R_s = \begin{bmatrix} \sigma^2_{a_{DLL}} + \sigma^2_{b_{DLL}} & 0 \\ 0 & \sigma^2_{a_{PLL}} + \sigma^2_{b_{PLL}} \end{bmatrix} \tag{3.44}$$

This matrix is transformed into the matrix of double differenced measurement variances using the transformation matrix, C^d_s, detailed in Section 2.2.2.

$$R = \begin{bmatrix} C^d_s & 0 \\ 0 & C^d_s \end{bmatrix} R_s \begin{bmatrix} C^d_s & 0 \\ 0 & C^d_s \end{bmatrix}^{\mathbf{T}} \tag{3.45}$$

3.3.2 Centralized Filter

The alternative to the federated filter approach is one filter estimating global and relative position states. Figure 3.6 shows a block diagram of the centralized DRTK/INS filter configuration. The filter inputs are the raw measurements from each GPS receiver and the INS navigation processor outputs from each platform. The global position, velocity, and attitude of each platform is estimated along with the RPV between the receivers.

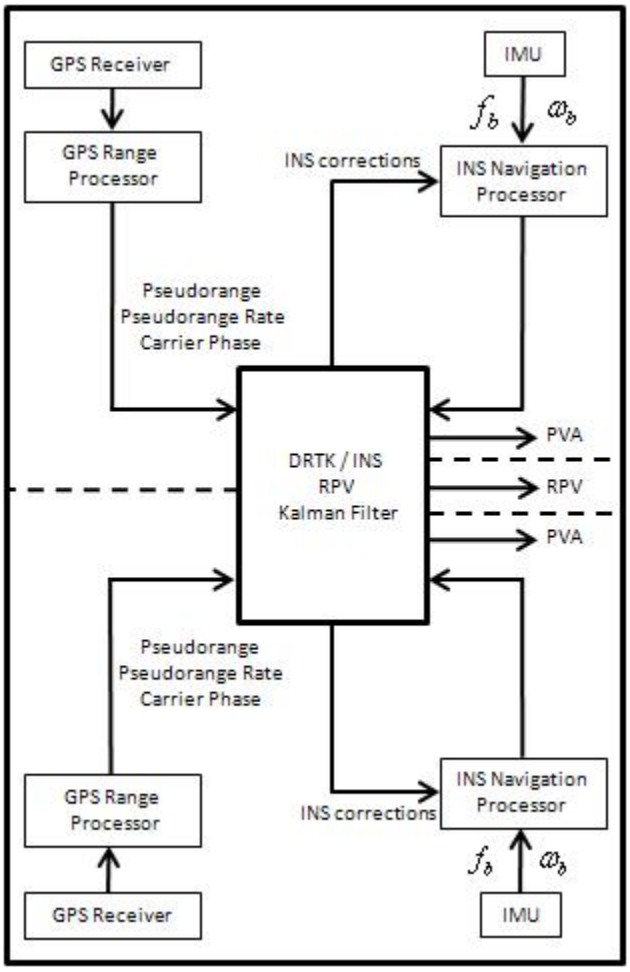

Figure 3.6: Centralized DRTK/INS filter configuration

3.3.2.1 Measurement Model

The centralized DRTK/INS filter can be thought of as a combination of the GPS/INS filter described in Section 3.2 and the DRTK algorithm described in Chapter 2. The Kalman filter is implemented with a combination of error states and actual states. The position, velocity, and attitude errors of each platform occupying the first 18 rows of the states vector. Three dimensional accelerometer and gyroscope bias estimates make up the next 12 states followed by the receiver clock bias and drift estimates. Next is the RPV error and the double differenced carrier ambiguities. The complete vector is given in Equation (3.46).

$$x = \begin{bmatrix} \delta P_{e_a} & \delta V_{e_a} & \delta \Psi_{e_a} & \delta P_{e_b} & \delta V_{e_b} & \delta \Psi_{e_b} & b_a & b_g & cdt_a & \dot{cdt_a} & cdt_b & \dot{cdt_b} & \delta r_{ab} & \nabla\Delta N_{ab} \end{bmatrix}^{\mathbf{T}} \tag{3.46}$$

While implementing a filter of this size in real time may be troublesome, it is shown here to investigate any performance improvements gained by coupling global position estimation with relative position estimation.

As in the GPS/INS filter, predictions of the pseudorange and pseudorange rate measurements are computed using Equation (3.12) and (3.13). The double differenced carrier phase measurements are also predicted from the estimated relative position vector and the carrier ambiguity estimates.

$$\nabla\Delta\hat{\phi}_{ab} = \Delta\vec{u}_a\vec{r}_{ab} + \nabla\Delta N_{ab} \tag{3.47}$$

The measurement vector is constructed by subtracting the predictions from the GPS measurements resulting in the measurement innovations.

$$z = \begin{bmatrix} \delta\rho_a \\ \delta\dot{\rho}_a \\ \delta\rho_b \\ \delta\dot{\rho}_b \\ \delta\phi_{ab} \end{bmatrix} = \begin{bmatrix} \rho_a - \hat{\rho}_a \\ \dot{\rho}_a - \hat{\dot{\rho}}_a \\ \rho_b - \hat{\rho}_b \\ \dot{\rho}_b - \hat{\dot{\rho}}_b \\ \nabla\Delta\phi^1_{ab} - \nabla\Delta\hat{\phi}^1_{ab} \end{bmatrix} \tag{3.48}$$

Again, the predicted pseudorange and pseudorange rates are nonlinear combinations of the position and velocity estimates. Therefore, the measurement matrix is developed by linearizing the measurement equations about the current position and velocity. The carrier phase prediction is a linear function of the RPV and the ambiguity estimates so the measurement equation can be put directly into the measurement matrix.

$$H = \begin{bmatrix} \vec{u}_a & 0 & 0 & 0 & 0 & 0 & 0 & 0 & 1 & 0 & 0 & 0 & 0 & 0 \\ 0 & \vec{u}_a & 0 & 0 & 0 & 0 & 0 & 0 & 0 & 1 & 0 & 0 & 0 & 0 \\ 0 & 0 & 0 & \vec{u}_b & 0 & 0 & 0 & 0 & 0 & 0 & 1 & 0 & 0 & 0 \\ 0 & 0 & 0 & 0 & \vec{u}_b & 0 & 0 & 0 & 0 & 0 & 0 & 1 & 0 & 0 \\ 0 & 0 & 0 & 0 & 0 & 0 & 0 & 0 & 0 & 0 & 0 & 0 & \Delta\vec{u}_a & \lambda \end{bmatrix} \tag{3.49}$$

The Kalman filter measurement update is performed using Equations (3.50) through (3.52).

$$K_k = P_k H_k^{\mathbf{T}} (H_k P_k H_k^{\mathbf{T}} + R_k)^{-1} \tag{3.50}$$

$$P_k^+ = (I - K_k H_k) P_k^- \tag{3.51}$$

$$\hat{x}_k^+ = \hat{x}_k^- + K_k z_k \tag{3.52}$$

An attempt is then made to fix the floating point ambiguity estimates to integer values using the LAMBDA method. With an acceptable integer set, the high precision RPV is

estimated using least squares as seen in Equation (2.32). Since the errors in the position, velocity, attitude, and RPV are being estimated in the Kalman filter, the estimates of the actual states must be updated after a measurement update. The position, velocity, and RPV estimates are updated by adding the estimated errors to the previous estimate while the attitude estimates are updated as seen in the GPS/INS filter using Equation (3.20).

3.3.2.2 Propagation Model

The propagation step of the centralized DRTK/INS filter involves propagation of the pose estimates and the RPV as well as propagation of the error states in the Kalman filter time update. Propagation of the position, velocity, and attitude estimates follows the procedure laid out in Section 3.2.1. The estimates of the pose of each platform are updated using Equations (3.53) through (3.55).

$$P_{e_k} = P_{e_{k-1}} + V_{e_k}\Delta t \tag{3.53}$$

$$V_{e_k} = V_{e_{k-1}} + (f_e + g_e - 2\Omega_{ie}V_{e_{k-1}})\Delta t \tag{3.54}$$

$$C^e_{b_k} = C^e_{b_{k-1}}(I + \Omega_{ib}\Delta t) - \Omega_{ie}C^e_{b_{k-1}}\Delta t \tag{3.55}$$

Propagation of the RPV can be performed by either doubly integrating the relative specific force of the two platforms expressed in the navigation frame or by integrating the relative velocity of the two platforms. Here, the relative velocities are chosen and the RPV is propagated by

$$\vec{r}_{ab_k} = \vec{r}_{ab_{k-1}} + (V_{e_{b_k}} - V_{e_{a_k}})\Delta t \tag{3.56}$$

The system matrix is constructed in the same manner as the system matrix of the GPS/INS filter. The accelerometer and gyroscope biases are modeled as Gauss Markov processes and the ambiguity states are modeled as constants. The RPV error state dynamics are given by

$$\delta\dot{\vec{r}}_{ab} = \delta V_{e_b} - \delta V_{e_a} \tag{3.57}$$

and the system matrix is shown in Equation (3.58).

$$F = \begin{bmatrix}
0 & I_3 & 0 & 0 & 0 & 0 & 0 & 0 & 0 & 0 & 0 & 0 & 0 & 0 \\
G_o & -2\Omega_{ie} & -f_e & 0 & 0 & 0 & C_b^e & 0 & 0 & 0 & 0 & 0 & 0 & 0 \\
0_3 & 0_3 & -\Omega_{ie} & 0 & 0 & 0 & 0 & C_b^e & 0 & 0 & 0 & 0 & 0 & 0 \\
0 & 0 & 0 & 0 & I_3 & 0 & 0 & 0 & 0 & 0 & 0 & 0 & 0 & 0 \\
0 & 0 & 0 & G_o & -2\Omega_{ie} & -f_e & C_b^e & 0 & 0 & 0 & 0 & 0 & 0 & 0 \\
0 & 0 & 0 & 0 & 0 & -\Omega_{ie} & 0_3 & C_b^e & 0 & 0 & 0 & 0 & 0 & 0 \\
0 & 0 & 0 & 0 & 0 & 0 & -\frac{1}{\tau_a} I_3 & 0 & 0 & 0 & 0 & 0 & 0 & 0 \\
0 & 0 & 0 & 0 & 0 & 0 & 0 & -\frac{1}{\tau_g} I_3 & 0 & 0 & 0 & 0 & 0 & 0 \\
0 & 0 & 0 & 0 & 0 & 0 & 0 & 0 & 0 & 1 & 0 & 0 & 0 & 0 \\
0 & 0 & 0 & 0 & 0 & 0 & 0 & 0 & 0 & 0 & 0 & 0 & 0 & 0 \\
0 & 0 & 0 & 0 & 0 & 0 & 0 & 0 & 0 & 0 & 0 & 1 & 0 & 0 \\
0 & 0 & 0 & 0 & 0 & 0 & 0 & 0 & 0 & 0 & 0 & 0 & 0 & 0 \\
0 & I_3 & 0 & 0 & I_3 & 0 & 0 & 0 & 0 & 0 & 0 & 0 & 0 & 0 \\
0 & 0 & 0 & 0 & 0 & 0 & 0 & 0 & 0 & 0 & 0 & 0 & 0 & 0
\end{bmatrix} \tag{3.58}$$

The state transition matrix is approximated by Equation 3.27 and the state vector and error covariance matrix are propagated using Equations 3.28 and 3.29.

3.3.2.3 Implementation

The centralized DRTK/INS filter is initialized with the first available GPS measurements as described in previous implementations. As with the federated filter approach the double difference ambiguity estimates can be initialized with either the double differenced pseudorange and carrier phase measurements or with the estimated RPV position vector. The error states used in the Kalman filter are initialized to zero.

GPS measurement variances are defined as a function of the carrier to noise ratio of the given signal in Equations (2.21), (3.32), and (2.24). These values are used once again

in the measurement noise covariance matrix. The measurement noise of the pseudorange, pseudorange rate, and carrier phase measurements are assumed to be uncorrelated but it should be noted that there is some correlation of the pseudorange rate and carrier phase noise that is ignored. The measurement noise covariance matrix is therefore represented by the matrix defined in Equation (3.59).

$$R = \begin{bmatrix} \sigma^2_{\rho_a} & 0 & 0 & 0 & 0 \\ 0 & \sigma^2_{\dot{\rho}_a} & 0 & 0 & 0 \\ 0 & 0 & \sigma^2_{\rho} & 0 & 0 \\ 0 & 0 & 0 & \sigma^2_{\dot{\rho}_a} & 0 \\ 0 & 0 & 0 & 0 & C^d_s(\sigma^2_{a_{PLL}} + \sigma^2_{b_{PLL}})C^d_s \end{bmatrix} \tag{3.59}$$

Note that the single difference carrier phase variance has been transform into the double difference variance.

Each of the DRTK/INS integrated filters described in this chapter may implemented with single or dual frequency GPS measurements. The federated and centralized filter configurations are initially compared based on performance in dual frequency operation to determine any discernible differences. The federated filter is selected for further study and its performance with only L1 measurements is examined. The federated filtering architecture is expanded in Appendix 5.2.3 to include fault detection and exclusion (FDE) capabilities. Additional results on the effectiveness of the FDE algorithm are also provided in the appendix.

3.4 Experimentation and Results

The federated and centralized DRTK/INS filters were tested in post-process using data collected at the National Center for Asphalt Technology (NCAT) at Auburn University. Data was collected on the test track and in the surrounding areas as seen in Figure 3.7. Two Infiniti G35 sedans were equipped with Novatel Propak V3 GPS receivers and automotive grade

Figure 3.7: NCAT test facility with data collection locations. Background map by *GPS Visualizer*

Crossbow 440 IMUs. GPS measurements were collected at 5 Hz and inertial measurements were collected at 20 Hz. A Septentrio Pola Rx2 GPS receiver was used as a base station to calculate a RTK position solution to be used as reference data.

The primary motivation for the developing both centralized and federated DRTK/INS filters was to determine if the coupling of the global and relative position estimates in the centralized filter would improve the accuracy of either estimate. In contrast to the coupled global and relative states of the centralized filter, there is no feedback from the DRTK filter to the independent GPS/INS filters in the federated architecture. For this reason the analysis begins with an evaluation of the global positions estimates of the individual vehicles. The estimated position of one of the test vehicles is shown in a local East, North, Up (ENU) frame in Figure 3.8. Note that the position of the vehicle is estimated in the ECEF frame and rotated into a local ENU frame using the initial position as the frame origin. The position solutions calculated with the centralized and federated filters are shown with the RTK reference solution. A portion of the figure is expanded in Figure 3.9 to reveal the three position solutions. A slight bias of the position solution from each filter can be seen in the figure. This can be attributed to unmodeled GPS errors such as atmospheric delays and signal multipath. Each estimate tracks the RTK solution well with little discernible difference in their accuracies. The East and North position errors are calculated at the 5 Hz

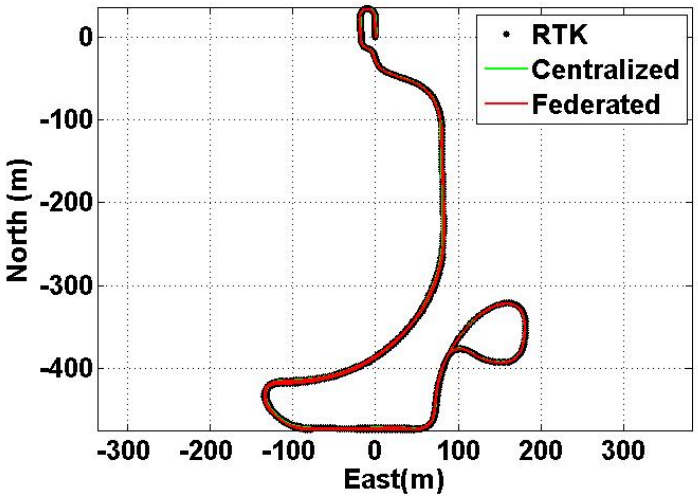

Figure 3.8: East and North global position solutions for one vehicle computed with centralized and federated filters shown with RTK reference solution

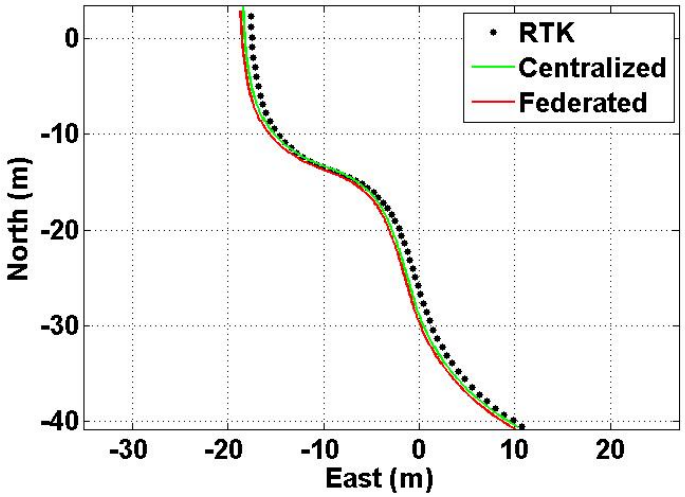

Figure 3.9: Zoom view of global position solutions shown with RTK reference solution

Table 3.1: Error Analysis of Position Estimates from Centralized and Federate Filters

	East		North	
	RMSE (m)	Variance (m^2)	RMSE (m)	Variance (m^2)
Centralized	1.17	0.40	0.63	0.25
Federated	1.32	0.44	0.67	0.40

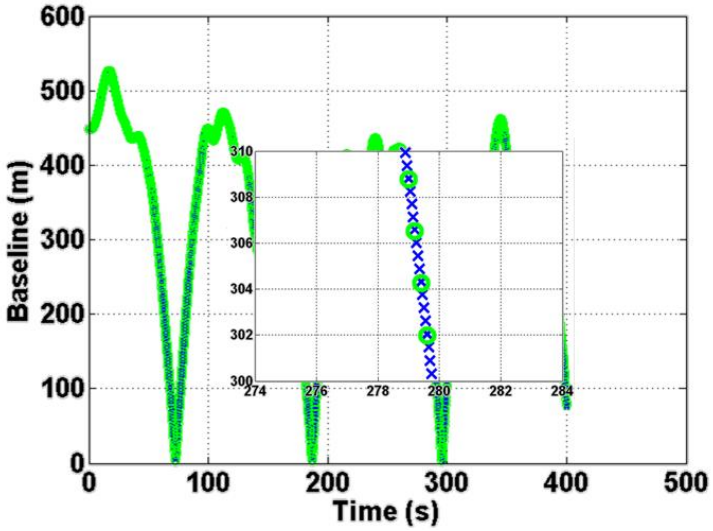

Figure 3.10: High and low precision baseline estimates as calculated by centralized DRTK/INS filter for separation distances up to 500 meters

update rate on the RTK solution and the results are shown in Table 3.1. The RMSE of the East and North position estimates is below one and one half meters for each filtering option. The analysis does not reveal a significant difference in the accuracy of the two filters when estimating the global position of one vehicle.

It is important to evaluate the accuracy of the relative position estimates. The low precision and high precision estimates of the baseline between the two vehicles are shown in Figure 3.10. The low precision solution is marked by blue Xs and the high precision solution is shown as green circles. This solution was calculated using the centralized architecture but it is typical of the results of each filtering method. A comparison of the results of the two filtering options is shown in Figure 3.11. The error in the relative position vector is shown for the centralized filter in green and the federated filter in red. The reference RPV was calculated by subtracting the RTK position solution of the two vehicles. From

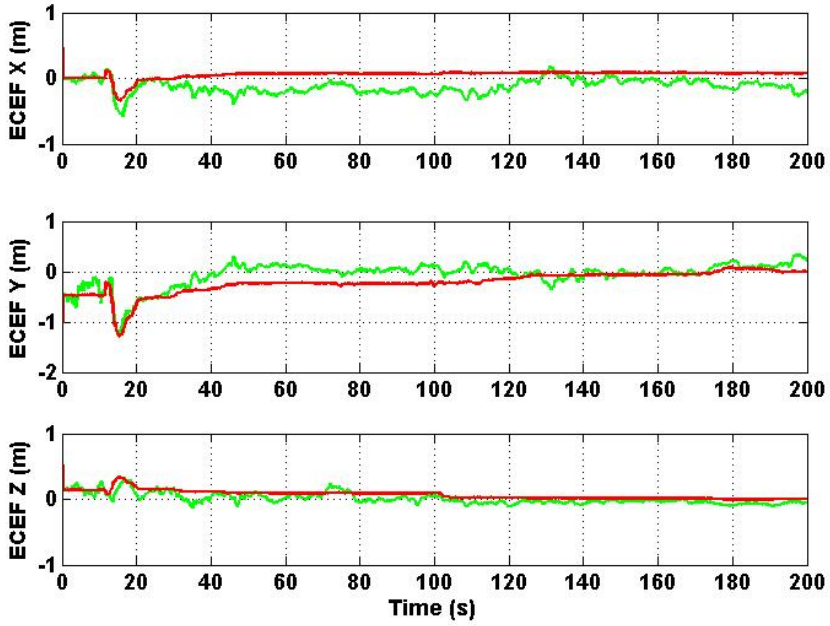

Figure 3.11: Low precision relative position vector errors in the ECEF frame of the centralized (green) and federated (red) RPV estimates as compared to RTK solution

Table 3.2: Statistics on HP and LP Baseline Errors

	High Precision		Low Precision	
	RMSE (cm)	Variance (cm^2)	RMSE (cm)	Variance (cm^2)
Centralized	0.13	0.03	12.03	44.0
Federated	0.06	0.03	13.57	17.0

the figure it is clear that the federated filter produces a smoother RPV estimate than the centralized filter. The low precision and high precision baseline errors are shown in Figure 3.12 and 3.13 respectively. In Table 3.2, the RMSE and variance of the low precision and high precision baseline errors are given. The results of each filter are comparable to the results seen in Chapter 2. Recall from Section 2.4 that the RMSE of the low precision baseline error was approximately 20 centimeters using only GPS measurements. The error is improved slightly by incorporating the IMU as the RMSE is approximately 13 centimeters for both the centralized and federated filter. Notice that the high precision error is consistent with the previous results showings sub-centimeter errors. This would be expected since the high precision solution is computed in the same manner as it was in Chapter 2.

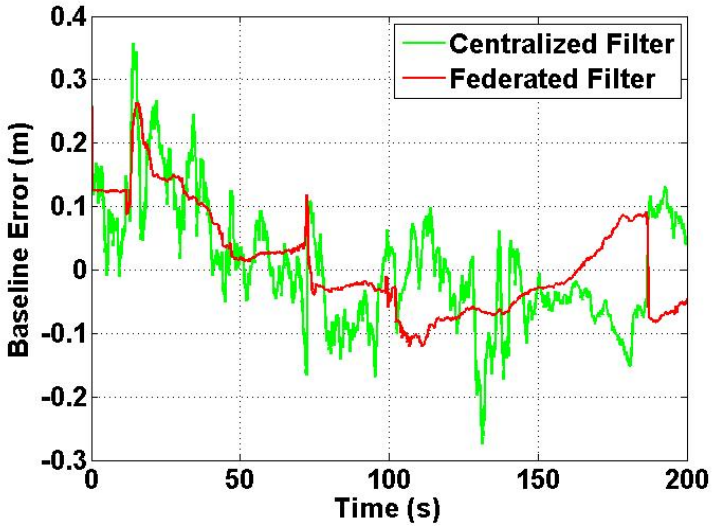

Figure 3.12: Low precision baseline error of centralized and federated DRTK/INS filters

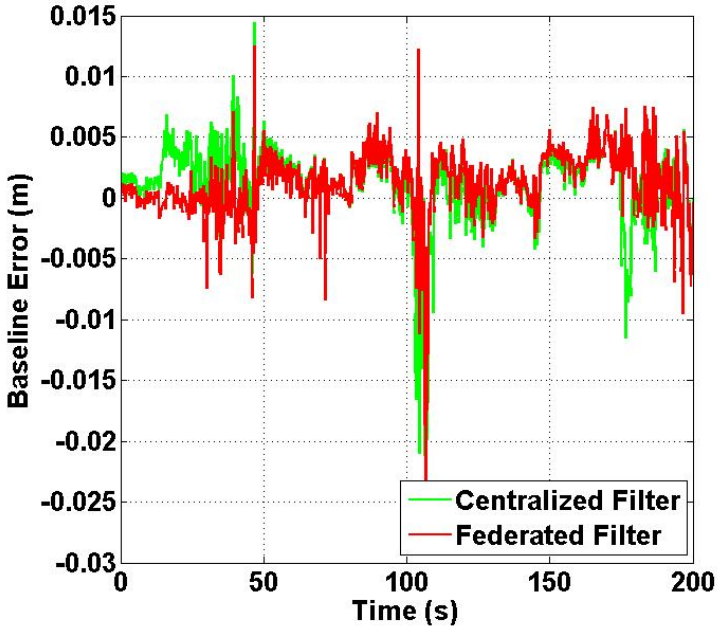

Figure 3.13: High precision baseline error of centralized and federated DRTK/INS filters

One final point of comparison of the centralized and federated filtering approaches was the reacquisition of fixed integer estimates of the carrier ambiguity after a GPS outage. As stated in Section 3.3.1.3, after a GPS outage the ambiguity estimates may be reinitialized using the propagated RPV estimate from the INS. To test the effectiveness of this initialization method, GPS outages were simulated during data processing. The ambiguity estimates were then reinitialized using Equation 3.43 and the time to reacquire fixed integer estimates was recorded. The results are shown in Figure 3.14 with the results of the DRTK algorithm described in Chapter 2 which does not use the INS for dead-reckoning. In the figure, the reacquisition time using the dead-reckoning solution increases significantly after as little as a one second outage. The increase in the reacquisition time is due to the drift of the INS RPV solution during the GPS outage. Accordingly, as the outage time increases, the INS solution degrades and the time to reacquisition increases. As would be expected, the original DRTK algorithm resulted in consistent fixing times regardless of the duration of the outage. The integer reacquisition times for the DRTK algorithm correspond well with the mean time to first fix reported in Chapter 2 of approximately 0.2 seconds. It is important to consider the quality of the IMU used in this test when evaluating these results. The unit used here was an automotive grade IMU which exhibits drift characteristics that can result in meter level errors in as little as one second [35]. Given a higher quality IMU, the results shown here could be significantly improved.

From these results, it is shown that both the centralized and federated DRTK/INS integration architectures provide low precision RPV estimates with sub-meter level errors. The two filtering options offer similar accuracies for both the global and relative position estimates. Furthermore, neither filter provides improvement in reacquisition of carrier ambiguities after a GPS outage. For these reasons and due to the complexity of the centralized filter architecture, the federated filter is selected as the preferred option. The federated filter was implemented and testing using only L1 measurements as a continuation of the single and dual frequency comparison from Chapter 2.

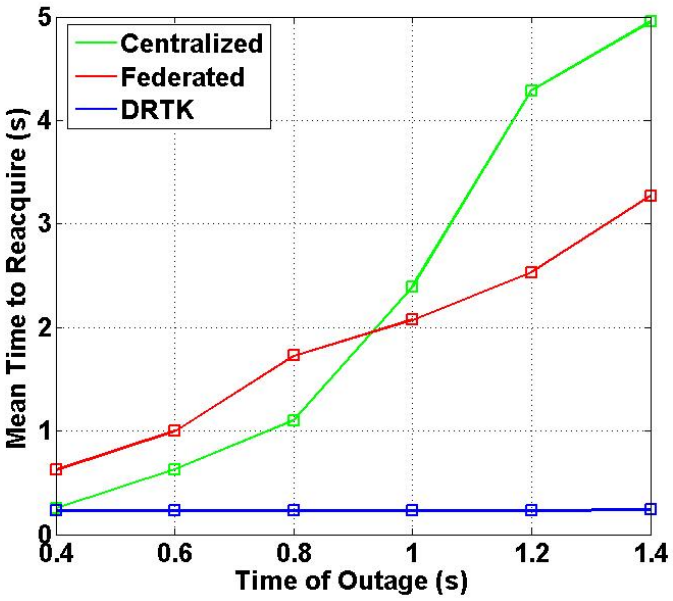

Figure 3.14: Integer reacquisition times after a GPS outage using different initialization procedures

Table 3.3: Statistics on HP and LP Baseline Errors of Single Frequency Federated Filter

	High Precision		Low Precision	
	RMSE (cm)	Variance (cm^2)	RMSE (cm)	Variance (cm^2)
Single Frequency	0.25	0.50	22.81	467

Evaluation of the single frequency algorithm focuses on the relative position estimation. Figure 3.12 shows the error in the low precision RPV estimates in the ECEF frame. The results shown here are comparable to those shown in Figure 3.11. The RMSE and variance of the baseline errors are provided in Table 3.3. Note that the low precision RMSE is nearly identical to the GPS only single frequency solution which was approximately 24 centimeters. Again, the RMSE of the high precision baseline error is consistent with the results shown in Chapter 2. The high precision baseline error is shown graphically in Figure 3.13.

Finally, the reacquisition of carrier phase ambiguities was investigated. As with the dual frequency algorithms, GPS outages ranging from two measurement epochs up to seven measurement epoch were simulated during data processing. The ambiguities estimates were reinitialized after the outage using the INS RPV solution. The results of the test are shown in

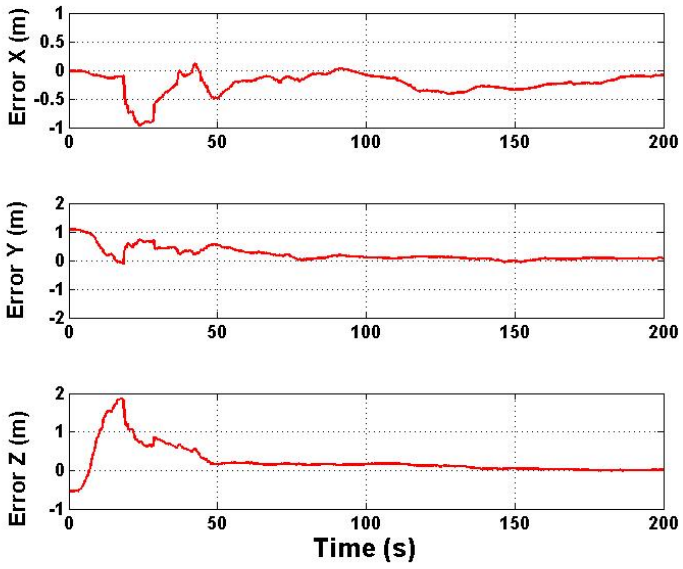

Figure 3.15: Low precision relative position vector errors in the ECEF frame of the single frequency federated RPV estimates as compared to RTK solution

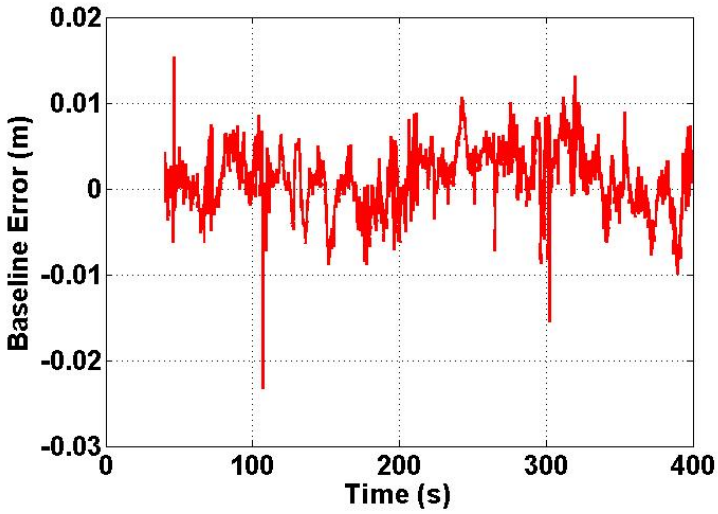

Figure 3.16: High precision baseline error of single frequency federated DRTK/INS filter

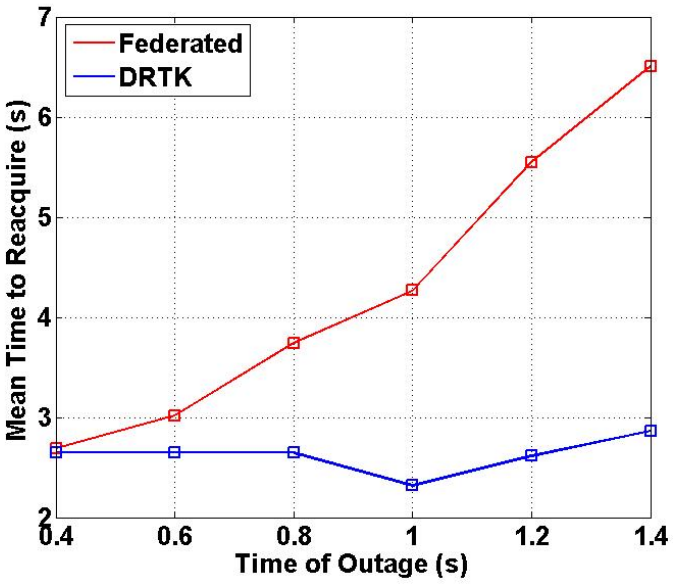

Figure 3.17: Integer reacquisition times after a GPS outage using single frequency measurements and different initialization procedures

Figure 3.17 with the results of the DRTK only algorithm using L1 frequency measurements. As expected, the DRTK algorithm results in consistent reacquisition times for various outage times. The integer reacquisition times for the DRTK algorithm were slightly shorter than the mean time to first fix reported in Chapter 2 of approximately 4.3 seconds. Again, the RPV based initialization method shows increasing reacquisition times as the duration of the outage increase.

3.5 Conclusions

Centralized and federated DRTK/INS integrated navigation systems were presented. The filter architectures were implemented and tested in post process using actual GPS and IMU data collect on two vehicles. The results indicate that each form is capable of providing estimates of the RPV between the two vehicles with sub-meter errors. Initialization of ambiguity estimates with INS propagated RPV estimates was also investigates. The automotive grade IMU used in this research did not provide the level of stability required to decrease the integer reacquisition time. The traditional ambiguity initialization method described in

the Section 2.2.1.3 provided more consistent results. The federated DRTK/INS filter was chosen as the preferred integration architecture due to the similarity in performance of the two methods and due to the complexity the centralized filter approach.

The federated DRTK/INS filter was also implemented and tested using only L1 frequency measurements. As in Chapter 2, the fixed ambiguity RPV accuracy of the DRTK/INS filter was comparable using either single or dual frequency measurements. As with the dual frequency algorithm, there was no improvement in the time to reacquire fixed integer ambiguity estimates using the dead reckoning RPV estimate.

Chapter 4

Performance Analysis of DRTK/TDCP Following

In this Chapter, an autonomous following method using differential GPS techniques is compared to an autonomous following method using standard GPS positioning. A description of each method is provided beginning with the following method using standard GPS positioning. Perhaps the most intuitive use of GPS positioning in the leader/follower application is the "breadcrumb" following method. In this approach, the following vehicle is notified of the lead vehicle's global position periodically. A database of the lead vehicle positions are stored as GPS coordinates or waypoints defining the lead vehicle's path. The following vehicle then selects a waypoint from the database to drive towards. The waypoint is selected based on some minimum following distance or look ahead distance. The selected waypoint is the point in the database closest to the following vehicle that exceeds the look ahead distance. Often the look ahead distance is variable and is scaled by the speed of the following vehicle. Additional constraints are used to ensure that the selected waypoint is in front of the following vehicle.

The breadcrumb following method requires accurate and smooth GPS global position estimates of both the lead vehicle and the following vehicle. However, standard GPS positioning errors are typically on the order of ten meters horizontally with a minimum of meter level errors under ideal conditions. An example of the horizontal position error of a standard GPS solutions is shown in Figure 4.1. The error is calculated between the standard position solution reported by the Novatel Propak V3 receiver and a RTK reference solution. The magnitude of horizontal position error calculated in a local ENU frame is plotted. The bottom graph is a zoomed portion of the top graph showing the horizontal error from the 150 second mark to the 200 second mark. As seen in the figure, there are several meter level

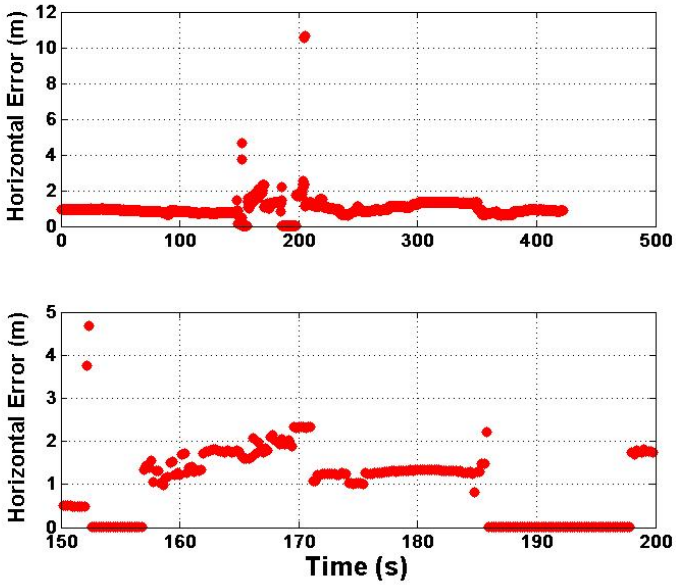

Figure 4.1: Horizontal position error for standard positioning solution as calculated by Novatel receiver compared to RTK reference

jumps in the position error in the 50 second time window and the maximum error is over 10 meters. Depending on the operational environment, using this solution for autonomous following could be dangerous. If the vehicles are operating in a road setting, a shift of only a couple of meters could lead to a head on collision as seen in Figure 4.2. In a military application, the autonomous vehicle could be following a land mine clearing vehicle through a mine field were accurate lateral positioning is vital. While the use of an RTK base station will improve the accuracy and consistency of the GPS position solution, base stations are not available in all operating environments. An alternative is to use the differential GPS methods discussed in Chapter 2 and 3 to provide highly accurate relative position estimates.

As shown in Chapter 2, the DRTK algorithm is capable of producing relative position vectors (RPV) between two platforms with sub-centimeter errors. This information can be used in an alternative following method in place of the global position estimates used in the breadcrumb following method. The RPV is used to calculate the a desired heading angle for the following vehicle which will point the following vehicle at the current position of

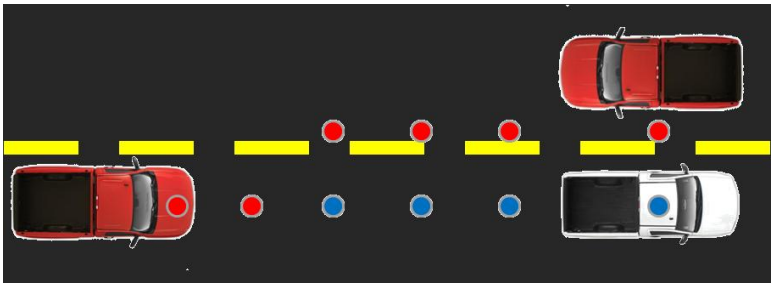

Figure 4.2: Shift in standard positioning solution (red dots) relative to the actual path of the lead vehicle (blue dots)

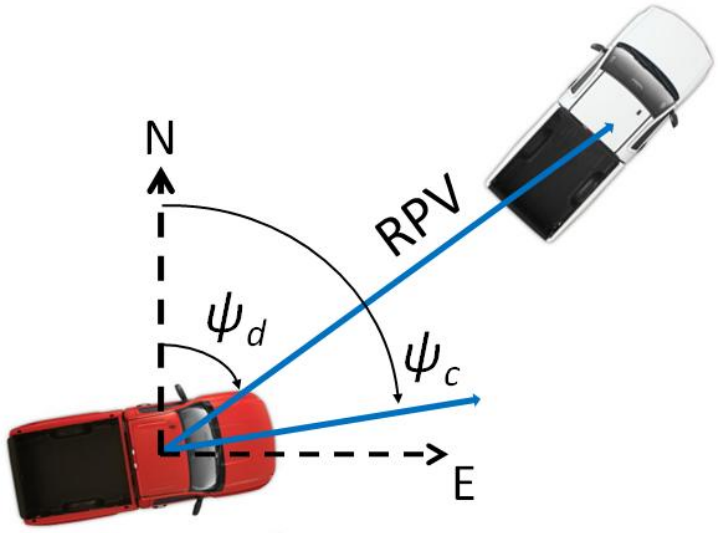

Figure 4.3: The desired heading angle of the following vehicle is calculated using the relative position vector expressed in the East, North, Up frame

the lead vehicle. The desire heading angle, ψ_d, the current heading angle of the following vehicle, ψ_c, and the RPV are shown for a leader/follower configuration in Figure 4.3. The desired heading angle is calculated using the East and North components of the RPV using Equation (4.1).

$$\psi_d = \arctan\left(\frac{RPV_E}{RPV_N}\right) \tag{4.1}$$

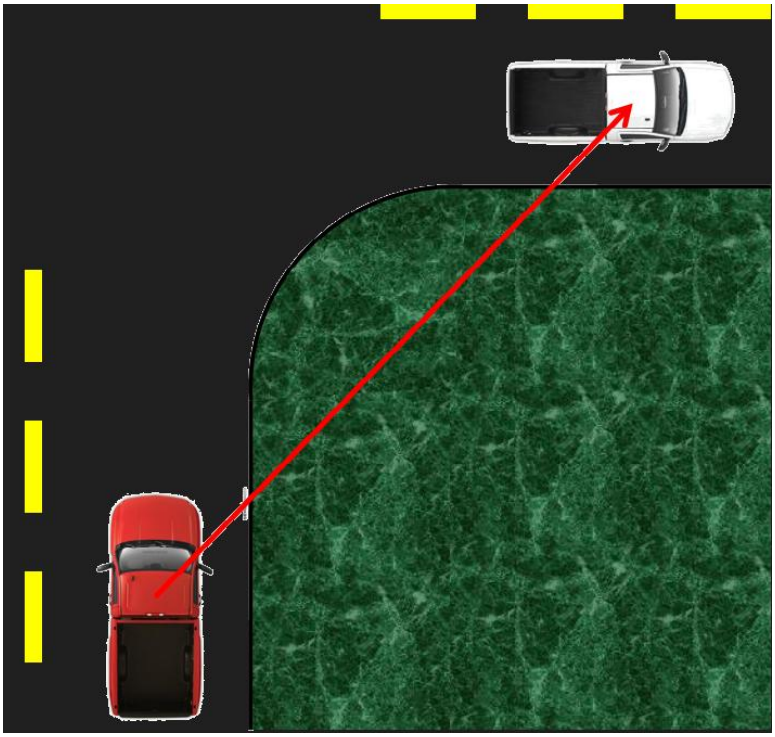

Figure 4.4: As the separation distance increases and the lead vehicle turns with a tight radius, the following vehicle will cut the corner if it turns directly towards the lead vehicle.

The following vehicle is steered to the desired heading and acts as if it is being towed by the lead vehicle. The towing aspect of the RPV following method introduces a different shortcoming to the leader/follower problem. When the lead vehicle performs a tight turn, the following vehicle will cut the corner of the turn as seen in Figure 4.4. This effect is exaggerated as the separation distance increases. Accordingly, the RPV following method is limited to applications with short following distances or predominantly straight paths. In order to reduce the impact of these limitations, a modified RPV following method is used to reduce the effective separation distance of the two vehicles without constraining the physical separation distance. This method uses a combination of differential GPS carrier phase algorithms including the DRTK algorithm and a time difference carrier phase (TDCP) algorithm.

4.1 TDCP positioning

The time difference carrier phase (TDCP) algorithm is conceptually similar to the DRTK algorithm in that a difference of two measurements is used to minimize the affect of common GPS errors on position estimation. The TDCP algorithm is used to compute the change in the position of one receiver from one measurement epoch to the next measurement epoch. Recall the GPS carrier phase measurement model from Equation (2.2). The difference between two successive carrier phase measurements is given in Equation (4.2).

$$\begin{aligned}\phi^s_{a_k} - \phi^s_{a_{k-\tau}} &= r^s_{a_k} + cdt_{a_k} + cdt^s_k + T^s_{a_k} - I^s_{a_k} + \lambda N^s_{a_k} + v^s_{a_k} \\ &\quad -r^s_{a_{k-\tau}} - cdt_{a_{k-\tau}} - cdt^s_{k-\tau} - T^s_{a_{k-\tau}} + I^s_{a_{k-\tau}} - \lambda N^s_{a_{k-\tau}} - v^s_{a_{k-\tau}} \end{aligned} \quad (4.2)$$

The majority of the common mode errors are remove as a result of the subtraction. For a short time step, the satellite clock error is nearly equal to the value from the previous measurement epoch and is removed. The ionospheric and tropospheric effects are largely removed and any residual atmospheric error is ignored. Assuming that there is no cycle slip of the carrier signal between measurements, the carrier ambiguity is also removed through subtraction. The result is an observation of the change in the range from receiver a to satellite s from time $k-\tau$ to time k corrupted by the receiver clock drift and noise, where τ is the measurement time step.

$$\phi^s_{a_{k-\tau,k}} = r^s_{a_{k-\tau,k}} + cdt_{a_{k-\tau,k}} + v^s_{a_{k-\tau,k}} \quad (4.3)$$

The change in the range from receiver a to satellite s can be rewritten as the range from a to s at time k minus the range from a to s at time $k-\tau$; each range is expressed as the dot product of the line of sight unit vector from receiver to satellite and vector components of

the range in the ECEF frame.

$$\phi^s_{a_{k-\tau,k}} = G^s_{a_k} \begin{bmatrix} r^s_{ax_k} \\ r^s_{ay_k} \\ r^s_{az_l} \end{bmatrix} - G^s_{a_{k-\tau}} \begin{bmatrix} r^s_{ax_{k-\tau}} \\ r^s_{ay_{k-\tau}} \\ r^s_{az_{k-\tau}} \end{bmatrix} + cdt_{a_{k-\tau,k}} + v^s_{a_{k-\tau,k}} \tag{4.4}$$

Note that G is the geometry matrix given by the unit vector from receiver a to satellite s.

$$G^s_{a_k} = \begin{bmatrix} u^s_{ax_k} & u^s_{ay_k} & u^s_{az_k} \end{bmatrix} \tag{4.5}$$

The range terms in Equation (4.4) are regrouped into terms associated with the change in the satellite position and terms associated with the change in the receiver position seen in Equation (4.6).

$$\begin{aligned} \phi^s_{a_{k-\tau,k}} \quad = \quad & G^s_{a_k} \begin{bmatrix} r^s_{x_k} \\ r^s_{y_k} \\ r^s_{z_l} \end{bmatrix} - G^s_{a_{k-\tau}} \begin{bmatrix} r^s_{x_{k-\tau}} \\ r^s_{y_{k-\tau}} \\ r^s_{z_{k-\tau}} \end{bmatrix} \\ & + G^s_{a_k} \begin{bmatrix} r_{ax_k} \\ r_{ay_k} \\ r_{az_l} \end{bmatrix} - G^s_{a_{k-\tau}} \begin{bmatrix} r_{ax_{k-\tau}} \\ r_{ay_{k-\tau}} \\ r_{az_{k-\tau}} \end{bmatrix} + cdt_{a_{k-\tau,k}} + v^s_{a_{k-\tau,k}} \end{aligned} \tag{4.6}$$

Assuming that the line of sight unit vector does not change significantly over the measurement time step, the time difference carrier phase measurement minus the change in the satellite position is expressed as a function of the current unit vector, the change in the

receiver position, the receiver clock drift, and noise.

$$\phi^s_{a_{k-\tau,k}} + G^s_{a_{k-\tau}} \begin{bmatrix} r^s_{x_{k-\tau}} \\ r^s_{y_{k-\tau}} \\ r^s_{z_{k-\tau}} \end{bmatrix} - G^s_{a_k} \begin{bmatrix} r^s_{x_k} \\ r^s_{y_k} \\ r^s_{z_l} \end{bmatrix} = \begin{bmatrix} G^s_{a_k} & 1 \end{bmatrix} \begin{bmatrix} r_{ax_{k-\tau,k}} \\ r_{ay_{k-\tau,k}} \\ r_{az_{k-\tau,k}} \\ cdt_{a_{k-\tau,k}} \end{bmatrix} + v^s_{a_{k-\tau,k}} \tag{4.7}$$

The change in the position of the receiver is then estimated using weighted least squares. The weighting matrix is derived from the variance of the carrier phase measurements based on the carrier to noise ratio as seen in Equation (2.24). Note that the carrier phase measurements are checked for cycle slips as described in Section 2.2.2 to ensure that the carrier ambiguity is removed prior to estimating the change in position.

4.2 DRTK/TDCP Following

As previously stated, the DRTK/TDCP following method is a modification of the RPV following method. Originally introduced in [35], the DRTK/TDCP following method reduces the effective following distance by using the RPV to a virtual leader position to calculate the desired heading of the following vehicle. The virtual leader position acting as the terminus of the RPV is actually a position of the lead vehicle at a previous GPS measurement epoch. The DRTK/TDCP following method is shown visually in Figure 4.5. The RPV of interest, $\text{RPV}_{k,k-n}$, is shown in green and is the RPV between the following vehicle's current position P^F_k, and the lead vehicle's previous position, P^L_{k-n} at time $k-n$. $\text{RPV}_{k,k-n}$is calculated by subtracting the change in the following vehicle's position from time $k-n$ to time k from the relative position vector, RPV_{k-n}, shown in black. The change in the follower's position from time $k-n$ to time k is calculated using Equation (4.8).

$$\Delta P^F_{k-n,k} = \sum_{i=k-n}^{k} \Delta P^F_i \tag{4.8}$$

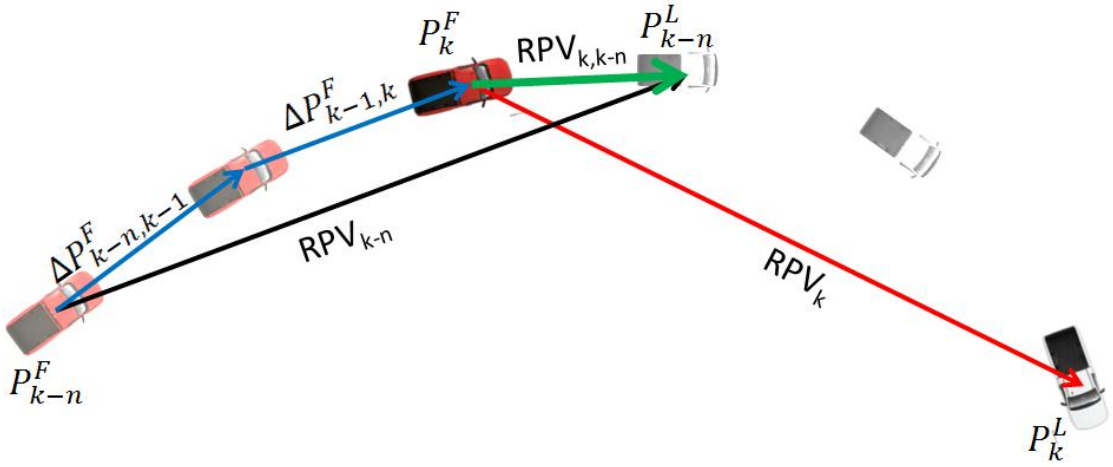

Figure 4.5: Using past knowledge of the lead vehicle's position relative the following vehicle and knowledge of the change in the position of the follower, the following vehicle steers toward a virtual leader position with a much shorter separation distance. The current leader and follower positions are shown in bright white and bright red respectively. The transparent white and red vehicles represent the previous leader and follower positions.

The TDCP algorithm is used to estimate the change in the following vehicle's position at each GPS measurement epoch, represented by ΔP^F_i. The RPV between the vehicles is estimated at each measurement epoch using the DRTK algorithm. With these estimates of the RPV and the change in the following vehicle's position, the RPV to the virtual leader is calculated using Equation (4.9).

$$RPV_{k,k-n} = RPV_{k-n} - \Delta P^F_{k-n,k} \tag{4.9}$$

The desired heading angle is computed using Equation (4.1).

To perform the steps of the DRTK/TDCP following method, a database of RPV and ΔP^F values is maintained. The values are stored sequentially and once a RPV is used to compute the relative position to a virtual leader position, all RPV and ΔP^F values occurring prior to that measurement are deleted to limit the size of the database. As with the RPV following method, the virtual leader position is selected based on minimum look ahead distance. The distance to the virtual leader position is computed starting with the current relative position vector, $RPV_{k,k}$. If that distance is greater than the look ahead distance, the next previous measurement epoch is considered and the $RPV_{k,k-1}$ is computed

to the virtual leader position P^L_{k-1}. If the magnitude of $RPV_{k,k-1}$ is still greater than the look ahead distance, the $RPV_{k,k-2}$ is computed. This continues until the magnitude of the $RPV_{k,k-m}$ is less than the look ahead distance and the previously computed measurement is used, $RPV_{k,k-(m+1)}$. This ensures that the closet virtual leader position that exceeds the look ahead distance is used. Notice that if the magnitude of the current relative position vector is less than the look ahead distance the DRTK/TDCP following method reverts to the RPV following method.

An additional point of interest in the DRTK/TDCP following method is the accuracy of the estimated change in the following vehicle's position. Since the individual change in position estimates are based on differential GPS carrier phase measurements, the error in any one ΔP^F estimate is expected to be on the order of centimeters. However, since the estimates from the TDCP algorithm contain some level of residual error, as the estimates are accumulated the error increases. Accordingly the accuracy of the TDCP is examined in the next section along with the effectiveness of the DRTK/TDCP following method as compared to GPS waypoint following.

4.3 Experimentation and Results

4.3.1 TDCP Error Analysis

The TDCP algorithm was first tested using data collected with a Novatel Propak V3 GPS receiver attached to a test vehicle. The vehicle was driven near the National Center for Asphalt Technology test track for approximately ten minutes as data was collected at 5 Hz. The change in the vehicle's position between GPS measurement epochs was estimated in post process with the TDCP algorithm. The resulting estimates were compared to a reference solution computed by subtracting consecutive RTK position solutions. The performance of the TDCP algorithm is shown in Figure 4.6 along with the performance of the standard position solution reported by the Novatel receiver. The error in the TDCP estimate and the error in the change of the standard Novatel position solution are plotted in the figure. The

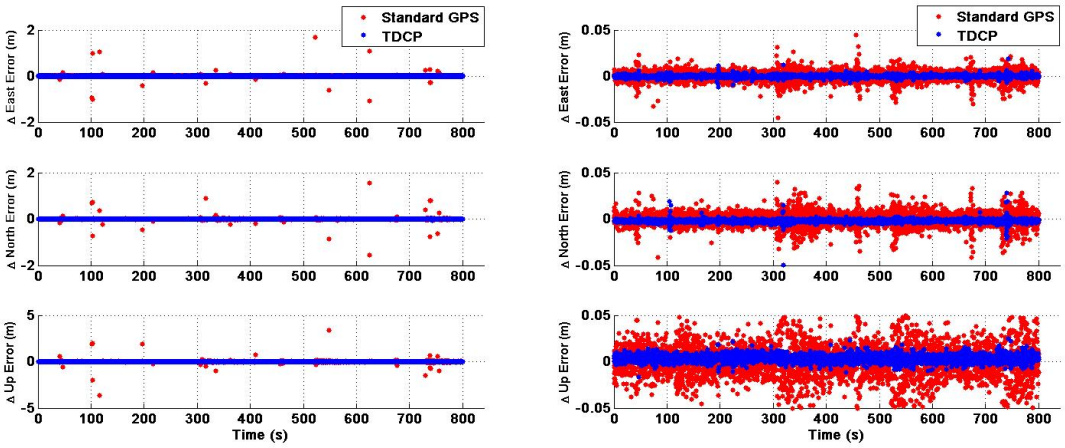

Figure 4.6: Error in the change in the position of a moving receiver for standard GPS position solution and TDCP estimation. The figure on the right is a zoomed view of the figure on the left.

Table 4.1: Standard Deviation of Errors in Change in Position Estimates

Standard GPS			TDCP		
$\sigma_{\Delta East}$(cm)	$\sigma_{\Delta North}$(cm)	$\sigma_{\Delta Up}$(cm)	$\sigma_{\Delta East}$(cm)	$\sigma_{\Delta North}$(cm)	$\sigma_{\Delta Up}$(cm)
5.4	6.9	25.0	0.12	0.2	0.34

image on the left of the figure shows the larger errors in the standard position solution with some errors over one meter. On the right, a closer view of the errors resulting from each method is shown. Clearly each method results in near zero means errors with the standard position solution exhibiting significantly higher deviation. The standard deviations of the errors in the TDCP solution and the standard GPS solution are given in Table 4.1. While each method results in a standard deviation of less than one meter, the standard deviation of the standard GPS solution is more than one order of magnitude higher than the TDCP solution.

Figure 4.6 and Table 4.1 show that the TDCP algorithm is capable of estimating the change in the vehicle's position with sub-centimeter errors. The DRTK/TDCP following method described in this chapter requires that the TDCP estimates be accumulated to compute the change in the follower's position over several measurement epochs. Therefore, the TDCP estimates were accumulated over the full data set with the initial position of the

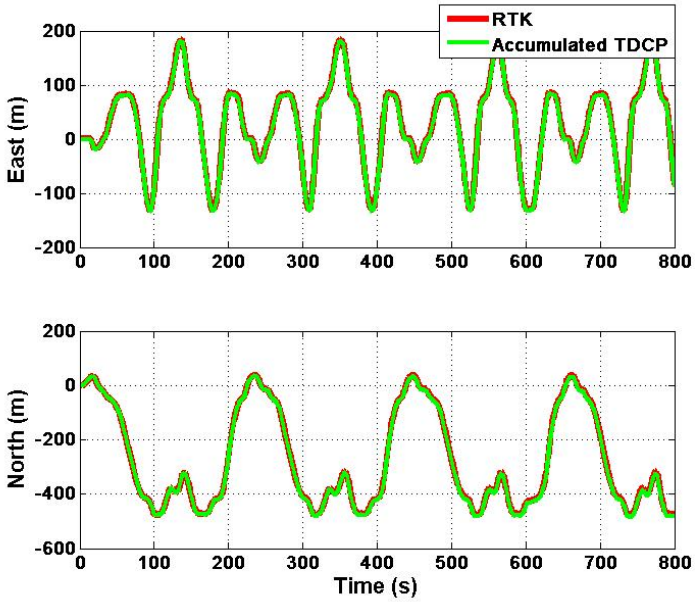

Figure 4.7: East and North positions on a receiver comparing the accumulated TDCP estimates to the reference RTK solution.

vehicle taken to be the origin of a local East, North, Up navigation frame. The accumulated TDCP East and North estimates and the RTK reference positions are shown in Figure 4.7.

As previously stated, the TDCP estimates contain residuals errors that can affect the accumulated position estimates. These errors are due to unaccounted for effects such as changing multipath effects, residual satellite clock errors, and residual atmospheric effects. The assumption of constant line sight unit vectors also contributes to the TDCP errors. The result of these effects are time correlated biases in the TDCP change in position estimates. When this biases are accumulated to compute the change in the position of the vehicle over several measurement epochs, the error in the estimate increases. This tendency is shown in Figure 4.8 where the error in the accumulated TDCP estimate is plotted over a thirteen minute data set. The East position error increases with some variation while the North position error increases nearly linearly. The horizontal error reaches 1 meter in approximately 100 seconds.

To better characterize the error growth of the accumulated TDCP estimates, data was collected on a stationary GPS receiver for twenty-four hours and analyzed. Allan variance

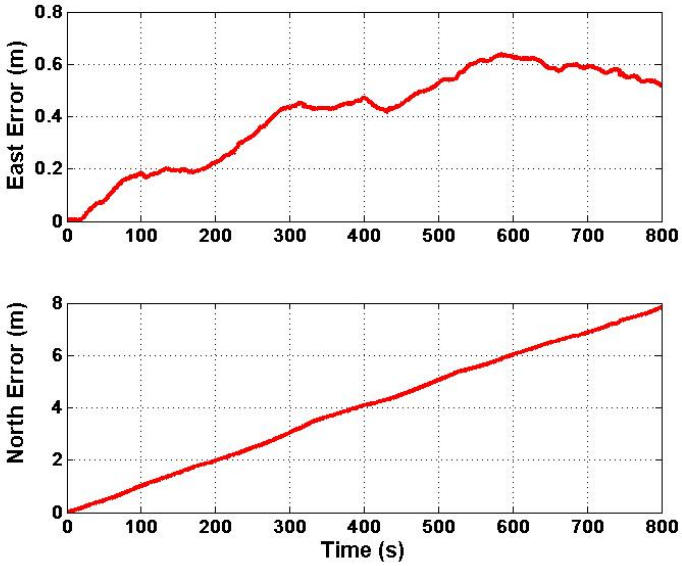

Figure 4.8: Error in the accumulated TDCP position estimate relative to the RTK solution.

analysis was used to examine the variability of the accumulated TDCP estimates as the number of accumulation increases. Originally developed to study the stochastic properties of clocks and oscillators [1], the Allan variance is used in this thesis to compare the accumulated TDCP performance to standard GPS positioning. In general, the Allan variance is computed for a range of selected averaging times and is a measure of the variability of the data sequence for each averaging time. For a formal definition of the Allan variance and for studies on the use of Allan variance analysis to characterize stochastic processes see [1] and[36].

The twenty-four hour data set was divided into averaging times ranging from 0.2 seconds to 12 hours. In Figures 4.9 through 4.11, the Allan deviations of the accumulated TDCP East, North, and Height estimates are shown in blue, and the Allan deviations of the standard GPS East, North, and Height positions are shown in red. Note that the Allan deviation is the square root of the Allan variance and that the values are plotted on a log-log scale in the figures. The figures show that for short averaging times the TDCP algorithm produced more consistent results than the standard GPS solution, as was expected. For the shortest averaging times, the Allan deviation corresponds closely to the standard deviation of the dynamic data set presented in Table 4.1. Recall that the TDCP standard deviation was on

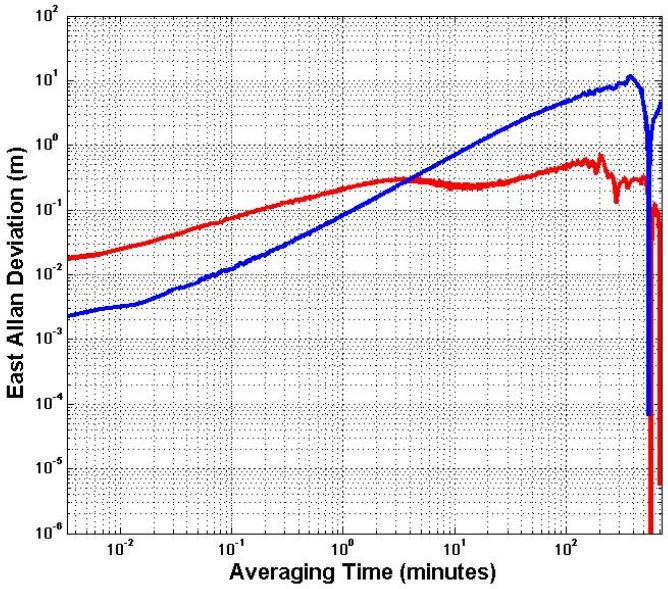

Figure 4.9: East position Allan deviation of the accumulated TDCP (blue) and the standard GPS position (red)

the order of millimeters and the standard GPS position standard deviation was on the order of centimeters. Also, the vertical position estimate produces the highest variance as seen in the both the table and the Allan deviation plots. For higher averaging times the deviation of the accumulated TDCP estimates is near 10 meters while the deviation of the standard GPS position levels off below 1 meter. The spikes in the figures near the maximum averaging times are due to the fact that the twenty-four hour data set can only be subdivided into a few set of data of that length. Therefore, the deviation is being computed with only a few data points resulting in higher volatility.

As the averaging time increases, the Allan deviation of the accumulated TDCP estimates overtakes the Allan deviation of the standard GPS solution. A closer view of the crossover of the East and North deviations can be seen in Figure 4.12. Notice that the values are now plotted on a linear scale. The leveling off effect of the Allan deviation of the standard GPS position is clear on the linear scale with a maximum Allan deviation of approximately 0.3 meters. As was seen with the error of the accumulated TDCP estimates in Figure 4.8, the accumulated TDCP deviation increases nearly linearly as the averaging time increases. The

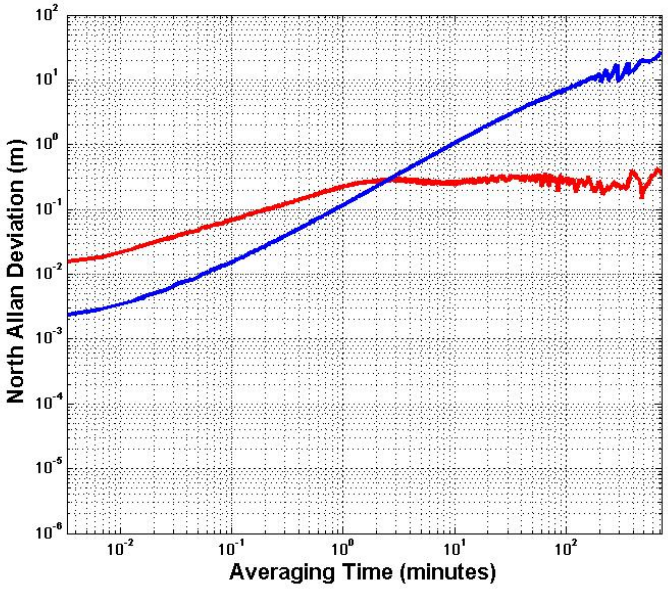

Figure 4.10: North position Allan deviation of the accumulated TDCP (blue) and the standard GPS position (red)

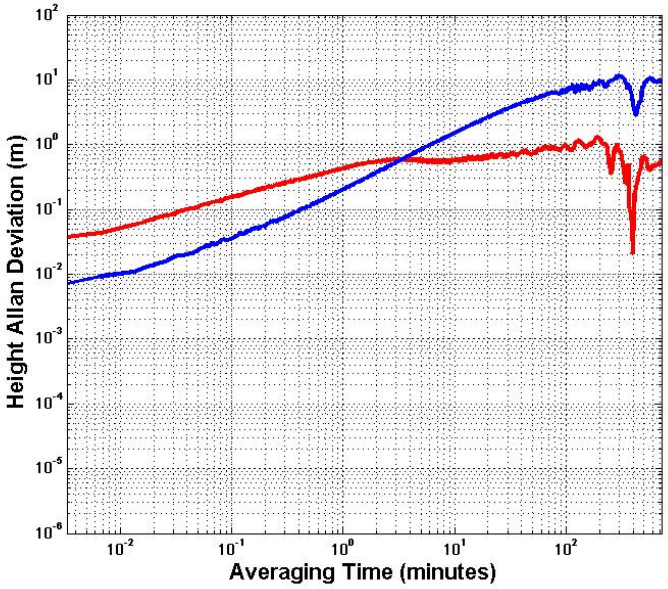

Figure 4.11: Height position Allan deviation of the accumulated TDCP (blue) and the standard GPS position (red)

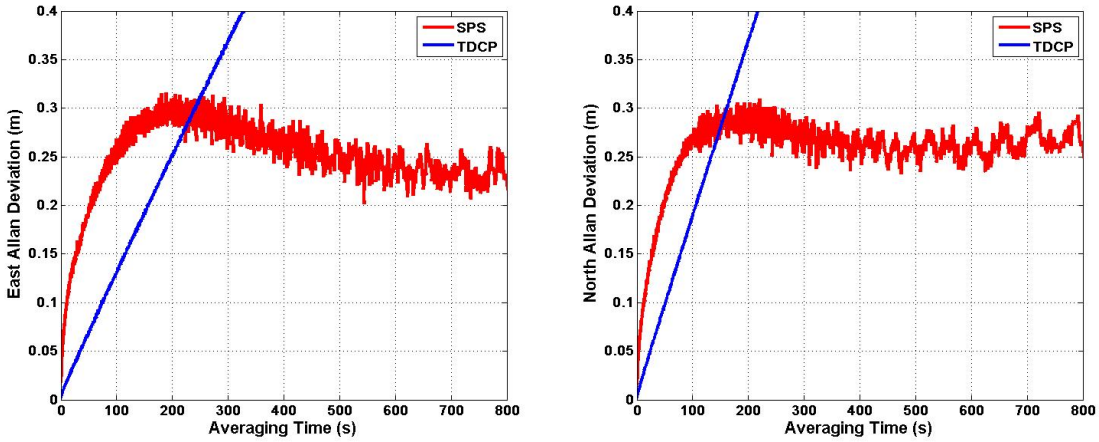

Figure 4.12: East and North Allan deviation of the accumulated TDCP (blue) and the standard GPS position (red)

accumulated TDCP deviation increases beyond the deviation of the standard GPS position at approximately 230 seconds in the East position and approximately 150 seconds in the North position.

The implications of the accumulated TDCP error growth on the DRTK/TDCP following method are seen by noticing that the averaging times in Figure 4.12 can be though of as the time interval between the lead vehicle and following vehicle. Accordingly, based on the results shown in Figure 4.12, if the following vehicle is less than 150 seconds behind the lead vehicle; the accumulated TDCP estimates will provide a more accurate and consistent estimate of the change in the position of the following vehicle than standard GPS positioning. By assuming that the following vehicle is moving at a constant speed, the averaging time or following time can be converted to a following distance. The Allan deviations of the accumulated TDCP estimates and the standard GPS positioning solution are shown as a function of following distance based on a variety of constant speeds in Figure 4.13. As seen in the figure, the accumulated TDCP Allan deviation is lower than the deviation of standard GPS positioning for different following distances based on the speed of the vehicle. As the speed of the following vehicle increases, the accumulated TDCP estimates outperform standard GPS positioning for longer following distances. In Table 4.2, the Allan deviations

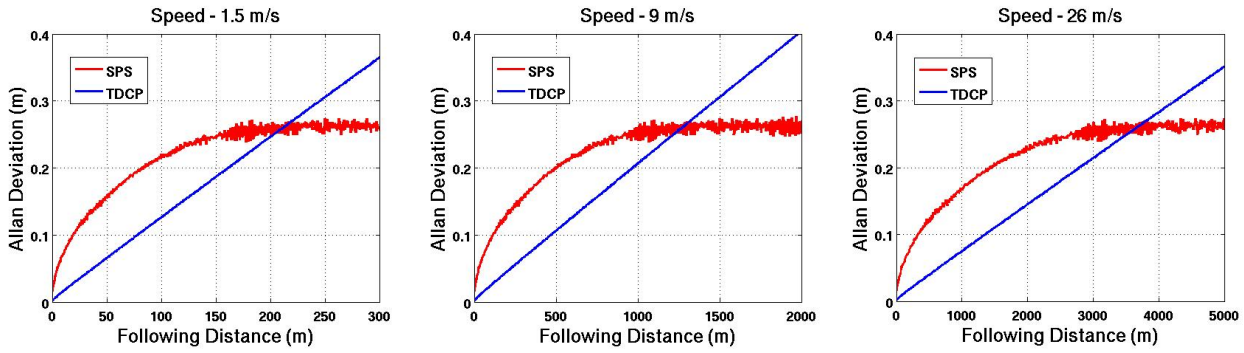

Figure 4.13: Allan deviation of the accumulated TDCP and the standard GPS positioning lateral position estimation as a function of following distance based on a constant speed

Table 4.2: Accumulated TDCP and Standard GPS Positioning Allan deviations as a function of Following Distance

Speed - 1.5 m/s			Speed - 9 m/s			Speed - 26 m/s		
Following Distance (m)	SPS (cm)	TDCP (cm)	Following Distance (m)	SPS (cm)	TDCP (cm)	Following Distance (m)	SPS (cm)	TDCP (cm)
190	25.5	23.4	1150	25.4	23.6	3300	25.4	23.4
200	26.4	24.7	1200	26.4	24.7	3575	26.4	25.3
210	25.8	25.8	1250	25.1	25.6	3650	25.2	25.8
220	26.3	27.0	1300	25.4	26.6	3775	26.8	26.7
230	26.4	28.2	1350	25.7	27.7	4000	26.1	28.2

of the accumulated TDCP estimates and the standard GPS positioning are shown for the same three selected speeds. Following distances shown in the table were selected to show the point of intersection of the accumulated TDCP and standard GPS positioning Allan deviations. The speeds were selected to cover a range of operating conditions such as walking speeds (1.5 m/s), slower driving speeds (9 m/s), and highway driving speeds (26 m/s). The accumulated TDCP estimates provided lower Allan deviations for following distances less than approximately 200 meters at walking speeds, for distances less than 1200 meters at slower driving speeds, and for distances less than 3500 meters at highway speeds.

The twenty-four hour data set was also used to determine the mean time to 1 meter horizontal error when accumulating TDCP estimates. For this analysis the TDCP estimates were accumulated until the horizontal error (the euclidean norm of the East and North error)

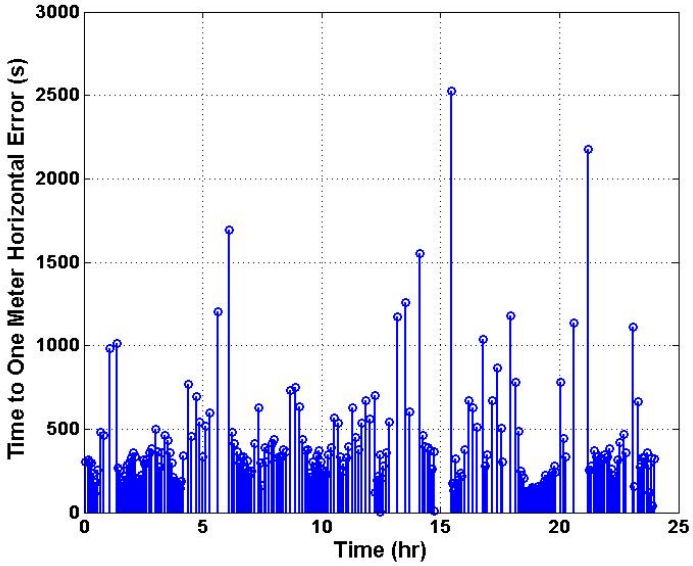

Figure 4.14: Time to one meter horizontal error for accumulated TDCP estimates

exceeded 1 meter; then the time recorded and the value was reset to zero. The results are shown in Figure 4.14. The mean time to 1 meter error was 378 seconds with a maximum value of over 2500 seconds and a minimum value of 3.4 seconds.

4.3.2 DRTK/TDCP Following and Waypoint Following

Finally, a comparison of the DRTK/TDCP following method and the waypoint (breadcrumb) following method was performed. Each method was used to navigate an automated ATV Corp. Prowler all-terrain vehicle (ATV) to reproduce the path of a human driven Infiniti G35 sedan. The Prowler ATV and Infiniti G35, seen in Figure 4.15, were each equipped with a Novatel Propak V3 receiver and a 900 MHz radio modem for inter-vehicle communication. In addition to GPS, the Prowler was also equipped with a Crossbow IMU 440, an Advantech computer, and a SmartMotor for steering control. Additional hardware was used to communicate actuator commands between the navigation processor on the Advantech computer and the SmartMotor. The heading error and the rate of change of the heading error of the Prowler were regulated using a proportional-derivative controller (PD) operating at 20Hz. Heading errors were calculated between the desired heading angle (estimated using

Figure 4.15: Infiniti G35 and Prowler ATV

either the DRTK/TDCP or the waypoint following methodology described in this chapter) and the current heading of the Prowler. The current heading of the Prowler was estimated in a loosely coupled GPS/INS filter and the rate of change of the heading error was estimated by numerically differentiating the heading error over successive iterations.

Results of the DRTK/TDCP following method are shown in Figure 4.16. An RTK system was used to record the positions of the lead vehicle and following vehicle as the path was driven. Let it be stated again that the lead vehicle was human driven and the following vehicle was steered autonomously. The speed of the following vehicle was maintained manually. In the figure, the following vehicle is seen to effectively reproduce the path of the lead vehicle. The following vehicle deviates slightly from the path in the first corner near the coordinates East – 40 meters and North – 20 meters. This may be due to fluctuations of the speed of the following vehicle which will change the look ahead distance used to select the virtual leader position. Notice that the following vehicle reproduce the path with little to no bias on the straight sections of the path.

The waypoint following method was first implemented using the RTK position solution of the lead vehicle with the expectation that the results would be similar to the DRTK/TDCP following method. The DRTK/TDCP following method is expected to outperform the waypoint following method when a RTK base station is unavailable. As seen in Figure 4.17,

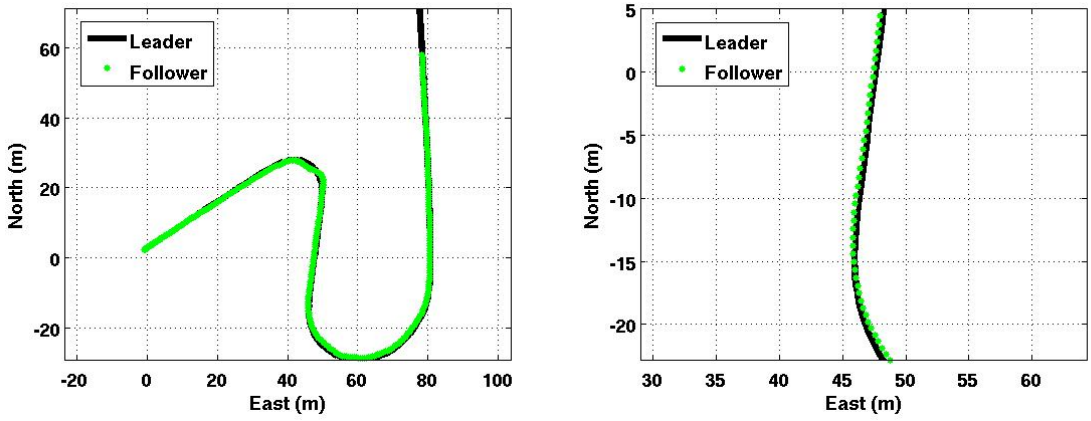

Figure 4.16: RTK positions of the lead vehicle and following vehicle using the DRTK/TDCP following method

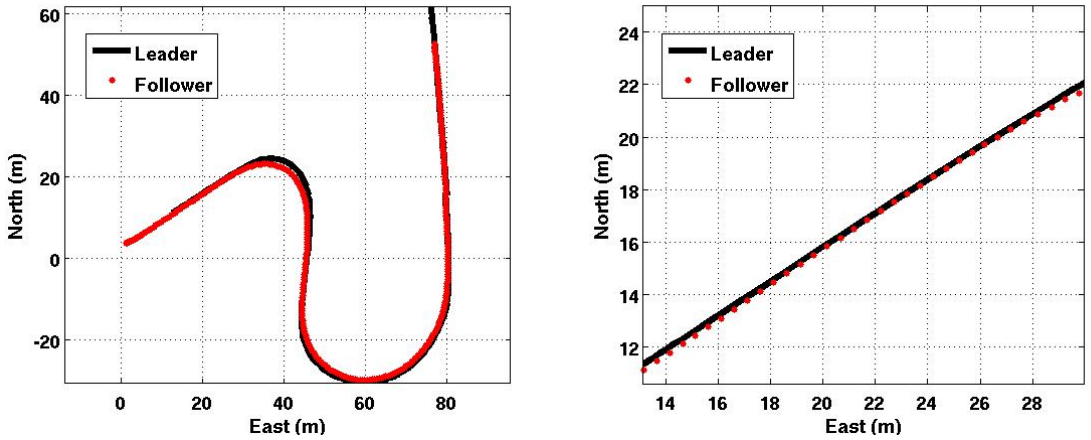

Figure 4.17: RTK positions of the lead vehicle and following vehicle using the waypoint following method with the RTK position of the lead vehicle

the waypoint following method using the RTK position of the lead vehicle produces results comparable to the DRTK/TDCP following method. Again, on the straight sections of the path the following vehicle reproduces the path without significant lateral bias. However, the following vehicle does turn inside the path in the first turn. The speed of the following vehicle and the resulting look ahead distance may account for this phenomenon

To evaluate the effectiveness of the waypoint following method when RTK is unavailable, the Prowler was steered with the waypoint following method using the lead vehicle's standard GPS position as reported by the Novatel receiver. The results of the test are shown in

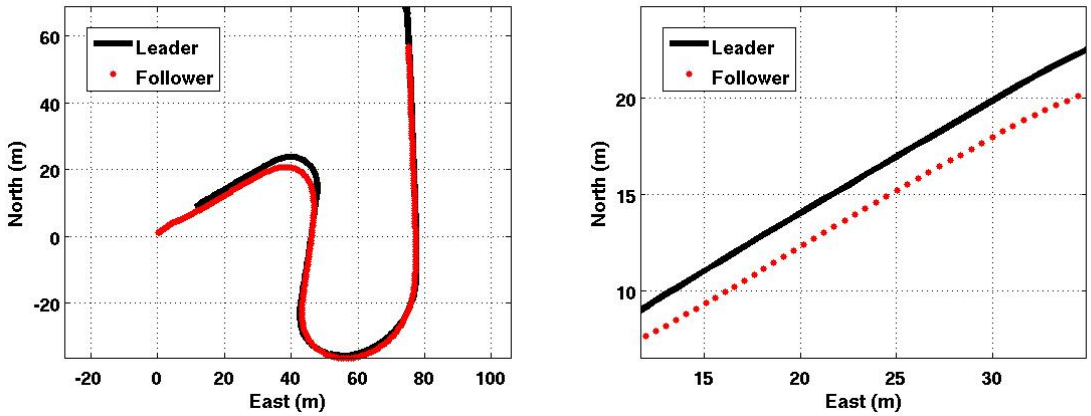

Figure 4.18: RTK positions of the lead vehicle and following vehicle using the waypoint following method with the standard GPS position of the lead vehicle

Figure 4.18. Clearly, the path of the following vehicle is offset laterally from the path of the lead vehicle as expected due to errors in the standard GPS position. For comparison, the DRTK/TDCP following method and the waypoint following method were used to duplicate the same path of the lead vehicle. This was done by recording the lead vehicle's standard GPS position while using the DRTK/TDCP following method to follow the lead vehicle. The waypoint following method was then used to reproduce the recorded path of the lead vehicle. The DRTK/TDCP follower positions and the waypoint follower positions are plotted along with the lead vehicle positions in Figure 4.19. The Prowler reproduces the path of the lead vehicle using either following method. However, the waypoint following method using standard GPS positions again produces a path with a lateral bias relative to the lead vehicle. The lateral errors for each following method are shown in Figure 4.20. The lateral errors of the DRTK/TDCP following method are most prominent in the turns as seen on the 20-30 second and 40-60 second intervals. At the 60 second mark the error in the DRTK/TDCP method settles to centimeter level as the path straightens. The lateral error of the waypoint following method is significantly higher for the majority of the path with a maximum error of nearly 3 meters. The waypoint method also exhibits an offset of approximately 0.5 meters during the straight portion of the path starting a the 50 second mark. Error statistics for

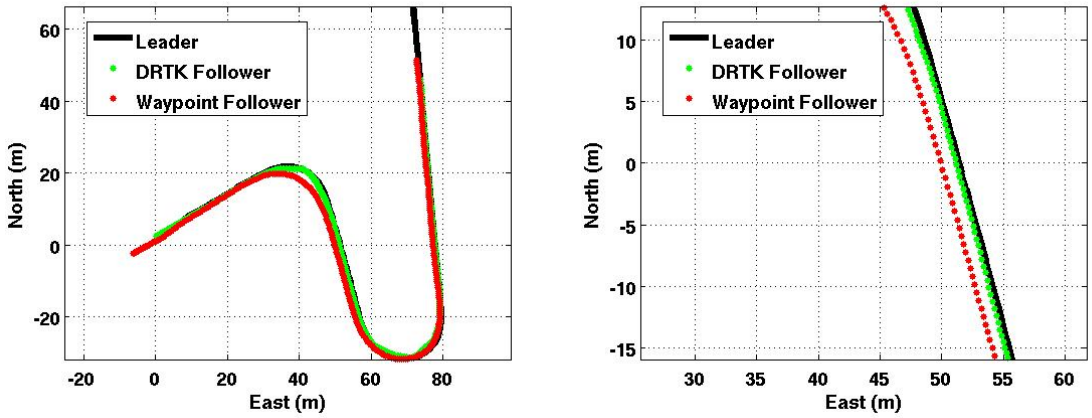

Figure 4.19: RTK positions of the lead vehicle, the following vehicle using the DRTK/TDCP following method, and the following vehicle using the waypoint following method with the standard GPS position of the lead vehicle

Table 4.3: Lateral Error Comparison of DRTK/TDCP Following and Waypoint Following

	DRTK/TDCP	Waypoint (RTK)	Waypoint (Standard)
Mean Lateral Error (m)	0.30	0.44	0.81
Error Variance (m^2)	0.09	0.18	0.49

several test runs using both the DRTK/TDCP following method and the waypoint following method are provided in Table 4.3. The results of waypoint following with RTK positions and with standard GPS positions are shown. As expected the waypoint following method is comparable to the DRTK/TDCP following method when RTK positions are available. The mean lateral error nearly doubles when only standard GPS positions are available. It is important to note that the reported error includes both the error due to the navigation algorithm and error due to the vehicle controller. Also note that the speed of the following vehicle was controlled manually and that the speed influences the selected leader position used to calculate the desired heading. Variation in the speed of the vehicle between the DRTK/TDCP run and the waypoint run affect the performance of each method, particularly in the turns.

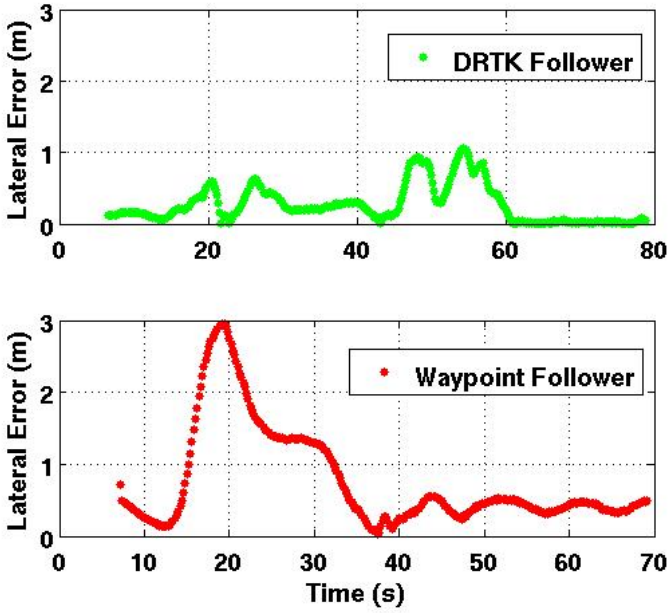

Figure 4.20: Lateral error of the DRTK/TDCP and waypoint following method. Standard GPS positions are used for waypoint following

4.4 Conclusions

In this chapter, autonomous vehicle navigation using GPS is examined. Two methods are discussed: DRTK/TDCP following and waypoint following. The DRTK/TDCP following method requires accurate estimates of the change in the position of the following vehicle between GPS measurement epochs. Accordingly, an algorithm using time difference carrier phase measurement is presented. The accuracy of the TDCP algorithm is evaluated based single epoch estimation and accumulated position change estimation. The TDCP algorithm provided significantly improved performance over standard GPS position for single epoch change in position estimation. As the TDCP estimates were accumulated to determine the change in position over several measurement epochs the solution degrades. Allan variance analysis indicated that the TDCP algorithm provided improvement over standard GPS positioning when accumulated for less than two to three minutes on average. Despite the limitation of the accumulated TDCP position estimation method, it is an effective alternative to standard GPS positioning for the DRTK/TDCP following method since the number

of required accumulations is a function of the distance to the virtual leader position which can be selected by the user.

The DRTK/TDCP following method and the waypoint following method were compared using an automated ATV. The ATV autonomous duplicated the path of a human driven lead vehicle using both the DRTK/TDCP method and the waypoint method. When using a RTK position solution for the lead vehicle, the waypoint following method provided comparable performance to the DRTK/TDCP following method. The waypoint following performance degraded significantly when standard GPS leader positions were used. The DRTK/TDCP following method reproduced the path of the lead vehicle with a mean lateral error of 30 centimeters.

Chapter 5

Conclusions and Future Work

5.1 Conclusions

In this thesis, differential GPS methods are developed for use in autonomous vehicle following applications. An autonomous vehicle requires robust, accurate positioning information to effectively duplicate the path driven by a lead vehicle. In Chapter 2, carrier phase based differential GPS algorithms were shown to produce relative position vectors between two vehicles with centimeter level errors. Dual frequency and Single frequency algorithms were described and compared based on accuracy and reliability. The accuracy of the dual and single frequency algorithm were shown to be commensurate. However, the availability of the fixed integer high precision solution varied between the algorithms as shown by the time to first fix.

The DRTK algorithms described in Chapter 2 are expanded in Chapter 3 to incorporate high rate inertial measurements. Blending of IMU measurements with GPS measurements exploits the complimentary capabilities of the sensors. The GPS/INS navigation solution combines the fast update, short term accuracy of the IMU with the driftless, global positioning from GPS. The tightly coupled architecture, characterized by the use of GPS pseudorange measurements, was selected for study in this thesis. To combine GPS and IMU measurements from two vehicles, two filter alternatives are proposed - a federated Kalman filter and a centralized Kalman filter. Each filter was described in detail and the results of a comparative analysis were presented. The filters performed with comparable accuracy and reliability; however due to the complexity of the centralized filter approach the federated filter was selected. The dead reckoning performance of the federated DRTK/INS filter was examined as it pertains to the reacquisition of fixed integer carrier phase ambiguity estimates. Results

were presented for the performance of the federated DRTK/INS filter use both dual and single frequency GPS measurements.

In Chapter 4, the use of time differenced carrier phase GPS measurements for change in position estimation is described. The accuracy of the TDCP algorithm over long time periods, up to 24 hours, is examined and compared to standard GPS positioning. Also, the TDCP algorithm is combined with the DRTK algorithm to estimate the relative position vector between the current position of the following vehicle and a previous position of the lead vehicle. This relative position associating the follow vehicle and a virtual lead vehicle is used in an autonomous following application. The DRTK/TDCP following method is tested on an autonomous recreational vehicle. The results of tests are compared to the performance of the same vehicle autonomously navigating a path of GPS waypoints.

5.2 Future Work

Future work in the leader/follower field may continue to focus on non line of sight following. The autonomous following method described in Chapter 4 may be expanded to include velocity control capabilities. Additional sensors, such as optical sensors, may be incorporated to improve functionality. Light Detection and Ranging Sensors (Lidar) and cameras may be used in obstacle avoidance, terrain characterization, or in cooperative localization routines. Some initial strides have been made in characterizing the terrain and mapping features along the path of the lead vehicle using Lidar information and those efforts are described briefly in the following sections.

5.2.1 Leader Path Terrain Characterization

In an attempt to provide the following vehicle with additional information about the path of the lead vehicle, the lead vehicle may be equipped with a three dimensional Lidar. The Lidar provides the range and bearing to features in the field of vision by calculating the time of fight of an emitted pulse which is reflected back to the sensor. With this information

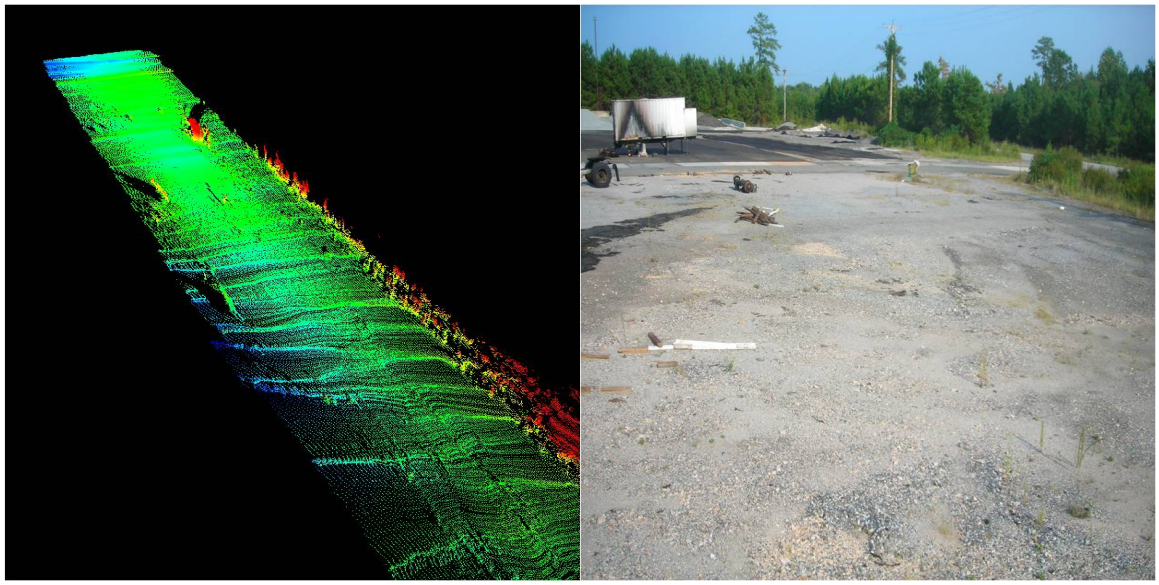

Figure 5.1: Three dimensional point cloud constructed using Lidar data from the lead vehicle showing the variability of the terrain along the path

a three dimensional point cloud of the environment near the lead vehicle can be developed. The coordinates of the cloud are in the frame of the current position of the lead vehicle. Using the TDCP and DRTK algorithms described in this thesis, the point cloud can be resolved into coordinates corresponding to the position of the following vehicle. The result is a three dimensional map of the terrain near the lead vehicle expressed relative to the following vehicles position. A visual representation of a three dimensional point developed using this method is shown in Figure 5.1 along with a picture of the actual terrain. The variability of the surface can be seen clearly in both the point cloud and the picture.

Using the three dimensional point cloud of the terrain near the lead vehicle, a quantities representation of the roughness of the terrain can be calculated. The root mean square elevation and the power spectral density are two methods used to characterize terrains. In Figure 5.2, a plot of the root mean square elevation along the path of the lead vehicle is shown. The data was collected along the path previously shown in Figure 5.1. Generally, the higher root mean square elevation values correspond to rougher terrain. This information may used in adaptive path planning algorithms to maneuver the following vehicle to flatter terrain while maintaining its proximity to the lead vehicles path.

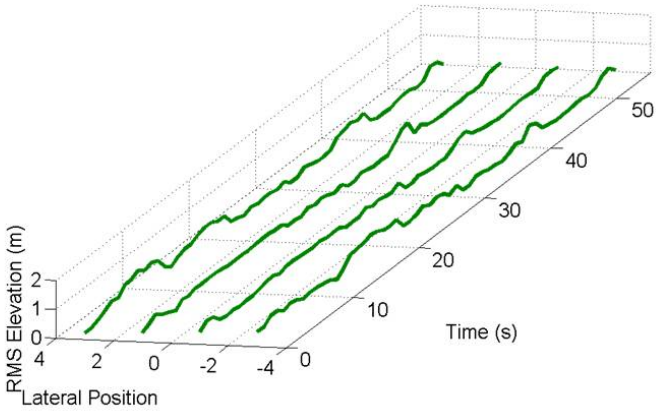

Figure 5.2: The root mean square elevation along the path of the lead vehicle as it travel through a rocky terrain

5.2.2 Leader Path Obstacle Detection

The three dimensional terrain map may also be useful in detecting potentially hazardous obstacles along the path of the lead vehicle. In Figure 5.3, the lead vehicle is traveling in close proximity to a series of concrete barriers. The barriers are clearly detected by the Lidar on the lead vehicle and are present in the resulting point cloud. In this case, it would be useful to isolate points of interest from the complete map corresponding to the borders of the barriers. The wavelet transform can be used to identify points in the three dimensional point cloud which deviation significantly from the surrounding points. An example of the points of interest identified by the wavelet transform is shown in Figure 5.4. The wavelet transform effectively selects points of interest corresponding to the location of the barriers but also identifies the edges of the search space. With refinement, the wavelet transform may prove to be a useful tool in an obstacle avoidance algorithm.

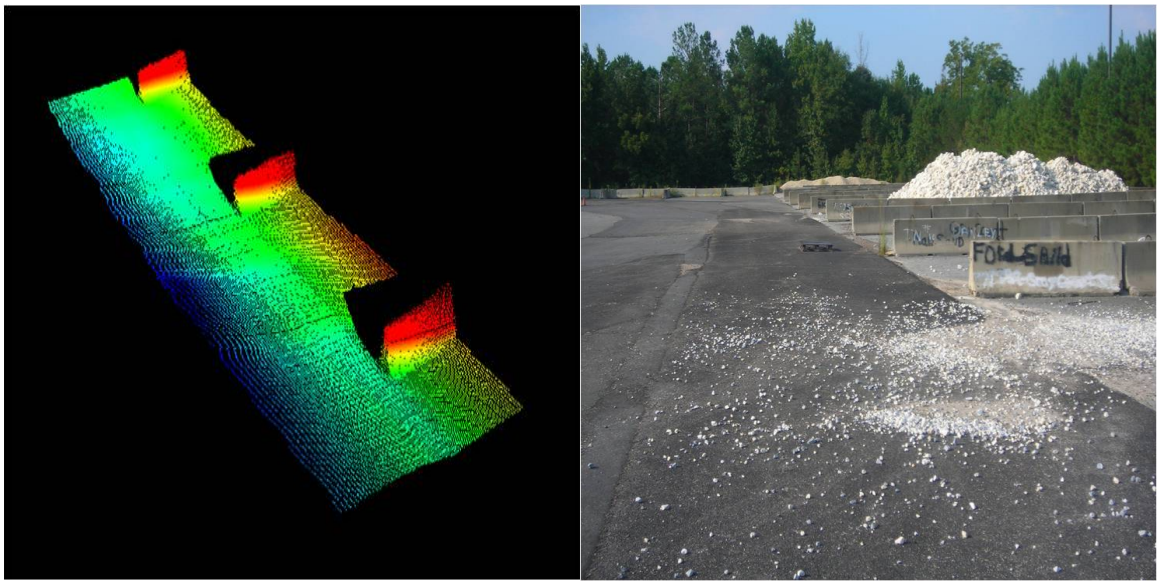

Figure 5.3: Three dimensional point cloud of the lead vehicles path a series of barriers with a picture of the actual terrain

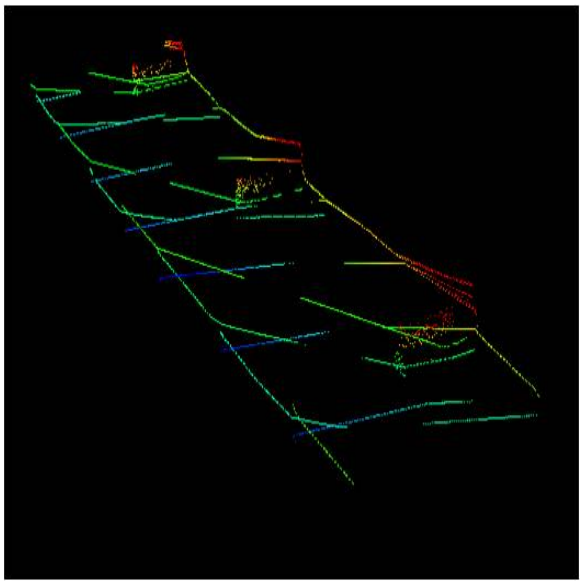

Figure 5.4: Points of interest along the barriers as identified by the wavelet transform

5.2.3 Feature Tracking and Cooperative Localization

One final approach would be to use the additional sensor information to improve the performance of the existing following method. It was shown in Chapter 4 that the accumulation of TDCP estimates leads to growth in the positioning error. In a feature rich environment, it may be possible to bound that error growth by matching features seen by the following vehicle to features previously seen by the lead vehicle. The position of the feature may be recorded as the lead vehicle passes using a combination of the DRTK algorithm and ranging information from a Lidar. This known position may be used to determine the change in the following vehicle's position as it navigates near the feature. This information may be used to improve the TDCP estimates, particularly as the change in position is accumulated along the path. It may also be possible to navigate in the absence of GPS using a cooperative mapping and localization method similar to Simultaneous Localization and Mapping (SLAM).

Bibliography

[1] D. W. Allan. Statistics of atomic frequency standards. 54(2):221–230, 1966.

[2] R. G. Brown and P. Y. C. Hwang. *Introduction to Random Signals and Applied Kalman Filtering*. John Wiley and Sons, Third edition, 1997.

[3] M. E. Cannon, C. Basnayake, S. Syed, and G. Lachapelle. Precise gps sensor subsystem for vehicle platoon control. In *Proceedings of the 16th International Technical Meeting of the Satellite Division of the Institue of Navigation ION GPS 2003*, pages 213–224, 2003.

[4] Fang Chen Chan. *A State Dynamics Method for Integrated GPS/INS Navigation And Its Application to Aircraft Precision Approach*. PhD thesis, Illinois Institute of Technology, May 2008.

[5] Cheng Chen, Han Wang, Ng Teck Chew, J. Ibanez-Guzman, Shen Jian, and Chan Chun Wah. Target-tracking and path planning for vehicle following in jungle environment. In *Proc. ICARCV 2004 8th Control, Automation, Robotics and Vision Conf*, volume 1, pages 455–460, 2004.

[6] B. J. Clark and D. M. Bevly. GPS/INS integration with fault detection and exclusion in shadowed environments. In *Proc. IEEE/ION Position, Location and Navigation Symp*, pages 1–8, 2008.

[7] S. J. Comstock. Development of a low-latency, high data rate, differential GPS relative positioning system for uav formation flight control. Master's thesis, Air Force Institute of Technology, 2006.

[8] S. Crawford, M. Cannon, D. Letourneau, P. Lepage, and F. Michaud. Performance evaluation of sensor combinations on mobile robots for automated platoon control. In *Proceedings of 17th Internation Meeting of the Satellite Division of the Institute of Navigation ION GNSS 2004*, pages 706–717, 2004.

[9] A. Dempster. Correlators for l2c: Some considerations. *Inside GNSS*, 1(7):32–37, October 2006.

[10] S. Dogra, J. Wright, and J. Hansen. Sea-based JPALS relative navigation algorithm development. In *Proceedings of the 18th International Technical Meeting of the Satellite Division of the Institute of Navigation ION GNSS 2005*, pages 2871–2881, 2005.

[11] P. Enge. Local area augmentation of GPS for the precision approach of aircraft. 87(1):111–132, 1999.

[12] Jay A. Farrel and Matthew Barth. *The Global Positioning System and Inertial Navigation*. McGraw Hill, 1999.

[13] S. C. Felter and N. E. Wu. A relative navigation system for formation flight. *IEEE Transactions on Aerospace and Electronic Systems*, 33(3):958–967, 1997.

[14] T. Ford, M. Hardesty, and M. Bobye. Helicopter ship board landing system. In *Proceedings of the 18th International Technical Meeting of the Satellite Division of the Institute of Navigation ION GNSS*, pages 979–988, 2005.

[15] Sylvia Gil, Ruggero Milanese, and Thierry Pun. Combining multiple motion estimates for vehicle tracking. In *In European Conference on Computer Vision*, pages 307–320. SpringerVerlag, 1996.

[16] Mohinder Grewal, Lawrence Weill, and Angus Andrews. *Global Positioning Systems, Inertial Navigation, and Integration*. john Wiley and Sons, Inc., 2001.

[17] P. D. Groves. *GNSS, Inertial, and Multisensor Integrated Navigation Systems*. Artech House, 2008.

[18] P. Joosten and C. Tiberius. Lambda: Faqs. *GPS Solutions*, 6:109–114, November 2002.

[19] E.D. Kaplan and C.J. Hegarty. *Understanding GPS: Principles and Applications*. Artech House, 2006.

[20] S. Khanafseh. *GPS Navigation Algorithms for Autonomous Airborne Refuling on Unmanned Air Vehicles*. PhD dissertation, Illinois Institute of Technology, May 2008.

[21] H. Leppakoski, H. Kuusniemi, and J. Takala. RAIM and complementary Kalman filtering for GNSS reliability enhancement. In *Proc. IEEE/ION Position, Location, And Navigation Symp*, pages 948–956, 2006.

[22] Scott Martin, Jeremy Dawkins, William Travis, and David Bevly. Terrain characterization and feature detection for automated convoys. In *Proceedings of Institute of Navigation GNSS 2010*, 2010.

[23] Scott Martin, William Travis, and David Bevly. Performance comparison of single and dual frequency closely coupled gps/ins relative positioning systems. In *Proc. IEEE/ION Position Location and Navigation Symp. (PLANS)*, pages 544–551, 2010.

[24] P. Mirsa and P. Enge. *Global Positioning System: Signals, Measurements, and Performance*. Ganga-Jamuna Press, 2006.

[25] Teck Chew Ng, J. I. Guzman, and M. D. Adams. Autonomous vehicle-following systems: a virtual trailer link model. In *Proc. IEEE/RSJ Int. Conf. Intelligent Robots and Systems (IROS 2005)*, pages 3057–3062, 2005.

[26] Teck Chew Ng, J. Ibanez-Guzman, Jian Shen, Zhiming Gong, Han Wang, and Chen Cheng. Vehicle following with obstacle avoidance capabilities in natural environments. In *Proc. IEEE Int. Conf. Robotics and Automation ICRA '04*, volume 5, pages 4283–4288, 2004.

[27] Kyle O'Keefe, Mark Petovello, Grerard Lachapelle, and M. Elizabeth Cannon. Assessing probability of correct ambiguity resolution in the presence of time-correlated errors. *The Journal of the Institute of Navigation*, 53(4):269–282, Winter 2006.

[28] B.W. Parkinson and J.J. Spilker. *The global positioning system: theory and applications volume I.* Aiaa, 1996.

[29] B. Pervan, F. C. Chan, D.Gebre-Egziabher, S. Pullen, P. Enge, and G. Colby. Performance analysis of carrier-phase DGPS navigation for shipboard landing of aircraft. *Journal of the Institute of Navigation*, 50(3):181–191, 2003.

[30] M. Petovello, G. Lachapelle, and M. Cannon. Using GPS and GPS/INS systems to assess relative antenna motion onboard an aircraft carrier for shipboard relative GPS. In *Procreedings of the 18th International Technical Meeting of the Satellite Division of the Institute of Navigation ION GNSS 2005*, pages 219–229, 2005.

[31] B. Remondi. Performing centimeter level surveys in seconds with GPS carrier phase: Initial results. *Navigation, Journal of Institute of Navigation*, 32(4):386–400, 1985.

[32] G. Seeber. *Satellite geodesy.* Walter De Gruyter Inc, 2003.

[33] P. J. G. Teunissen. The least-squares ambiguity decorrelation adjustment: A method for fast gps integer ambiguity estimation. *Journal of Geodesy*, 70:65–82, 1995.

[34] P. J. G. Teunissen and S. Verhagen. On the foundation of the popular ratio test for gnss ambiguity resolution. In *Proceedings of the 17th International Technical Meeting of the Satellite Divison of the Institute of Navigation ION GNSS 2004*, pages 2529–2540, 2004.

[35] William Travis. *Path Duplication Using GPS Carrier Based Relative Position for Automated Ground Vehicle Convoys.* PhD dissertation, Auburn University, May 2010.

[36] John Wall. A study of the effects of stochastic inertial sensor errors in dead-reckoning navigation. Master's thesis, Auburn University, August 2007.

[37] M. Wei and K. P. Schwarz. A strapdown inertial algorithm using an earth-fixed cartesian frame. *Journal of the Institute of Navigation*, 37(2):153–167, 1990.

Appendix A

Fault Detection and Exclusion for GPS Error Mitigation

GPS measurements are affected by several error sources previously outline in Chapter 1 of this thesis. Typically these sources of error introduce a predictable variance in the GPS pseudorange, pseudorange rate, and carrier phase measurements. Occasionally, these errors significantly exceed the expected value resulting in a degraded pose estimation. The extraneous measurements are often the result of satellite failure, severe multipath, or receiver failure. Navigation solution degradation due to satellite failure and severe multipath is potentially avoidable given that the faulty measurements are successfully detected. Fault detection and exclusion (FDE) algorithms identify outlining measurements and exclude the outliers from the calculations used to update the state estimates.

In the Kalman filter approach to GPS/INS navigation discussed in Chapter 3, errors in the GPS measurements corrupt the navigation solution through the measurement innovations. Accordingly, the innovations are often used as the test statistics in FDE algorithms. Two fault detection methods incorporating the measurement innovations are innovation filtering and innovation sequence monitoring [17]. Innovation filtering is a snapshot method used to detect immediate large deviations between the predicted measurement and the actual measurement. Innovation sequence monitoring is used to detect errors that are first introduced as small variations but increase with time. Innovation sequence monitoring offers a level of sensitivity that is not available with innovation filtering but is cumbersome to implement requiring multiple parallel filters for proper fault exclusion. For that reason, innovation filtering was selected for implementation.

A.1 Innovation Filtering

Innovation filtering compares the measurement innovations to a predefined threshold in order to identify extraneous measurements. The measurement innovations are the difference between the current measurements and the predicted measurements calculated in the measurement update of the Kalman filter. Since the innovations are a function of the current measurement and the propagated states, the magnitude of the individual innovations varies greatly based on measurement noise and state uncertainty. Therefore, the innovations are scaled before they are compared to the detection threshold. The denominator of the Kalman gain equation is used to normalize the innovations since it represents the expected covariance of the measurement innovations. The covariance, S, is the sum of the projection of the state covariance into the measurement domain and the current measurement covariance as seen in Equation (5.1).

$$S_k = H_k P_k^- H_k^{\mathbf{T}} + R_k \tag{5.1}$$

The measurement innovations, δz, are scaled by the square root of the diagonal elements of S resulting in the vector of test statistics, y.

$$y_{k_i} = \frac{\delta z_{k_i}}{\sqrt{S_{k_{ii}}}} \tag{5.2}$$

The index i is given by $i = 1...m$ where m is the number of measurements. Each elements of y is compared to the fault detection threshold which is chosen to meet a selected probability of false alarm. If the threshold is exceeded, the corresponding rows of the measurement vector and geometry matrix are removed.

A.2 Implementation

The federated DRTK/INS relative positioning algorithm described in Chapter 3 is expanded to include fault detection and exclusion capabilities. The filter architecture requires

the computation of measurement innovations in the individual GPS/INS filters and in the master DRTK/INS filter. Refer to Figure 3.5 for clarification if necessary. The FDE is incorporated in the GPS/INS filters due to the inherent integrity monitoring already present in the DRTK algorithm, in the form of the cycle slip detection. Additional consideration was given to the fact that there is no feedback from the DRTK/INS filter to the GPS/INS filters. It the FDE algorithm were incorporated only at the DRTK/INS level, faulty measurements could be used in the measurement update of the GPS/INS filters, corrupting the individual GPS/INS navigation solutions. The FDE algorithm is not included at both the GPS/INS level and the DRTK level to prevent redundancy.

Early, the measurement innovations of the GPS/INS tightly coupled filter were defined in Equation (3.14). These innovations are scaled as shown in Equations (5.1) and (5.2), and are compared the a threshold value of 3. This threshold is selected to limit the probably of fault alarm to 0.27 percent [17]. The FDE algorithm identifies any extraneous GPS measurements in the GPS/INS filters. The erroneous measurements are removed from the GPS/INS update equations and the corresponding PRN number is sent to the DRTK/INS filter. During the DRTK/INS update step, the measurements from the satellite corresponding that RPN number are removed from consideration.

A.3 Experimentation and Results

Testing the FDE algorithm involved simulating a degradation in a GPS pseudorange measurement. Data was collected on two vehicles as described in Section 3.4. One pseudorange measurement from a satellite visible to both receivers was selected and that pseudorange was corrupted with a simulated additive error. Two error models were used in testing: a constant bias and a first order Gauss Markov random walk.

A range of constant bias values were tested in both single and dual frequency filters to evaluate the sensitivity of the FDE algorithm and to determine the effect of the error on the navigation solution. The biases used in testing ranged from 10 meters to 30 meters and were

added to sixty second sections of a much longer data run. The test was repeated twenty times throughout the data run. A typical response of the GPS/INS filter with and without the FDE algorithm is shown in Figure 5.5. The east and north errors (with respect to the RTK reference solution) of each filter are shown for an added bias error of 25 meters. The error was introduced at 100 seconds, with a duration of sixty seconds and was added to measured pseudorange from 1 of 8 visible satellites. The error was detected by the FDE algorithm at each GPS measurement epoch. Clearly, the error induced a significant deviation in both the east and north position estimates in the filter not equipped with FDE. After the error is removed, at the 160 second mark, the GPS/INS solution returns to the original error levels.

The mean results of the twenty test segments are shown in Table 5.1. The mean percentage of correct detections for the L1 only algorithm and the L1/L2 algorithm are presented along with the mean low precision baseline root mean square error from the DRTK master filter. The high precision baseline errors is not included due to the consistency of the results; the high precision error was sub-centimeter for all cases shown. The FDE algorithm detected no errors with magnitudes less than the minimum value in the table and detected all errors with magnitudes greater than the maximum error in the table. The results show that with either L1 frequency or L1 and L2 frequency measurements the FDE algorithm detected 100 percent of the distorted measurements when the additive error exceeded 18.5 meters. The FDE algorithm exhibited sightly higher sensitivity with dual frequency measurements as 100 percent of the distorted measurements were detected down to 16.5 meters. The DRTK low precision baseline error increases for both the L1 and L1/L2 algorithm as the bias value increase until a significant majority of the faulty measurements are detected. With 100 percent detection the algorithms returns to error level consistent with the results shown in Chapter 3. Recall, the DRTK/INS L1/L2 algorithm had a low precision root mean square error of 13.6 centimeters and the DRTK/INS L1 algorithm had a low precision root mean square error of 22.8 centimeters.

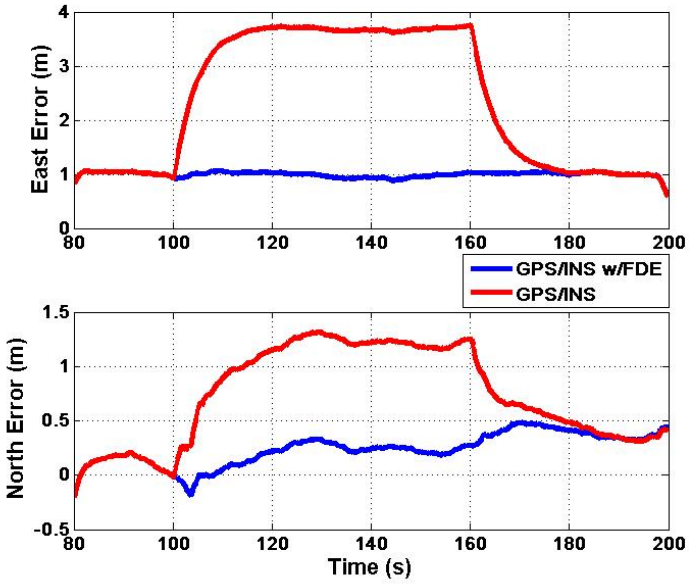

Figure 5.5: GPS/INS filtered solution with one corrupted GPS pseudorange measurement with and without FDE algorithm

Table 5.1: Results of FDE algorithm for a GPS pseudorange measurement corrupted with constant bias error

Bias (m)	L1 Mean Detection (%)	L1 LP Baseline RMSE (cm)	L1/L2 Mean Detection (%)	L1/L2 LP Baseline RMSE(cm)
14.0	0	66.5	0	51.5
14.5	0	68.7	7.5	53.7
15.0	0	70.9	18.2	55.8
15.5	0	73.2	24.2	57.9
16.0	0	75.4	75.3	59.9
16.5	2.6	77.6	100.0	6.5
17.0	17.6	79.9	100.0	6.5
17.5	31.8	79.2	100.0	6.5
18.0	94.3	17.3	100.0	6.5
18.5	100.0	17.3	100.0	6.5

In order to give some context to this analysis, consider the expected pseudorange measurement error due to normally experienced error sources such as ephemeris errors, satellite clock errors, ionosphere delays, troposphere delay, multipath, and thermal noise. According to [28], the cumulative effect of these errors is an expected one sigma range error of approximately 5.3 meters. The simulated errors of 10 and 30 meters therefore represent 2σ and 6σ errors, respectively. Assuming that the errors follow a Gaussian distributed, an error of 10 meters will occur approximately once in 22 measurements during normal operation. An error of 30 meters can be expected only once in over 500 million measurements. Recall that the FDE algorithm detected errors in the 16 to 18 meter range effectively which would correspond to approximately a 3σ error. A 3σ error can be expected to occur once in 370 measurements. Accordingly, a measurement error exceeding the detection capabilities of the FDE algorithm would not be expected to happen often during normal operation. However, in some environments, such as heavy foliage or urban canyons, errors due to multipath can induce significant errors. The effective use of FDE to detect errors in heavy foliage environments was shown in [6].

The second test of the FDE algorithm involved time varying errors. The additive error was simulated as a first order Gauss Markov random walk defined by Equation (5.3).

$$v_{k+1} = e^{-\frac{1}{\tau}dt} v_k + \epsilon_k \tag{5.3}$$

The dynamics of the error were dictated by the time constant, τ, and the variance σ_ϵ^2. Note that ϵ is a zero mean white Gaussian random variable with variance σ_ϵ^2. Several combination of time constants and variances were tested with values of τ ranging from 30 to 110 seconds and values of σ_ϵ^2 ranging from 0.25 to 25 meters. The values are selected based on a study examining carrier phase ambiguity resolution in the presents of time correlated noise performed at the University of Calgary [27]. The variance values of this study extend beyond those of the Calgary study to determine the detection capabilities of the FDE algorithm.

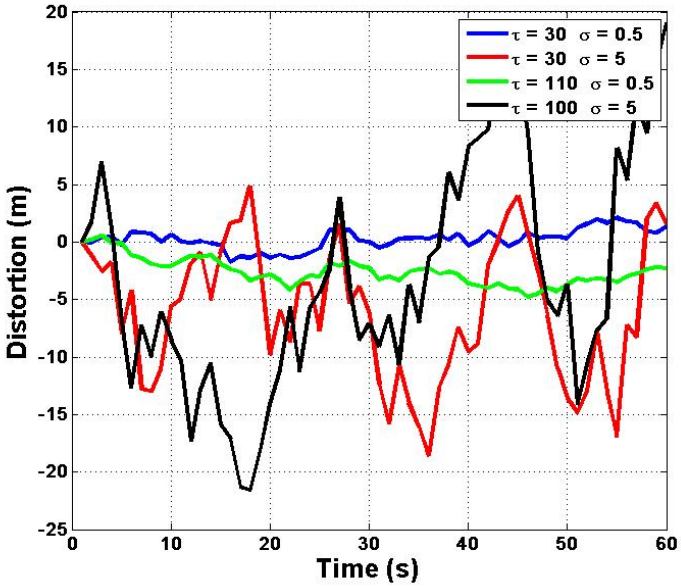

Figure 5.6: Example of the simulated first order Gauss Markov random walk errors used to test the FDE algorithm

Four typical random walk errors are shown in Figure 5.6. It is clear that the variance of ϵ significantly impacts the magnitude of the error, particularly for the 60 second simulation time use in this test. As would be expected from the innovation filtering method, which is a snapshot method, the magnitude of the error was the driving factor in the probability of detection. The random walk errors with low variance values do not reach magnitudes high enough to be detected by the FDE algorithm. As seen in Figure 5.6, the random walk errors with a variance of 5 meters can reach magnitudes well in excess of the sensitivity level established by the bias testing. However, the transient property of the random walk means that the magnitude of the error will not always exceed the expected detection abilities of the FDE algorithm. This is apparent in the data in Table 5.2. The table summarizes the results of 100 Monte Carlo simulations. Less than fifty percent of the time varying errors were successfully detected regardless of the variance of the stochastic term. The algorithm did not show significant sensitivity to changes in the time constant.

Table 5.2: Results of FDE algorithm for 100 Monte Carlo simulations of a GPS pseudorange measurement corrupted with random walk error

τ(s)	$\sigma_\epsilon^2(m^2)$	L1 Mean Correct Detection (%)	L1/L2 Mean Correct Detection (%)
30	0.25	0	0
70	0.25	0	0
110	0.25	0	0
30	4.0	6.4	10.4
70	4.0	8.3	10.2
110	4.0	9.5	10.5
30	25.0	41.7	44.1
70	25.0	45.9	46.1
110	25.0	44.1	45.8

A.4 Conclusions

The DRTK/INS federated Kalman filter described in Chapter 3 is expanded to include fault detection and exclusion capabilities. The FDE algorithm is incorporated in the GPS/INS filters that feed the DRTK master filter. To test the algorithm, simulated errors were added to real GPS pseudorange measurements and the data was processed with the DRTK/INS FDE algorithm. Constant errors and time varying errors were simulated in separate tests and performance measures of the algorithm were presented. The FDE algorithm detected all constant bias errors with magnitudes greater than 18 meters. Detection of time varying errors was also heavily dependent on the magnitude of the error. Slowly drifting, low magnitude errors were not detected by the algorithm.